

UNIVERSITÄT HAMBURG

DISSERTATION

---

# Semiconductor Nanorods in the Vicinity of Ordered Gold Nanorods

---

*Author:*

Wiebke Friedrich

*Supervisor:*

Prof. Dr. Horst Weller

*A dissertation submitted in fulfilment of the requirements  
for the degree of Doctor of Science*

*in the*

Department of Chemistry  
Faculty of Mathematics, Informatics and Natural Sciences

Hamburg, March 23, 2015



## **Gutachter**

Prof. Dr. Horst Weller (Universität Hamburg)

Prof. Dr. Alf Mews (Universität Hamburg)

Datum der Disputation: 5. Juni 2015

# *Summary*

In this work, the optical properties of CdSe/CdS semiconductor nanorods in the proximity to ordered gold nanorods were investigated depending on their distance and orientation. Therefore, a substrate with ordered gold nanorods was designed, so that the distance between gold nanorods and semiconductor nanorods could be varied. For the exact interpretation of the data, optical microscopy was correlated with scanning electron microscopy.

Monodisperse gold nanorods with different aspect ratios stabilized by cetyltrimethylammonium bromide were synthesized in aqueous solution. The growth as well as the final optical properties of the rods were studied with UV/Vis-NIR spectroscopical methods and transmission electron microscopy. The influence of the different reagents and parameters was examined. A ligand exchange with octadecanethiol enabled the transfer of the gold nanorods into organic solvents without any loss in shape or monodispersity. Another ligand exchange with the polymer ligand PEGMUA was carefully investigated with regard to a close polymer ligand shell. The parameters of this ligand exchange were analyzed with oxidative etching. Without losing stability against cyanide etching, the amount of PEGMUA could be minimized by a three-step-method. Firstly, the gold nanorods had to be incubated with PEGMUA, secondly extracted with chloroform, and thirdly again stabilized with PEGMUA.

Experiments with different film deposition techniques were performed in order to find an adequate method for the fabrication of horizontally and vertically ordered gold nanorod arrangements. Droplet evaporation was found to be the most promising method. Different parameters such as drying speed, gold nanorod concentration, substrate and droplet volume were investigated. Finally, a setup for the slow and clean drying of the substrate was developed. The optimized droplet evaporation method was transferred to SiN membranes of distinct thicknesses. This substrate met all requirements for the correlation of confocal laser scanning microscopy and scanning electron microscopy. The two-sided preparation of single semiconductor nanorods and ordered gold nanorods assured the well defined distance.

In a first isotropic setup, distance-dependent photoluminescence enhancement and quenching of single semiconductor dot/rods was detected on gold nanoparticle films.

When the experiment was extended to the anisotropic setup with ordered gold nanorods, SiN membrane thicknesses and therefore distances between the two materials of 5, 10, 20 and 50 nm were examined. The optical properties of the single semiconductor nanorods were investigated by means of blinking behavior, photoluminescence intensity and fluorescence lifetime. For a distance of 5 nm between gold nanorods and semiconductor nanocrystals, the photoluminescence intensity was partially quenched. Energy transfer from the semiconductor nanorods to the gold nanorods occurred. At a 20 nm distance to the ordered gold nanorods an enhancement of the photoluminescence intensity was detected. On horizontally ordered gold nanorods, the photoluminescence intensity was 2.2 times higher than without gold and on vertically ordered gold nanorods it was enhanced

by a factor of 8.1. The enhancement is even more pronounced on vertically ordered gold nanorods due to the more intense surface plasmon resonance along the longitudinal direction. Due to the plasmon-exciton interaction, the transition rate between valence and conduction band and the radiative rate are increased. In addition to this, the scattering of the gold nanorods enhances the emission in the far-field. The normalized lifetime of the semiconductor nanocrystals was reduced with decreasing distance between semiconductor nanorods and gold nanorods. The longest lifetime of 8.5 ns was found for semiconductor nanorods with a 50 nm distance to the gold nanorod assemblies. Almost showing no change in lifetime without gold and consequently no plasmon-exciton interaction was observed at this distance. At a 5, 10 and 20 nm distance to gold nanorods the lifetime was reduced to 0.6, 1.4 and 2.3 ns, respectively. The energy transfer rate between gold and semiconductor nanorods was calculated to be 1.55, 0.35, 0.30 and 0.02 ns<sup>-1</sup> for distances of 5, 10, 20 and 50 nm, respectively. This confirms that the energy transfer from semiconductor to gold nanorods is accelerated with decreasing distance.

Overall, the experiments showed a distance and orientation dependence of the photoluminescence intensity from semiconductor nanorods on ordered gold nanorods and a distance dependence of the fluorescence lifetime.

# *Zusammenfassung*

In der vorliegenden Arbeit wurden die optischen Eigenschaften von CdSe/CdS Halbleiternanostäbchen in der Nähe von geordneten Goldnanostäbchen abstands- und orientierungsabhängig untersucht. In diesem Zusammenhang wurde ein Substrat mit geordneten Goldnanostäbchen-Strukturen entwickelt, bei dem der Abstand von Goldnanostäbchen und Halbleiternanostäbchen variiert werden konnte. Für die genaue Interpretation der Daten wurden optische Mikroskopie und Rasterelektronenmikroskopie korreliert.

Monodisperse, mit Cetyltrimethylammoniumbromid stabilisierte Goldnanostäbchen mit unterschiedlichen Aspektverhältnissen wurden im wässrigen Medium synthetisiert. Sowohl das Wachstum als auch die finalen optischen Eigenschaften der Stäbchen wurden mittels UV/Vis-NIR spektroskopischer Methoden sowie Transmissionselektronenmikroskopie untersucht. Der Einfluss der unterschiedlichen Reagenzien und Parameter wurde getestet. Unter Anwendung eines Ligandenaustauschs mit Oktadekanthiol konnten die Nanostäbchen ohne Veränderung von Form und Monodispersität in organische Lösungsmittel überführt werden. Ein anderer Ligandenaustausch mit dem Polymer-Liganden PEGMUA wurde sorgfältig im Hinblick auf eine geschlossene Polymer-Ligandenhülle untersucht. Die Parameter des Ligandenaustauschs wurden mit oxidativem Ätzen analysiert. Die Stabilität gegen das Ätzen mit Zyanid zeigte eindeutig, dass die Menge an eingesetztem PEGMUA mittels einer 3-stufigen Methode minimiert werden kann ohne Stabilität zu verlieren. Zuerst werden die Goldnanostäbchen mit PEGMUA inkubiert. Darauf folgt eine Extraktion mit Chloroform und eine anschließende Stabilisierung mit PEGMUA.

Es wurden Experimente mit verschiedenen Filmdepositionstechniken durchgeführt. So konnte die am besten geeignete Methode, um horizontal und vertikal geordnete Goldnanostäbchen-Anordnungen herzustellen, gefunden werden. Die Tropfen-Evaporations-Methode wurde für am vielversprechendsten befunden. Verschiedene Parameter, wie Trocknungsgeschwindigkeit, Goldnanostäbchenkonzentration, Einfluss des Substrats und Tropfenvolumen wurden studiert. Folglich wurde ein Aufbau für eine langsame und saubere Eintrocknung entworfen. Die optimierte Eintrocknungsmethode wurde auf dünne SiN-Membranen mit unterschiedlicher Dicke übertragen. Diese SiN-Substrate erfüllten alle nötigen Kriterien für die Korrelation von konfokaler Lasermikroskopie und Rasterelektronenmikroskopie. Die Präparation durch Rotationsverdampfung von stark verdünnten Halbleiternanostäbchen und Eintrocknung von Goldnanostäbchen von verschiedenen Seiten der Membran mit definierter Höhe, stellten den festen Abstand sicher.

In einem ersten isotropen Aufbau wurde eine abstandsabhängige Photolumineszenz-Verstärkung und Auslöschung von einzelnen Halbleiternanostäbchen auf Goldnanopartikelfilmen detektiert.

Für den anisotropen Aufbau mit geordneten Goldnanostäbchen wurden 5, 10, 20 und 50 nm dicke Membranen und somit ebensolche Abstände zwischen den beiden Stäbchenmaterialien charakterisiert. Die optischen Eigenschaften von einzelnen Halbleiternanostäbchen wurden im Hinblick auf Blinkverhalten, Photolumineszenz-Intensität sowie Fluoreszenz-Lebenszeiten untersucht. In einem 5 nm Abstand zwischen Gold und Halbleitern wurde

die Photolumineszenz-Intensität teilweise ausgelöscht. Es trat ein Energie-Transfer von den Halbleiternanostäbchen zu den Goldnanostäbchen auf. Bei einem Abstand von 20 nm zu den geordneten Goldnanostäbchen wurde eine Verstärkung der Photolumineszenz gemessen. Auf horizontal geordneten Goldnanostäbchen war die Photolumineszenz-Intensität 2.2 mal höher als ohne Gold und auf vertikal geordneten wurde die Intensität sogar um den Faktor 8.1 verstärkt. Die Verstärkung ist auf vertikal geordneten Goldnanostäbchen-Strukturen noch ausgeprägter aufgrund der höheren Intensität der Oberflächenplasmonenresonanz in longitudinaler Richtung. Aufgrund der Plasmon-Exziton-Wechselwirkung sind die Übergangsgeschwindigkeit zwischen Valenz- und Leitungsband und der Anteil an strahlender Exziton-Rekombination erhöht. Außerdem verstärkt die Streuung der Goldnanostäbchen die Emission im Fernfeld. Bei einem Abstand von 50 nm wurde kein Einfluss der Goldnanostäbchen auf die Photolumineszenz-Intensität beobachtet. Die normalisierte Lebenszeit der Halbleiternanostäbchen nahm mit geringerem Abstand zwischen Gold- und Halbleiternanostäbchen ab. Die längste Lebenszeit von 8,5 ns wurde für Halbleiternanostäbchen in einem 50 nm Abstand zu den Goldstäbchen detektiert. Hier wurde fast keine Abweichung zur Lebenszeit ohne Gold und dementsprechend keine Plasmon-Exziton-Wechselwirkung gemessen. Bei 5, 10 und 20 nm Abstand zu den Goldnanostäbchen wurde die Lebenszeit jeweils auf 0,6, 1,4 bzw. 2,3 ns reduziert. Die Geschwindigkeitsrate für den Energietransfer zwischen Gold- und Halbleiternanostäbchen wurde berechnet. Als Werte ergaben sich 1,55, 1,35, 1,30 und  $0,02 \text{ ns}^{-1}$  für Abstände von jeweils 5, 10, 20 und 50 nm. Dies bestätigt den beschleunigten Energie-Transfer von Halbleiter- zu Goldnanostäbchen bei verringertem Abstand.

Ingesamt haben die Experimente eine abstands- und orientierungsabhängige Photolumineszenz-Intensität und eine abstandsabhängige Lebenszeit von Halbleiternanostäbchen auf geordneten Goldnanostäbchen gezeigt.





# Contents

<b>Summary</b>	<b>ii</b>
<b>Zusammenfassung</b>	<b>iv</b>
<b>Contents</b>	<b>vi</b>
<b>List of Figures</b>	<b>xi</b>
<b>Abbreviations</b>	<b>xv</b>
<b>1 Introduction</b>	<b>1</b>
1.1 Introduction . . . . .	1
1.1.1 Approach and Project Goal . . . . .	2
<b>2 Theoretical Background and Literature Survey</b>	<b>3</b>
2.1 Semiconductor Nanorods . . . . .	3
2.1.1 Semiconductor Bulk Material - Electronic Properties . . . . .	3
2.1.2 Electronic Properties of Semiconductor Nanocrystals . . . . .	5
2.1.2.1 Anisotropic Effects of the Hexagonal Lattice . . . . .	7
2.1.3 Optical Properties of Semiconductor Nanocrystals . . . . .	8
2.1.4 CdSe/CdS Semiconductor Nanorods . . . . .	9
2.1.5 Optical Properties of Individual Semiconductor Nanocrystals . . . .	10
2.2 Gold Nanorods . . . . .	13
2.2.1 Optical Properties of Gold Nanorods . . . . .	15
2.2.2 Test for Successful Ligand Exchange with Polymer Ligands - Cyanide Etching . . . . .	19
2.3 Interaction of Metal and Semiconductor Nanomaterials . . . . .	21
2.3.1 Theoretical Models . . . . .	23
2.3.1.1 Förster Resonance Energy Transfer . . . . .	23
2.3.1.2 CPS Model . . . . .	24
2.3.1.3 Gersten Nitzan Model . . . . .	24
2.3.1.4 Ruppin Model . . . . .	25
2.3.1.5 Radiating Plasmon Model . . . . .	25
2.3.2 State of the Art - what has been done? . . . . .	25
2.4 Ordered Assemblies of GNR . . . . .	28
2.4.1 Coffee Stain Effect . . . . .	28
2.4.1.1 The Case of Ordered GNR . . . . .	29

<b>3</b>	<b>Results and Discussion</b>	<b>33</b>
3.1	CdSe/CdS Dot/Rods . . . . .	33
3.1.1	Size Distribution . . . . .	33
3.1.2	Dimerization . . . . .	35
3.1.3	Optical Properties and Quantum Yield . . . . .	35
3.2	Gold Nanorods . . . . .	37
3.2.1	Synthesis - Characterization . . . . .	37
3.2.1.1	Synthesis according to Nikoobakht et al. . . . .	37
	Size Distribution . . . . .	37
	Optical Properties . . . . .	38
3.2.1.2	Synthesis according to the Murray Group . . . . .	39
	Size Distribution . . . . .	39
	Optical Properties . . . . .	41
3.2.1.3	Growth Monitoring . . . . .	42
3.2.1.4	Influence of the different Parameters . . . . .	42
3.2.2	Ligand Exchange . . . . .	44
3.2.2.1	Octadecanethiol . . . . .	44
3.2.2.2	PEGMUA - Cyanide Etching . . . . .	46
	Etching of Extracted Samples - Monitoring . . . . .	46
	Etching - How much PEGMUA is needed? . . . . .	50
3.3	Ordered GNR Assemblies . . . . .	54
3.3.1	Establishing a Fabrication Method . . . . .	54
3.3.1.1	Film Deposition Techniques . . . . .	54
	Spin Coating . . . . .	54
	Dip Coating . . . . .	57
	Langmuir-Blodgett . . . . .	59
3.3.1.2	High Voltage Cell . . . . .	59
3.3.1.3	Influence of the Substrate . . . . .	61
3.3.2	Properties and Trends . . . . .	62
3.3.2.1	Drying Speed . . . . .	65
3.3.2.2	Droplet Volume . . . . .	67
3.3.2.3	GNR Concentration and the Role of CTAB . . . . .	69
3.3.2.4	Horizontal vs. Vertical Assemblies and Resulting Cracks . . . . .	71
3.3.2.5	Upside-Down-Drying . . . . .	72
3.3.2.6	GNR AR and Monodispersity . . . . .	73
3.3.2.7	Mechanical Cleavage . . . . .	75
3.3.2.8	Influence of Dimercaptosuccinic Acid and NaCl as Additives . . . . .	77
3.4	Fluorescence Intensity Enhancement and Quenching of single SNR on GNP Films . . . . .	79
3.5	Sample Setup for Confocal Laser Scanning Microscopy Measurements on GNR substrates . . . . .	82
3.6	Fluorescence Properties of Single SNR on Ordered GNR . . . . .	84
3.6.1	Photoluminescence Intensity . . . . .	84
3.6.2	Time Traces and Power Law . . . . .	91
3.6.3	Fluorescence Lifetime . . . . .	94

<b>4</b>	<b>Conclusion</b>	<b>101</b>
4.1	Semiconductor Dot/Rods . . . . .	101
4.2	Gold Nanorods . . . . .	101
4.3	Ordered GNR Assemblies . . . . .	102
4.4	Single SNR in the Vicinity of Ordered Gold Nano-structures . . . . .	103
<b>5</b>	<b>Experimental Methods</b>	<b>107</b>
5.1	Chemical Methods . . . . .	107
5.1.1	Chemicals . . . . .	107
5.1.2	Synthesis of Semiconductor Dot/Rods . . . . .	108
5.1.3	Syntheses of Gold Nanorods . . . . .	108
5.1.3.1	Synthesis of GNR stabilized with CTAB . . . . .	108
5.1.3.2	Synthesis of GNR using CTAB and NaOL as surfactant . . . . .	109
	Variation of the Parameters . . . . .	110
5.1.4	Ligand Exchange . . . . .	110
5.1.4.1	Ligand Exchange with Octadecanethiol . . . . .	110
5.1.4.2	Ligand Exchange with PEGMUA . . . . .	111
	Ligand Exchange with Incubation . . . . .	111
	Ligand Exchange with Extraction . . . . .	111
5.1.5	Etching Experiments . . . . .	111
	Monitoring . . . . .	112
	PEGMUA Concentration . . . . .	112
	TEM monitoring . . . . .	114
5.2	Sample Preparation - Physical Methods and Surface Techniques . . . . .	114
5.2.1	Fabrication of GNP Films - Layer-by-Layer Spin Coating . . . . .	114
5.2.2	Fabrication of horizontally and vertically aligned GNR . . . . .	115
5.2.2.1	Substrate . . . . .	115
5.2.2.2	Film Deposition Techniques . . . . .	115
	Spin Coating . . . . .	115
	Dip Coating . . . . .	116
	Langmuir-Blodgett . . . . .	116
	Droplet Evaporation . . . . .	116
5.2.2.3	HV Cell . . . . .	116
5.2.2.4	GNR Solution . . . . .	116
	Aqueous solvent . . . . .	116
	DMSA . . . . .	117
	NaCl . . . . .	117
	Organic Solvent . . . . .	117
5.2.3	Sample Preparation for CLSM Measurements . . . . .	117
5.2.3.1	GNP substrate . . . . .	117
5.2.3.2	GNR substrate . . . . .	118
5.3	Characterization Techniques . . . . .	118
5.3.1	Absorption Spectroscopy . . . . .	118
5.3.2	Emission Spectroscopy . . . . .	119
5.3.3	Transmission Electron Microscopy . . . . .	119
5.3.4	Atomic Force Microscopy . . . . .	121
5.3.5	Scanning Electron Microscopy . . . . .	121

---

5.3.5.1	Setup and Working Principle . . . . .	121
5.3.5.2	Measurement Procedure . . . . .	122
5.3.6	CLSM and TCSPC . . . . .	122
5.3.6.1	Setup and Working Principle . . . . .	122
5.3.6.2	Measurement . . . . .	125
	IRF . . . . .	125
	Measurement Procedure . . . . .	125
	Data Processing . . . . .	125
<b>A</b>	<b>Additional Data</b>	<b>127</b>
A.1	Parameter Variation in the GNR Synthesis . . . . .	127
A.2	GNP Film . . . . .	128
<b>B</b>	<b>Chemicals</b>	<b>129</b>
B.1	All H, EUH and P Statements . . . . .	129
B.2	Chemicals and Statements . . . . .	142
B.3	CMR . . . . .	144
	<b>Bibliography</b>	<b>145</b>
	<b>Declaration of Authorship</b>	<b>158</b>
	<b>Acknowledgements</b>	<b>159</b>

# List of Figures

2.1	Sketch of the dispersion relations. . . . .	7
2.2	Schematic representation of the energy levels in a hexagonal lattice. . . .	8
2.3	Absorption spectrum of CdSe nanocrystals. . . . .	8
2.4	Illustration of the wavefunction localization and band gaps in CdSe/CdS dot/rods. . . . .	9
2.5	Sketches of the different blinking mechanisms. . . . .	10
2.6	Illustration of the three different growth mechanisms of the GNR. . . . .	14
2.7	The original and corrected model for the crystal structure of monocrys- talline GNR. . . . .	15
2.8	TSPR and LSPR are illustrated in an exemplary GNR spectrum. . . . .	18
2.9	Sketch of the competing mechanisms during etching. . . . .	21
2.10	Sketch of how the coffee ring effect evolves. . . . .	29
2.11	Graphs of the calculated potentials, that determine the interaction En- ergy, depending on the gap distance . . . . .	31
3.1	TEM images of the used SNR samples. . . . .	34
3.2	TEM images of SNR-1. . . . .	35
3.3	Optical properties of SNR-1, SNR-2, and SNR-3. . . . .	36
3.4	TEM images of GNR. . . . .	37
3.5	Absorption spectra of synthesis type one and two. . . . .	38
3.6	TEM images from the synthesis variations. . . . .	39
3.7	Absorption spectra of the different synthesis procedures. . . . .	41
3.8	Absorption spectra taken during the GNR growth. . . . .	42
3.9	Absorption spectra from the parameter variations. . . . .	43
3.10	TEM image of the standard synthesis after the transfer to chloroform. . .	44
3.11	Absorption spectra of the standard synthesis before and after the transfer to chloroform and toluene, respectively. . . . .	44
3.12	Monitoring of the extracted samples in 25 mM KCN, interval 5 min. . . .	46
3.13	TEM monitoring of the cyanide etching. . . . .	49
3.14	Monitoring of the purified extracted samples in 25 mM KCN, interval 10 min. . . . .	50
3.15	Absorbance at 450 nm for different PEGMUA concentrations incubated for 16 h. . . . .	51
3.16	Absorbance at 450 nm for different PEGMUA concentrations, 10 $\mu$ M and 25 $\mu$ M PEGMUA addition before extraction. . . . .	52
3.17	Absorbance at 450 nm for different PEGMUA concentrations, 10 $\mu$ M PEGMUA concentration before extraction with different incubation times. .	53

3.18	Absorbance at 450 nm for all experiments after at least 14 d 25 mM KCN exposition/reaction. . . . .	53
3.19	SEM image of octadecanethiol stabilized GNR deposited via spin coating. . . . .	55
3.20	SEM image of the patterned substrate. . . . .	55
3.21	SEM images of GNR in aqueous solution with dioxane addition spin coated on a patterned substrate. . . . .	56
3.22	SEM images of GNR in aqueous solution dip coated on a patterned substrate. . . . .	58
3.23	SEM image of a sample prepared with Langmuir-Blodgett deposition. . . . .	59
3.24	SEM images of GNR with (a) and without (b) applied voltage of 2.0 kV. . . . .	60
3.25	SEM images of GNR drop casted on different substrates. . . . .	61
3.26	SEM images of vertically (a, b) and horizontally (c, d) aligned GNR. . . . .	63
3.27	SEM image of the height of the coffee stain. . . . .	64
3.28	SEM images of GNR assemblies prepared by droplet evaporation with different drying speeds. . . . .	66
3.29	SEM images of GNR assemblies prepared with a different droplet volume. . . . .	68
3.30	SEM images of GNR assemblies prepared with different CTAB and GNR concentrations. . . . .	70
3.31	SEM images of vertical and horizontal GNR assemblies. . . . .	72
3.32	SEM images of a sample dried upside-down. . . . .	73
3.33	SEM images of GNR arrangements of a sample with a bimodal size distribution. . . . .	75
3.34	SEM images of GNR assemblies transferred by mechanical cleavage. . . . .	76
3.35	SEM images of GNR assemblies fabricated under the addition of NaCl. . . . .	77
3.36	SEM images of GNR assemblies dried with added DMSA. . . . .	78
3.37	FI image and the corresponding TM image of a GNP sample with a distance of 11.3 nm. . . . .	80
3.38	Graph of the distance dependent normalized FI. . . . .	80
3.39	Emission spectrum of a single SNR and absorption spectrum of the GNP film. . . . .	82
3.40	Photography and SEM image of a prepared SiN substrates. . . . .	83
3.41	TM and PL Images of the same sample frame of a 50 nm membrane. . . . .	84
3.42	SEM overview image of a 50 nm membrane, corresponding to the TM and PL images shown before. The inset depicts a single SNR on GNR. . . . .	85
3.43	TM and PL image of the same sample frame of a 5 nm membrane and the extracted LP. . . . .	86
3.44	The normalized PL intensity of SNR on GNR plotted vs. the distance. . . . .	87
3.45	The corresponding line profiles with and without GNR beneath, on a 10 nm membrane. . . . .	88
3.46	The corresponding line profiles with and without GNR beneath, on a 50 nm membrane. . . . .	89
3.47	The plots of the corrected normalized PL intensity. . . . .	89
3.48	Time traces of SNR on 5 nm (a), 10 nm (b), 20 nm (c) and 50 nm (d). (e-h) show the corresponding intensity histograms. . . . .	91
3.49	Probability density of on- (a-d) and off-times (e-h) of the different membrane thicknesses. . . . .	93
3.50	Representative time trace on GNR with low intensity. . . . .	93
3.51	Graph of the normalized decay curves. . . . .	94

---

3.52	Graphs of the decays on the different membrane thicknesses, relative to the decay on SiN, respectively. . . . .	95
3.53	Graphs of lifetime vs. distance. . . . .	96
3.54	Graph of the normalized lifetime. . . . .	97
3.55	Graph of the energy transfer rate depending on the distance between GNR and SNR. . . . .	98
3.56	GNR-SNR distance: 50 nm. . . . .	99
3.57	GNR-SNR distance: 5 nm. . . . .	99
3.58	GNR-SNR distance: 20 nm. . . . .	100
5.1	Pictures of the interior of the HV cell. . . . .	117
5.2	Pictures of droplet-drying setup. . . . .	118
5.3	Corresponding SEM and TM images from the window and the scanned frame, respectively. . . . .	123
5.4	A sketch of the FV 1000 setup. . . . .	124
5.5	Schematic representation of the TCSPC connections. . . . .	124
A.1	TEM images of GNR synthesized with varied parameters. . . . .	127
A.2	SEM images of a GNP film on a glass slide. . . . .	128





# Abbreviations

<b>A450</b>	<b>Absorbance</b> at <b>450nm</b>
<b>AA</b>	<b>Ascorbic Acid</b>
<b>AFM</b>	<b>A</b> tomic <b>F</b> orce <b>M</b> icroscopy
<b>APD</b>	<b>A</b> valanche <b>P</b> oto <b>D</b> iode
<b>AR</b>	<b>A</b> spect <b>R</b> atio
<b>CFD</b>	<b>C</b> onstant <b>F</b> raction <b>D</b> iscriminator
<b>CLSM</b>	<b>C</b> onfocal <b>L</b> aser <b>S</b> canning <b>M</b> icroscope
<b>CTAB</b>	<b>C</b> etyl <b>T</b> rimethyl <b>A</b> mmonium <b>B</b> romide
<b>cw</b>	<b>c</b> ontinuous <b>w</b> ave
<b>DMSA</b>	<b>D</b> i <b>M</b> ercapto <b>S</b> uccinic <b>A</b> cid
<b>DDA</b>	<b>D</b> iscrete <b>D</b> ipole <b>A</b> pproximation
<b>DLVO</b>	<b>D</b> erjaguin <b>L</b> andau <b>V</b> erwey <b>O</b> verbeck
<b>DMSA</b>	<b>D</b> i <b>M</b> ercapto <b>S</b> uccinic <b>A</b> cid
<b>EDX</b>	<b>E</b> nergy <b>D</b> ispersive <b>X</b> -ray
<b>FE</b>	<b>F</b> luorescence <b>E</b> nhancement
<b>FI</b>	<b>F</b> luorescence <b>I</b> ntensity
<b>FLIM</b>	<b>F</b> luorescence <b>L</b> ifetime <b>I</b> maging <b>M</b> icroscopy
<b>FRET</b>	<b>F</b> örster <b>R</b> esonance <b>E</b> nergy <b>T</b> ransfer
<b>FWHM</b>	<b>F</b> ull <b>W</b> idth at <b>H</b> alf <b>M</b> aximum
<b>GC</b>	<b>G</b> lassy <b>C</b> arbon
<b>GNP</b>	<b>G</b> old <b>N</b> ano <b>P</b> articles
<b>GNR</b>	<b>G</b> old <b>N</b> ano <b>R</b> ods
<b>hh</b>	<b>h</b> eavy <b>h</b> ole
<b>HOMO</b>	<b>H</b> ighest <b>O</b> ccupied <b>M</b> olecular <b>O</b> rbital
<b>HPA</b>	<b>H</b> exyl <b>P</b> hosponic <b>A</b> cid

---

<b>lh</b>	light hole
<b>LP</b>	Line Profile
<b>LT</b>	LifeTime
<b>LSPR</b>	Longitudinal Surface Plasmon Resonance
<b>LUMO</b>	Lowest Unoccupied Molecular Orbital
<b>NaOL</b>	Na OLeate
<b>NIR</b>	Near InfraRed
<b>ODPA</b>	OctaDecylPhosphonic Acid
<b>PEGMUA</b>	$\alpha$ -methoxypoly-(ethylene glycol)- $\omega$ -(11-mercaptoundecanoate)
<b>PL</b>	PhotoLuminescence
<b>PS</b>	PolyStyrene
<b>QD</b>	Quantum Dot
<b>QY</b>	Quantum Yield
<b>rpm</b>	revolutions per minute
<b>SANS</b>	Small Angle Neutron Scattering
<b>SAXS</b>	Small Angle Xray Scattering
<b>SE</b>	Secondary Electrons
<b>SEM</b>	Scanning Electron Microscopy
<b>SNR</b>	Semiconductor NanoRods
<b>so</b>	split off
<b>STEM</b>	Scanning Transmission Electron Microscopy
<b>STS</b>	Scanning Tunneling Spectroscopy
<b>TCSPC</b>	Time Correlated Single Photon Counting
<b>TDC</b>	Time to Digital Converter
<b>TEM</b>	Transmission Electron Microscopy
<b>TM</b>	TransMission
<b>TMOS</b>	TetraMethylOrthoSilicate
<b>TOP</b>	TriOctylPhosphine
<b>TOPO</b>	TriOctylPhosphine Oxide
<b>TSPR</b>	Transverse Surface Plasmon Resonance
<b>TTTR</b>	Time Tagged Time Resolved
<b>UV/Vis</b>	Ultra Violet/Visible
<b>XRF</b>	X-Ray Fluorescence

# Chapter 1

## Introduction

### 1.1 Introduction

Nanoparticles can be considered as a species between molecules and solid state bulk material. Consequently, the evolution of bulk electronic and optical properties can be observed with increasing number of atoms. Nanocrystals, as a crystalline material below 100 nanometers, exhibit strikingly different properties than bulk material. Although being different from the bulk, the characteristics of the different classes of materials such as metals and semiconductors can be clearly distinguished. In semiconductor nanocrystals the optical properties arise from transitions between the bands, whose energy is shifted into the visible region. In contrast to this, in metallic gold nanoparticles, oscillations of the conduction band electrons determine the optical properties [28, 64].

The size dependence of the optical and electronic properties in materials on the nanoscale are a powerful tool for material science. Thoroughly understood, nanoparticles' properties can be used for innovative materials design [45].

The combination of fluorescing semiconductor nanoparticles and metallic nanocrystals with their collective conduction band oscillation is a challenging possibility to create new devices in catalysis, sensing techniques, surface enhanced Raman scattering (SERS), and light-emitting systems [4, 45].

When it comes to anisotropic particles, the orientation of the semiconductor nanorods (SNR) and gold nanorods (GNR) has an enormous influence on the systems optical

and electronic behavior. The application of these enhanced and sensitive systems of combined metallic and semiconductor anisotropic structures can influence various fields. Especially for medical/biological purposes, the investigation of the conformation and distance dependence of energy transfer and fluorescence enhancement and quenching of SNR in the vicinity of GNR is indispensable. Interesting here is the interaction of SNR with 2-dimensional GNR arrays due to controlled hotspots and NIR scattering of the setup [38, 79, 100].

### 1.1.1 Approach and Project Goal

The optical properties of individual semiconductor nanoparticles and the particle ensemble differ drastically. Besides effects of the polydispersity (morphology, lattice stoichiometry etc.), the fluorescence blinking is an effect that can only be investigated on the single particle level [40]. In this work a setup is developed, in which the GNR are vertically and horizontally ordered, while the SNR are deposited randomly. The setup guarantees a fixed orientation of the gold nanorods to the SNR in an either vertical or horizontal manner. The focus here lies in the photoluminescence intensity of the single SNR depending on their plasmonic environment. The distance between GNR and SNR is varied. Hence, the influence of this plasmonic structure on the SNR fluorescence properties can be analyzed including their dependence on orientation and distance.

## Chapter 2

# Theoretical Background and Literature Survey

### 2.1 Semiconductor Nanorods

In this work, CdSe/CdS dot/rods are used for the optical investigations. The large extinction coefficient in combination with a high quantum yield ease the detection on the single particle level [21, 120]. The dot/rods are synthesized according to a seeded-growth approach, developed by Carbone et al. [15]. The CdSe seeds, which determine the later emission wavelength nucleate hereby based on the supersaturation of the precursor solution. The mechanism of the burst nucleation was explained in detail by LaMer et al. [70]. With a hot-injection method, adding the seeds into a preheated precursor solution, the CdS shell is grown in the presence of a carefully chosen phosphonic acid surfactants mixture. The shell grows preferentially along the c-axis of the hexagonal wurtzite structure of the seeds, so that rod-shaped particles are generated. A negligible small amount of tetrapods grown around the seeds with a cubic lattice is formed [15].

#### 2.1.1 Semiconductor Bulk Material - Electronic Properties

In order to understand the theoretical background of a physical property or a phenomenon, an adequate model has to be chosen or extended. It is important that it

describes everything relevant, but that it is also as simple as possible. The following section gives an overview about the relevant models and concepts.

Many of the basic problems in solid state physics can be solved or understood on the basis of the free electron model. However, in order to understand metallic, insulator or semiconductor like behavior and to distinguish between them, the model has to be extended by a periodic potential.

Consequently, the zone scheme expands to a periodic zone scheme, in which the branches overlap. A band gap is opened in-between. The band gap is proportional to the Fourier component of the potential. From another model, it can be understood, that as a consequence of the large amount of unit cells in a crystal, the electrons are arranged in energy bands. Between those bands, there are energies with no existing orbital; the so called band gaps.

In an impurity free semiconductor crystal, the valence band (occupied states) is separated from the conduction band (unoccupied states). If an electron is now excited to the conduction band, a hole is created and replaces the electron in the valence band. This hole can be characterized as a quasiparticle that fills the vacant orbitals. It shows a  $+e$  behavior under an electric or magnetic current. This electron-hole-pair is called exciton.

The distance between electron and hole is defined as Bohr radius and is on the nanometer scale for bulk material. Different types of electron-hole-pairs can be distinguished, depending on the material. The Mott Wannier excitons are defined by the Coulomb interaction between the charged electron-hole-pair, which is screened by the crystal's dielectric constant. In contrast to this, Frenkel excitons in ionic or polar crystals are localized due to the electrons being tightly bound to the lattice [5, 27].

Besides the periodic potential model and the corresponding definitions, the Schrödinger equation is a prerequisite for the physical description of the semiconductor's electronic structure:

$$H\Psi = \left[ \frac{-\hbar^2}{2m} \nabla^2 + V(r) \right] \Psi = E\Psi \quad (2.1)$$

where  $H$  is the Hamiltonian,  $\Psi$  the wave function,  $\hbar$  the reduced Plank constant,  $m$  the mass a free electron, and  $V(r)$  the potential. According to Bloch's theorem, the eigenstates of the one-electron Hamiltonian can be described by a plane wave function multiplied with the lattice periodicity  $u$  to solve the Schrödinger equation:

$$\Psi_{nk}(r) = e^{ikr} u_{nk}(r) \quad (2.2)$$

The linear combination of Bloch functions now simplifies the problem to solve the Schrödinger equation. Nevertheless, it is a general solution and has to be specified.

Close to the extrema of the bands, the energy dispersion is  $E_c(k) = \frac{\hbar^2}{2m_e^*} k^2 + E_g$  for the conduction band and  $E_v(k) = \frac{-\hbar^2}{2m_h^*} k^2$  for the valence band. Herein gives  $E_g$  the band gap energy and  $m_e^*$  and  $m_h^*$  are the effective masses of the electron and hole, respectively. From this concept is becomes evident, that the curvature of the bands depends on the effective mass. The effective mass is defined as:

$$\frac{1}{m^*} = \frac{1}{\hbar^2} \frac{d^2 E}{dk^2} \quad (2.3)$$

The exact band structure can be calculated with different methods, such as tight-binding method, the independent electron approximation, the cellular method, augmented plane wave method, Green's function method orthogonalized plane wave methods or the use of pseudo potentials, to mention just a few [5, 64].

### 2.1.2 Electronic Properties of Semiconductor Nanocrystals

As already mentioned, in semiconductor nanocrystals the Bohr radius is in the regime of the actual crystal size. Consequently, the motion of the charge carriers is restricted. The confined motion between potential wells can be explained in terms of the electron in a box model. The potential wells are in this case the materials' boundaries.

The eigenenergies of a 0-dimensional semiconductor are then given by:

$$E_{n,l}^{e,h} = \frac{\hbar^2 \beta_{n,l}^2}{2m_{e,h}^* R^2} \quad (2.4)$$

where  $\beta_{n,l}$  stands for the  $n^{th}$  null of the spherical Bessel function of the  $l^{th}$  order. Two cases of confinement can be distinguished:

$$V_{conf}(r) = \begin{cases} 0 & \text{if } r < R \\ \infty & \text{if } r > R \end{cases} \quad (2.5)$$

where  $r$  is the radial coordinate and  $R$  the nanoparticle radius.

For a thorough description of the electronic structure, the band structure has to be analyzed. The conduction band of the in this work investigated II-VI semiconductor nanocrystals emerges from s-type atomic orbitals. Regarding the spin, it is two-fold degenerate. Thus, a parabolic curve is adequate to describe the motion of the electron. The following Hamiltonian for the envelope function can be used for  $r > R$ :

$$H = -\frac{\hbar^2}{2m_e^*} \nabla_e^2 - \frac{\hbar^2}{2m_h^*} \nabla_h^2 + V_e(r_e) + V_h(r_h) - \frac{e^2}{\varepsilon|r_e - r_h|} \quad (2.6)$$

where  $V_e(r_e)$  and  $V_h(r_h)$  are the potentials for electron and hole, respectively, and  $\varepsilon$  the dielectric constant of the semiconductor.

Brus et al. developed based on the effective mass approximation a calculation for the lowest excitation energy for Wannier excitons [13].

$$E = E_g + \frac{\pi^2 \hbar^2}{2R^2} \left[ \frac{1}{m_e^*} + \frac{1}{m_h^*} \right] - \frac{1.8e^2}{\varepsilon R} \quad (2.7)$$

In this calculation, the first part is based on the confinement and the second part considers the Coulomb based interaction of electron and hole.

For the valence band, the case is more complicated. The band originates from p-type orbitals, leading to a six-fold degeneracy of the spin. The electron spin couples to the angular momentum, described by a spin-orbit interaction. This has to be included in the Hamiltonian. An additional summand  $D$  in 2.6 takes the coupling into account.

The molecular orbital theory can be used to explain the exciton generation, too. The charge is transferred from the HOMO (highest occupied molecular orbital) of the anion e.g.  $\text{Se}^{2-}$  to the LUMO in the cation, e. g.  $\text{Cd}^{2+}$ . Since HOMO and LUMO here are linear combinations of different types of atomic orbitals, electron and hole are bound



more weakly than in molecules which makes their separation and independent non-radiative decay more probable [27].

### 2.1.2.1 Anisotropic Effects of the Hexagonal Lattice

The characteristics discussed before include a spherical approximation for the cubic lattice [25]. However, the investigated CdSe/CdS nanorods crystallize in a hexagonal lattice, which makes a more complex approach necessary.

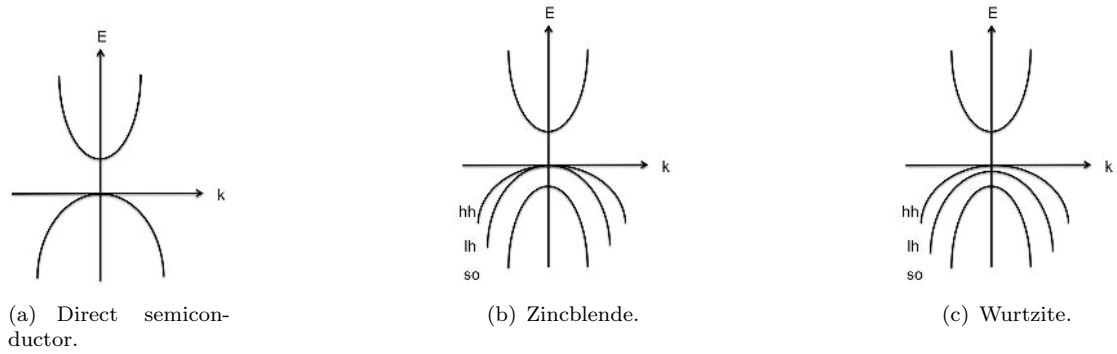


FIGURE 2.1: Sketch of the dispersion relations.

In figure 2.1 (c) the more complex valence band structure is shown for CdSe in comparison to a direct semiconductor (a) in general and the cubic crystal structure (b). The cubic lattice exposes inversion symmetry which is why heavy hole (hh) and light hole (lh) are degenerate. In contrast to this, these two bands are separate in the hexagonal wurtzite structure. This leaves three bands; heavy hole, light hole and split-off band (so) [40]. The splitting occurs due to different effective masses of the hole parallel and perpendicular to the  $c$ -axis of the lattice.

The non-degenerate bands in hexagonal lattices can be understood under consideration of the quantum numbers and couplings, respectively. The eightfold degeneracy of the two parabolic bands for the  $1S_e \rightarrow 1S_h$  transition is lifted when the spin-orbit coupling is no longer neglected. In the valence band,  $J_{\frac{1}{2}}$  (the split-off band) is energetically lower than the state with  $J_{\frac{3}{2}}$  and does not take part in the excitonic ground state  $1S_e \rightarrow 1S_{\frac{1}{2}}$ . In the hexagonal lattice the state  $J_{\frac{3}{2}}$  splits into its projections  $m$ . This leads, if the exchange interaction of electron and hole is taken into account, to five states characterized by the projection of the total angular momentum  $F = M + s_z$ . The splitting of the energy levels is shown in figure 2.2.



FIGURE 2.2: Schematic representation of the energy levels in a hexagonal lattice. The dark states are represented in grey.

For semiconductor nanorods El-Sayed et al. showed, that the relaxation rate decreases with increasing aspect ratio [27].

### 2.1.3 Optical Properties of Semiconductor Nanocrystals

Semiconductor nanocrystals with confined energy levels are often called quantum dots (QD). One of the most prominent properties of QD is the size dependent fluorescence. The nanocrystal absorbs a photon of  $\hbar\omega \geq E_g$ . Subsequently, an electron in state  $i$  is elevated to the conduction band in state  $j$  and leaves a hole in the valence band. Electron and hole recombine under the emittance of a photon of  $E_g$ .

The transition rate for the absorption is given by Fermi's golden rule:

$$\omega_{i \rightarrow j} = \left(\frac{2\pi}{\hbar}\right) |\langle j | eEr | i \rangle|^2 \delta(\varepsilon_j - \varepsilon_i - \hbar\omega) \quad (2.8)$$

The emission rate can be described by:

$$\omega_{j \rightarrow i} = \left(\frac{2\pi}{\hbar}\right) |\langle j | eEr | i \rangle|^2 \delta(\varepsilon_i - \varepsilon_j + \hbar\omega) + \left(\frac{4\alpha\omega_{ji}^3}{c^2}\right) |\langle j | r | i \rangle|^2 \quad (2.9)$$

with  $\omega_{ji} = \frac{(\varepsilon_j - \varepsilon_i)}{\hbar}$  and  $\alpha$  being the fine structure constant. Of course, these optical processes underly the optical transition rules that  $\delta n$  and  $\delta l$  have to be equal to zero.

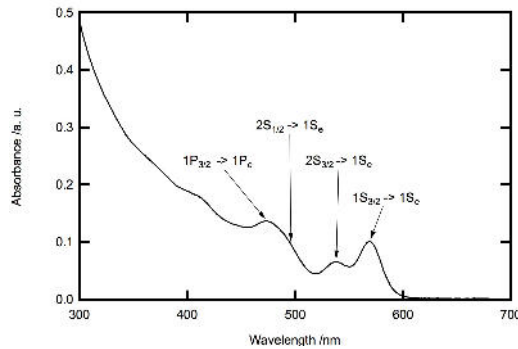


FIGURE 2.3: Absorption spectrum of CdSe nanocrystals. The visible transitions are marked in the spectrum.

For bulk semiconductor  $\omega \rightarrow \infty$ , the absorption is continuous. In contrast to this, for nanocrystals due to the confined states electronic transitions can be distinguished as features in the absorption spectrum [64]. This is exemplarily shown in fig 2.3 for CdSe quantum dots, synthesized within this work.

#### 2.1.4 CdSe/CdS Semiconductor Nanorods

For simply ligand stabilized semiconductor nanoparticles only one half of the atoms at the surface are passivated [90]. This means that non-radiative recombination of electron-hole-pairs due to trap states on the nanocrystal surface becomes more likely. In order to avoid this, two types of core/shell nanoparticles can be grown under the condition that the lattice misfit between core and shell material is small enough.

- **Type I core-shell nanoparticles** in which a wider band gap material is grown around a smaller band gap material => both electron and hole wave function are localized in the core particle, creating a spatial distance between electron-hole-pair and the trap states on the surface
- **Type II core-shell nanoparticles** in which the energy of valence band or conduction band of the shell material is in the band gap of the core material. This leads to a spatial separation of electron and hole wave function.

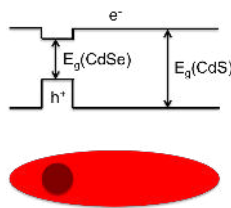


FIGURE 2.4: Illustration of the wavefunction localization and band gaps in CdSe/CdS dot/rods.

The Banin group used scanning tunneling spectroscopy (STS) to determine the band off-set for CdSe/CdS dot/rods [119]. The data obtained by STS is proportional to the density of states. It was possible to prove by performing point measurements on different dot/rod positions that the band gap energy is higher for the CdS shell than for the CdSe core. This confirms that CdSe/CdS is Type I. Both, electron and hole are in the ground state localized in the core. But while the hole wave function is completely localized in

the CdSe core, the electron expands over the CdS shell. This is schematically shown in figure 2.4. A conduction band off-set of  $\delta_c = 0.30 \text{ eV}$  and a valence band off-set of  $\delta_v = 0.44 \text{ eV}$  were determined.

### 2.1.5 Optical Properties of Individual Semiconductor Nanocrystals

Most commonly, semiconductor nanocrystals are optically characterized in the ensemble. Nevertheless, a deeper understanding can only be gained by investigations on the single particle level. This can be realized by the use of a highly diluted solution for the confocal laser scanning microscopy (CLSM) sample. In addition to this, very sensitive detectors and a time correlated single photon counting (TCSPC) device can shed light on the optical properties of individual particles.

While semiconductor nanocrystals exhibit a permanent fluorescence in the ensemble, Brus and coworkers observed on- and off-times of the photoluminescence in the time traces of single CdSe nanoparticles.

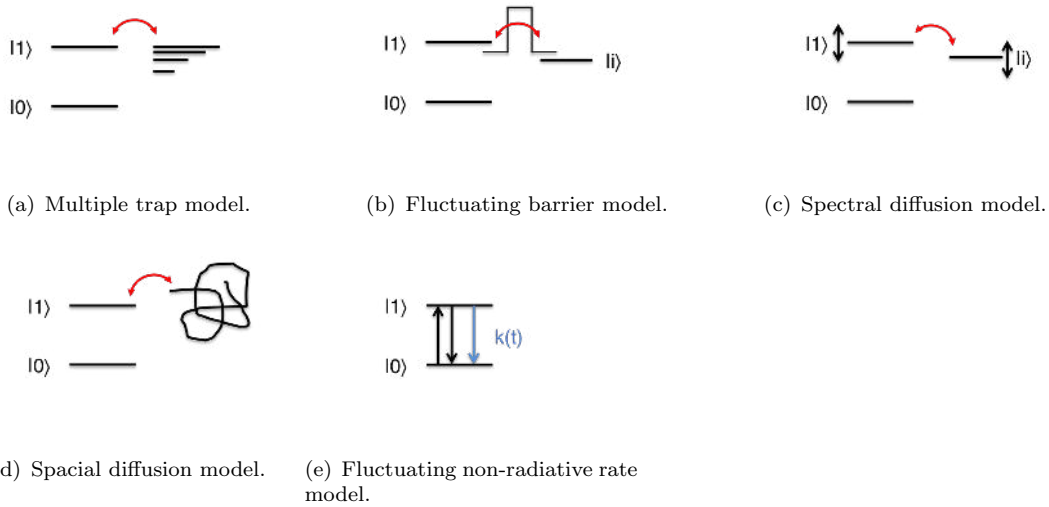


FIGURE 2.5: Sketches of the different blinking mechanisms [32].

They explained this by a two-step mechanism. An electron is ejected and leaves a charged particles. Subsequently, electron-hole recombination occurs by non-radiative Auger relaxation until the photoionization is stopped by neutralization [95]. This Auger-like model was substantiated by Efros et al. [26]. Later on, it was extended by the fact that multiple traps exist on the nanocrystal surface, leading to trapping and de-trapping rates ((a) in fig. 2.5) [122].

For Kuno et al., the intermittency of fluorescence is a result of the change of the local environment during the tunneling between quantum dot and trap state. The altering of the dimensions of the tunneling barrier results in the intermittency ((b) in fig. 2.5) [67].

Shimizu and coworkers found a correlation between spectral diffusion and blinking behavior, where shifts in the emission spectra go together with rare jumps in the fluorescence intensity. They proposed a resonant tunneling mechanism. The tunneling to the acceptor level of the environment is here the main cause for the blinking behavior ((c) in fig. 2.5) [92, 113].

In contrast to this, Margolin et al. introduced a spacial diffusion model ((d) in fig. 2.5) [80]. Under consideration of anomalous diffusion processes, the ejected electron diffuses in 3D space before it returns to the nanocrystal. This model leaves a probability of a constantly dark particle if the electron does not return at all.

Another approach came from Frantsuzov and Marcus, who established a model, in which the trapping rate is accompanied with the spectral diffusion of a second excited state of the semiconductor nanocrystal. Hence, on- and off-states are a result of the non-radiative recombination rate ((e) in fig. 2.5) [33].

However, a theoretical model why the fluorescence intermittency evolves does not help in its mathematical description. In contrast to what is suggested by Bohr's model of quantum jumps, the off-time distribution cannot be represented by an exponential function. Instead, a universal power law has to be introduced with the exponent  $m$  [67]:

$$P(t_{off}) = At_{off}^{-m_{off}} \quad (2.10)$$

The on-time can be illustrated in a similar way, and follows a truncated power law [113]:

$$P(t_{on}) = At_{on}^{-m_{on}} e^{-\frac{t_{on}}{\tau_{on}}} \quad (2.11)$$

Where  $\tau_{on}$ , the saturation factor, depends on various influences such as temperature and intensity.

Schlegel et al. showed, that the decay times are correlated with the fluorescence intensity, which itself fluctuates with the fluctuating environment. This finding was based on time traces with no on- and off-times due to multi exponential decay. They fitted the intensity

$I(t)$  with a stretched exponential function, including the initial intensity  $I_0$  and the decay time  $\tau_{1/e}$ :

$$I(t) = I_0 e^{-\frac{t}{\tau_{1/e}^\beta}} \quad (2.12)$$

where  $\beta$  is the stretching exponent and describes the relaxation rate [110]. In order to fit the probability density with the least-square fit method, Kuno et al. developed a method to weigh the data points statistically. They introduced a factor  $\delta t_{off(on)}^{avg}$  that averages over the next longest and next shortest time [67]:

$$P(t_{off(on)}) = \frac{N(t_{off(on)})}{N_{off(on)}^{tot}} \frac{1}{\delta t_{off(on)}^{avg}} \quad (2.13)$$

with  $N(t_{off(on)})$  being the number of off(on) events and  $N_{off(on)}^{tot}$  being the total number of off(on) events.

Crouch et al. directed the attention to the influence of the choice of binning time  $\delta t$  and the threshold intensity  $I_{thr}$  [19]. While the off-time is insensitive to changes in binning time and  $I_{thr}$ , the on-time has an intrinsic time-scale due to  $\tau_{on}$  and reacts sensitively to changes in the number of bins. In order to avoid a dependence of the results on the threshold intensity, it should be chosen significantly above the background level.

Recent studies on CdSe/CdS dot/rods with a thick shell (diameter of the dots: 2.5 nm, width of the CdS shell: 6 nm) by Javeaux et al. revealed, that the emission can be blinking-free at cryogenic temperatures, as the Auger recombination rate is thermally activated around 200 K. In vacuum, they observed a QY of 100 % due to the radiative recombination of charged excitons [59]. In agreement with these findings, Biadala et al. found 2014 a strong dependence of the radiative recombination rate and the bright-dark energy splitting on the inverse CdS rod width, independent from the core size. The splitting scales quadratically with the inverse of the width. For the thick shell dot/rods, the Auger processes are suppressed as a consequence of the one-dimensional electron delocalization. The bright state was identified as the neutral exciton and the gray state as the negative trion [9, 106].

Besides multiple studies on the intrinsic blinking and recombination dynamics of core-shell nanoparticles, some research groups focused on the characteristics in the vicinity of a plasmonic environment. Ma et al. explained fluorescence enhancement of CdSe

multi-shell particles on a gold nanoparticle film with off-resonant excitation field enhancement, where the metal nanoparticles act as optical antennas. The secondary field of the nanocrystals is scattered which leads to radiationless energy transfer to the metal particles, while the near field is turned into radiation. The blinking is suppressed due to the existence of gray states [77]. Jin et al. explained their observed fluorescence enhancement in the proximity of silver nanoparticles with an enhanced absorption of incident photons and thus contradicted the common approach of an enhanced radiative or non-radiative rate [60]

In contrast to the observed gray states, Bharadwaj et al. studied one and the same quantum dot on a single gold nanoparticle. They detected a preservation of the power law and a binary switching behavior between on- and off-state. For a short QD-GNP distance, the ratio of non-radiative and radiative rate is strongly increased, which explains the decrease in QY. They proposed a mechanism initially introduced by Kuhn in 1970. It is based on a slower on-off than off-on transition [8].

## 2.2 Gold Nanorods

Gold nanorods with their shape dependent optical properties are of great interest. Although the mechanism how spherical gold nanoparticles grow is well understood, there are still several conflicting theories that describe the anisotropic growth of GNR.

In this work the GNR are synthesized with seeded-growth methods. The small gold nanoparticle seeds are formed via the reduction of  $\text{Au}^{3+}$  ions by sodium boron hydride. The particles are stabilized by cetyltrimethylammonium bromide (CTAB). In this rather simple step the spherical particles around 1.5 nm are formed by a burst nucleation, when the reducing agent is added quickly [70, 75, 129]. Although easy to be formed, the seeds have an immense influence on the resulting GNR. An increased size leads to a decreased AR of the GNR. Seeds with a positive surface charge show less aspect ratio dispersity than negatively charged particles regarding the size distribution of the resulting GNR [39].

However, the actual anisotropic growth in the second step is the more complex part. The seeds are added to a growth solution containing gold precursor, stabilizing agent(s), silver nitrate and the reducing agent ascorbic acid (AA). The role of ascorbic acid is

clear; it reduces  $\text{Au}^{3+}$  to  $\text{Au}^0$  so that the rods can grow, but it is not strong enough to trigger nucleation. In the synthesis of the Murray group, the sensitivity of the reaction to the ascorbic acid concentration is minimized by a prereduction of  $\text{Au}^{3+}$  to  $\text{Au}^{1+}$  by sodium oleate (NaOL) [131].

The other reagents contribute to the successful anisotropic growth. Different models state their role as the most important one, respectively. Most likely, the combination of the effects is the key to monodisperse single crystalline GNR. Silver nitrate is a crucial reagent for their formation. Jana came to the conclusion that silver and bromide change CTAB micelles to a rod-like shape, which make them a soft template for the anisotropic growth ((3) in fig. 2.6)[55]. In another approach, surface sensitive techniques are used to prove the underpotential deposition of silver on the longitudinal faces. This makes these covered facets unavailable for gold deposition ((1) in fig. 2.6) [43]. Nevertheless, the third explanation, that a  $[\text{CTABrAg}]^+$  complex acts as a face capping agent and blocks the longitudinal facets is, since it is substantiated by experiments, just as plausible as the other ones ((2) in fig. 2.6) [93].

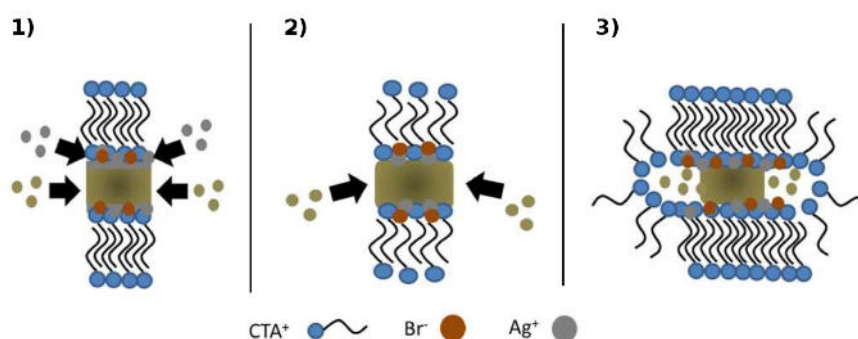


FIGURE 2.6: Illustration of the three different growth mechanisms of the GNR. Reprinted with permission [74].

Besides the silver, Leduc and coworkers showed that the bromide counterion of CTAB is essential for the anisotropic growth, too [115]. It adsorbs selectively and influences the kinetics. This is in agreement with the findings of Smith, Miller and Korgel, who investigated the impurities in different CTAB batches and suppliers. They found that Iodide impurities as small as  $0.57 \mu\text{M}$  hinder the anisotropic rod growth [116, 117]. On the contrary to this model, Ye et al. developed a synthesis based on bromide-free surfactants [130].



These contradicting findings, among other inconsistent theories, affirm, that the anisotropic GNR growth is possible due of mutual effects. The mechanism is highly condition dependent and remains challenging.

Finally, the GNR show a cubic crystal structure, and are with a CTAB bilayer stabilized in water [41]. 11 years after the El-Sayed group had cleared up the crystal structure of GNR, the model was corrected and higher-index facets were added. The two models are depicted in fig. 2.7 [14, 125].

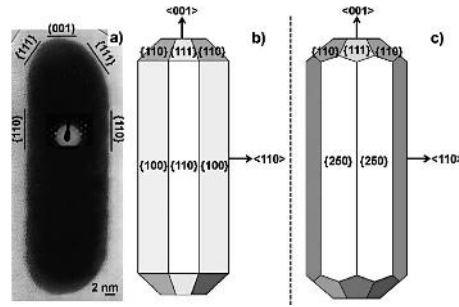


FIGURE 2.7: The original and corrected model for the crystal structure of monocrystalline GNR. Reprinted with permission [14, 125].

### 2.2.1 Optical Properties of Gold Nanorods

Metals exhibit in their interaction with electromagnetic waves fascinating properties, which can be described by solving Maxwell's equations. The oscillator like behavior in the interaction with light of gold and silver nanoparticles in contrast to the relaxator like behavior of bulk material leads to the generation of collective conduction band oscillations. These oscillations are known as surface plasmon polaritons (SPP).

Among the variety of physical models and variables in the interaction with light, this work focuses on the linear optical properties of gold nanoparticles. For macroscopic bodies, those are reflectance and transmission. For nanomaterials, these are extinction and scattering [105]. For the nanoparticle characterization, the main influencing factors are given by the particle shape, the ratio of the irradiating light wavelength and particle size, the complex dielectric function of the material and the dielectric constant of the surrounding medium [73]. For spherical gold nanoparticles in the visible light region, the Rayleigh regime begins above particle sizes of 300 nm.

Besides geometric and electronic resonances, the oscillation of free charge carriers generates, as already mentioned, surface plasmon polaritons. For gold, the surface plasmon

resonance originates from the oscillation of the 6s electrons in the conduction band. The incoming electromagnetic wave polarizes the free electrons and the net charge difference at the particle surface acts as restoring force [105].

Below the Rayleigh regime, Mie theory is an electrodynamic approach to solve Maxwell's equations for small spherical metal nanoparticles. While the Rayleigh scattering uses an electrostatic approach, Mie build his theory based on the plane wave components of the electromagnetic field [69].

By integrating the energy density over the particle volume, the absorption rate can be obtained. Normalized by the intensity of the incoming light, the optical cross sections for extinction, scattering and absorption  $\sigma_{ext}$ ,  $\sigma_{sca}$  and  $\sigma_{abs}$  can be expressed as a particle dependent property.

$$\sigma_{ext} - \sigma_{sca} = \sigma_{abs} \quad (2.14)$$

If these cross sections are further divided by the projection of the particle geometry on the perpendicular plane to the direction of the incoming light  $G$  it results in dimensionless efficiencies  $Q$ :

$$Q_{ext} - Q_{sca} = Q_{abs} \quad (2.15)$$

The extinction cross section for spherical particles can with some assumptions be expressed as [37]:

$$\sigma_{ext} = \frac{24\pi^2 R^3 \varepsilon_m^{3/2}}{\lambda} \frac{\varepsilon''}{(\varepsilon' + 2\varepsilon_m)^2 + \varepsilon''^2} \quad (2.16)$$

where  $\varepsilon_m$  is the medium's dielectric constant and  $\varepsilon'$  and  $\varepsilon''$  are part of the complex dielectric function of the metal. The equation scales with the particle radius  $R^3$  and indicates no absorption, if  $\varepsilon''$  is either non-absorbing (zero) or reflective (infinity).

With regard to Mie theory, the impressive optical properties can be explained under consideration of the dielectric function. For metals, the terms of the complex dielectric functions are given by:

$$\varepsilon'(\lambda) = \varepsilon(0) - \frac{\lambda^2}{\lambda_p^2} \quad (2.17)$$

$$\varepsilon''(\lambda) = \frac{\lambda(\lambda^2 + \lambda_d^2)}{\lambda_p^2 \lambda_d} \quad (2.18)$$

where the plasma wavelength  $\lambda_p$  is material specific and depends on the electron density  $N$ , the effective mass of the electron  $m$ , the damping constant  $\lambda_d$ :

$$\lambda_p = \frac{2\pi c}{\omega_p} = \sqrt{\frac{4\pi^2 c^2 m \varepsilon_0}{N e^2}} \quad (2.19)$$

The confined excitation of conduction band electrons reduces the position of the absorption band of small metal spheres to :

$$\varepsilon_1 = -2\varepsilon_m \quad (2.20)$$

with  $\varepsilon_1$  being the real part of the dielectric function of the metal, and  $\varepsilon_m = n_{med}^2$  giving the direct relation to the refractive index of the medium [103, 105].

Although Mie theory is a powerful tool to calculate optical properties of nanoparticles, when it comes to gold nanorods, the assumptions have to be extended and calculations become more complex. Using Mie-Gans-theory, the plasmon resonance absorption splits into two bands for gold nanorods. This effect is based on the different surface curvatures and thus different restoring forces, which is described in detail in several textbooks and reviews [10, 12, 81, 103, 105]. The transverse surface plasmon resonance (TSPR) band is found at smaller wavelengths and is almost aspect ratio independent. The more intense longitudinal surface plasmon resonance (LSPR) is found at higher wavelengths. This is graphically illustrated in fig. 2.8. For monodisperse gold nanorods the intensity ratio of TSPR and LSPR should be approximately 1:10 [123]. Link and coworkers showed,

comparing theoretical calculations and experiments that the maximum absorption of the longitudinal plasmon resonance depends linearly on the aspect ratio and on the medium dielectric constant [73].

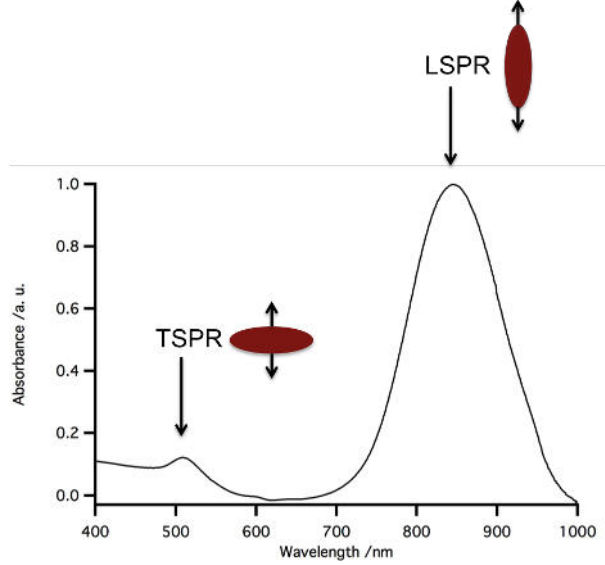


FIGURE 2.8: TSPR and LSPR are illustrated in an exemplary GNR spectrum.

Small gold rods confirm Gans theory, which assumes that the dipole approximation holds, while for high AR GNR other further calculations are more accurate.

The different restoring forces for GNR can also be described with different depolarization fields. Hence, the polarizability  $\alpha$  of an ellipsoid along  $x$ ,  $y$ ,  $z$  axis equivalent to  $a$ ,  $b$  and  $c$  ( $a > b = c$ ) is given by

$$\alpha_{x,y,z} = \frac{4\pi abc(\varepsilon_{Au} - \varepsilon_m)}{3\varepsilon_m + 3L_{x,y,z}(\varepsilon_{Au} - \varepsilon_m)} \quad (2.21)$$

The depolarization factor  $L$  of the axes is

$$L_x = \frac{1 - e^2}{e^2} \left( -a + \frac{1}{2e} \ln \frac{1+e}{1-e} \right) \quad (2.22)$$

$$L_{y,z} = \frac{1 - L_x}{2} \quad (2.23)$$

with the rod ellipticity  $e^2 = 1 - (b/a)^2$  [103].

In practice it has been demonstrated, that gold nanorods are more like cylinders or spherocapped cylinders and optical properties can be exactly calculated with DDA methods [12, 54], instead of the small ellipsoidal model assumed by Gans in 1912 [36].

Furthermore, GNR exhibit area normalized absorption and scattering cross sections that are one order of magnitude higher than the ones determined for spherical particles. For high AR GNR the scattering contrast is significantly enlarged for higher effective radii. If the effective radius is smaller, the absorption becomes more pronounced [54]. This makes them, alongside with the anisotropy of the properties a valuable material for nanomaterial design.

### **2.2.2 Test for Successful Ligand Exchange with Polymer Ligands - Cyanide Etching**

Etching of already synthesized nanoparticles is often used in order to achieve the desired nanoparticles' shape or monodispersity [46]. In addition to the synthetic value, etching can give some indication for the stability of different crystal facets. The already published data about oxidative etching of GNR focusses mainly on the CTAB stabilized rods. The etching with hydrogen peroxide and  $\text{Au}^{3+}$  ions revealed a spatially directed etching at the nanorods' tips. The preferential etching was only observed in the presence of CTAB as ligand. The attack of the higher curved surface sites was explained by a higher flux of the reactant on highly curved surfaces than on flat ones [107, 133]. Interestingly, Jana et al. found a different etching mechanism with cyanide depending on the AR. Between AR of 2 and 5, only the tips were attacked, in agreement with the already mentioned publications. For GNR with an AR of 18, the etching started at many sites and without any change in length. This was explained by a different local crystal structure, where the defect sites reacted advantageously [56].

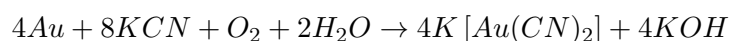
The etching experiments in this work focus on the ligand shell characterization. The stabilizing ligands are a crucial factor for the nanoparticle properties. Gold nanoparticles are used for biological or medical applications, which makes the characteristics of the stabilizing ligand system even more essential. CTAB in general and free molecules in

solution in particular exhibits a high cytotoxicity [3]. Hence, a ligand exchange is a prerequisite for further application.

The surfactant CTAB used during the GNR synthesis forms a highly stable bilayer. Hence, a complete ligand exchange is not straight forward, since CTAB is often not removed completely. For an effective lab routine, a system how to evaluate the ligand exchange is adopted and transferred to the GNR system in this work. This was achieved in collaboration with Dr. Florian Schulz.

The successful ligand exchange with polymer ligands can be tested via the resistance against cyanide etching. The probe has been applied for colloidal gold nanoparticles with different ligand systems [85, 112]. Schulz et al. impressively proved the substitution of the citrate ligands with ligands composed of a PEG (polyethylene glycol) unit linked by different spacers to a thiol group. The PEG unit is linked to the spacer by an ester bond. The polymer ligand provides application of the nanoparticles in biological or medical experiments. The test is based on the fact, that the resistance towards etching is drastically improved by the polymer ligand shell in comparison to the initial system.

The etching itself is based on the reaction of the cyanide ions with gold:



where the main product, the cyanide gold complex, is colorless, so that the reaction can be monitored with time-resolved UV/Vis spectroscopy [112].

Based on the findings of Schulz et al. fig. 5.1.5 illustrates the two competing mechanisms that can occur during the cyanide etching of GNR. Firstly, the rods can be etched layer-by-layer, as the ligand shell is repaired after a first cyanide reaction. The rod is restabilized by free ligand from the solution. This would result in decrease in size but a more or less constant GNR concentration. The second mechanism is that the repairing effect is less pronounced and a rod, once a defect site is created, "vanishes" completely. This would result in a decrease in concentration, but constant GNR dimensions.

As a consequence of the asymmetry of the GNR, the location of the defect site can shed light on the quality of the stabilization of transversal and longitudinal facets. If the

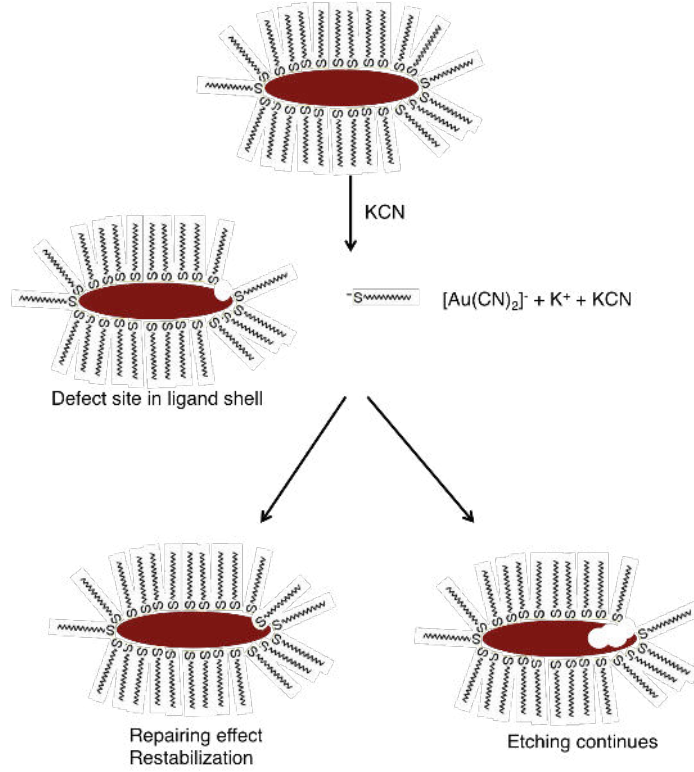


FIGURE 2.9: Sketch of the competing mechanisms during etching.

cyanide attacks first on the end of the GNR, the AR decreases and therefore the LSPR would be shifted to smaller wavelengths. If the etching rate is higher on the longitudinal facets, the AR would increase and thus one would expect a LSPR at higher wavelengths.

## 2.3 Interaction of Metal and Semiconductor Nanomaterials

In this work, the interaction of CdSe/CdS semiconductor dot/rods (SNR) with gold nanorods is studied. This means, the model system consists of a fluorescing dipole in proximity to an electric field originating from the surface plasmon resonances of the GNR. Mainly, two competing and distance dependent processes play a role in this interaction; the radiationless energy transfer from the dot/rods to the metal and the photoluminescence (PL) enhancement. Those two mechanisms are influenced by the absorption, radiative emission and the non-radiative dissipation [53].

The distance dependent energy transfer between donor and acceptor, is often described with Förster resonance energy transfer (FRET). The energy transfer rate  $k_{FRET}$  is given

by:

$$k_{FRET} = \frac{1}{\tau_0} \left( \frac{R_0}{d} \right)^n \quad (2.24)$$

with the lifetime of the donor  $\tau_0$  and, the Förster radius  $R_0$  and the distance  $d$ .  $n$  depends on the absorbing medium. The lifetime is determined by its intrinsic and its non-radiative decay rate.

This model works for semiconductor nanoparticles in the vicinity of an absorbing medium or molecules, as well as quenching metal ions [7, 11, 58]. However, when the interaction with a plasmonic nanostructure is considered, the radiative rate is more complex.

The total exciton recombination rate  $k_{tot}$  including the GNR-SNR interaction can be expressed by:

$$k_{tot} = k_{rad} + k_{non-rad}^0 + k_{non-rad,metal} \quad (2.25)$$

where  $k_{rad}$  is the radiative rate and  $k_{non-rad}^0$  the non-radiative rate of the SNR and  $k_{non-rad,metal}$  is the recombination rate including the interaction with GNR.

The intensities for absorption and emission  $I_{abs}$  and  $I_{emis}$  are given by [42]:

$$I_{abs} = P(\omega_{laser}) I_{abs}^0 \quad (2.26)$$

$$k_{rad} = P(\omega_{emis}) k_{rad}^0 \quad (2.27)$$

$$I_{emis}(\omega_{emis}) = \frac{P(\omega_{emis}) k_{rad}^0 P(\omega_{laser}) I_{abs}^0}{P(\omega_{emis}) k_{rad}^0 + k_{non-rad}^0 + k_{non-rad,metal}(\omega_{emis})} \quad (2.28)$$

with the PL enhancement factor  $P$  depending on the laser frequency  $\omega_{laser}$  or the exciton emission frequency  $\omega_{emis}$ . The non-radiative emission rate in interaction with the metal can be deduced from Fermi's golden rule and the resulting matrix of initial state  $|exc; 0_{pl}\rangle$  and final states  $|0_{exc}; f\rangle$ :

$$k_{non-rad,metal}(\omega_{exc}) = \langle \sum |\langle 0_{exc}; f | V_{int} | exc; 0_{pl} \rangle|^2 \delta(\hbar\omega_{exc} - \hbar\omega_f) \rangle \quad (2.29)$$



In order to obtain a comparable, focus independent intensity, a normalized intensity  $I_{gold}/I_0$  is introduced, where the PL intensity on the gold nanostructure  $I_{gold}$  is normalized by the PL intensity without gold  $I_0$ :

$$\frac{I_{gold}}{I_0} \approx \frac{P(\omega_{emis})P(\omega_{laser})k_{rad}}{k_{non-rad,metal}} \quad (2.30)$$

Three different parameters change, depending on the distance, simultaneously; the absorptive rate, the radiative and the non-radiative rate. Since their influences on the PL intensity cannot be weighed or separated, the interpretation of the data is challenging.

In addition to a proper knowledge of the theoretical models, a setup with a high time-resolution is necessary, as the fluorescence lifetime decreases drastically in the direct vicinity of metal nanoparticles [69].

Those aforementioned most important theoretical models that describe the complex interactions are presented in the following in more detail. All concepts have strengths and weaknesses applied to the present system.

### 2.3.1 Theoretical Models

#### 2.3.1.1 Förster Resonance Energy Transfer

FRET is a donor-acceptor based interaction between two dipoles. Energy is transferred from the fluorescing donor to the acceptor, whereupon the donor's fluorescence is quenched. An adequate position of donor and acceptor levels is a prerequisite. This can be assured by an overlap in the absorption spectrum of the acceptor and emission spectra of the donor species. If two point dipoles are investigated, the transfer probability scales with a factor of  $d^{-6}$  and a Förster radius  $R_0$  can be calculated at which the transfer probability is 0.5.

$$R_0^6 = \frac{9(\ln(10))}{128\pi^5 N_A} \kappa^2 n^{-4} \phi_0 J(\lambda) \quad (2.31)$$

where  $n$  is the index of refraction,  $J$  defines the overlap integral and  $\kappa$  is determined by the orientation of the two dipoles with the angles  $\sigma_D$  and  $\sigma_A$  and the angle towards

each other  $\sigma_{DA}$  [31]:

$$\kappa = \cos \sigma_{DA} - 3 \cos \sigma_A \cos \sigma_D \quad (2.32)$$

$\kappa^2$  is between 0 for orthogonal dipole moments and 4 for a parallel orientation of both dipoles.

In this case, the point dipole interacts with metal nanorods. The FRET concept can be applied at small distances and if not only the SNR but as well the GNR are considered as point dipoles. Although this model describes the quenching of the SNR in close proximity to GNR fairly good, it does not take the influence of the GNR on the radiative rate into account. In addition to this, the assumption that two point dipoles interact, does not hold [69].

### 2.3.1.2 CPS Model

Drexhage performed the pioneering work on the field when he modeled the approach of a fluorophore to a metal film regarding its radiative and non-radiative rates [23]. Chance, Prock and Silbey (CPS) tied in with this, with a fundamental addition. They included the interaction between absorbing medium and dipole closer than 100 nm, solving Maxwells equations. For this they assumed that the metal film was completely smooth. The energy transfer scales with  $d^{-4}$  for films and with  $d^{-3}$  for volumes. The mirror effect of the metal film was incorporated, when they calculated an increased non-radiative rate due to absorption of the surface [17]. The main drawback of these calculations is the assumption that the absorbing medium is of finite thickness and homogeneously flat. GNR or nanoparticles exhibit a surface roughness or additional hot spots for surface enhancement [101, 121].

### 2.3.1.3 Gersten Nitzan Model

The Gersten Nitzan model is an electrostatic model based on solving the Maxwell equations for a fluorescing molecule near a metal nanoparticle system. Gersten and Nitzan take into account that the fluorescing molecule induces a dipole. This dipole moment of the metallic nanoparticle changes its electric field and consequently the total dipole moment, too. Since the metal nanoparticles are not infinitely conductive, Gersten and

Nitzan were able to calculate a non-radiative rate based on the ohmic losses [69]. The model calculates not only the quenching in close proximity, but also an enhanced emission of the fluorophore. Accordingly, the lifetime depends on the orientation of the dipole to the metal nanoparticle. It matches with the CPS model for the lifetime of a perpendicularly oriented dipole. Unfortunately, it gives only reliable information for dipoles and nanoparticles that are in the size regime of the penetration depth of the light (around 10 nm) [68, 76].

#### **2.3.1.4 Ruppin Model**

Ruppin dissected the electromagnetic field into plane waves and used them for his electrodynamic model. Linear combinations of these plane waves lead to radiative and non-radiative rates, respectively. As a local theory, the model is only reasonable for metal-fluorophore distances larger than a few nanometers [108, 109].

#### **2.3.1.5 Radiating Plasmon Model**

Lakowicz developed a model that explains lossy surface waves as trapped plasmons. They decay as heat if quenching is observed. He states, that the interaction of fluorophores with metal nanoparticles or films is determined by the metal's optical properties. If the scattering cross section is dominant, the fluorescence is enhanced by radiation of the trapped plasmons. It is quenched, if the absorption cross section is controlling [68]. The radiation of the plasmons is dictated from the optical selection rules, that means if the wave vectors match, the plasmon radiates.

### **2.3.2 State of the Art - what has been done?**

A lot of research has been done in the field of fluorescence quenching and enhancement when a fluorescing species is brought in the vicinity of metal nanoparticles.

In 2009, Fu and Lakowicz published a study about the near-field (wavelength distance) of single fluorophores with metal nanostructures. They found a quenching due to lossy surface waves at small distances and shorter lifetimes, from which they concluded a higher photo stability of the fluorophore as it spends less time in the excited state

[34]. Their findings agree with Shimizu et al. who found a reduced blinking behavior of QD on rough thin gold films. They stated, that this observation originates from the emission of charged nanoparticles. In contrast to the usual non-radiative decay for charged particles, the combination of radiative rate and absorption rate near the gold nanostructure accelerates the radiative relaxation processes [114].

Related to the work of the Bawendi group, various other researchers investigated QD in the vicinity of gold films. Ito et al. compared single QD on rough and flat gold surfaces. While the PL was quenched on flat films, it was enhanced on rough gold, depending on the laser excitation wavelength. Additionally, they confirmed the suppressed blinking on gold due to accelerated rates. In the proximate year they extended their study and reported a strong dependence on the polarization of the excitation wavelength. In the same year, the group around Kanemitsu published a study of mixed gold nanoparticle and QD monolayers. They found a decreased PL intensity with increasing amount of gold nanoparticles and an increased electromagnetic enhancement factor, determined with Raman scattering. They explained their results by a step-by-step ET from the QD to the directly adjacent gold nanoparticle and the second neighboring gold nanoparticle via a neighboring QD [50, 53, 61, 83].

Kawai et al. investigated the PL of CdSe nanoparticle multilayers at different distances to a thin gold film. At a distance of 60 nm the PL intensity was maximal, while the fluorescence decay decreased constantly with decreasing distance to the gold film [62]. Ueda et al. detected the maximum PL intensity at a distance of 43 nm which was also their largest investigated distance from QD to gold film [121].

These rather long distances contradict the results of Kulakovich et al. who found 11 nm as the distance between QD and a gold particle film for maximal PL enhancement [66]. Another contradictory paper was published by Okamoto et al. who deposited QD without any spacer on a gold film and measured a 23 fold PL enhancement for CdSe nanocrystals. The effect was not observed for CdSe/ZnS particles as their initial quantum efficiency is too high for the coupling based PL enhancement [97].

In addition to the distance to gold nanoparticles and their amount, also the size of the gold colloids seems to have a major influence on the relation between ET and fluorescence enhancement. West et al. discovered an interparticle FRET for QD emitting at different wavelengths. The fluorescence enhancement was high in the vicinity of larger gold

nanoparticles and ET to the metal was dominant for smaller gold particle films. This finding agrees with the RP model, in which fluorescence enhancement is expected for fluorophores close to gold nanostructures with large scattering cross sections (larger GNP) and a quenching when the absorption is more pronounced (small colloids) [68, 126].

Peng et al. focused their investigations on the properties of a QD monolayer at a defined distance to vertically ordered GNR. Besides the decrease in lifetime closer to the GNR monolayer which is affirmed by all research groups, they recorded a quenching of the QD emission for a silica spacer of 5 nm and a 10.4 fold enhancement of PL for a spacer thickness of 20 nm. No change in PL intensity was detected at thicknesses of 50 nm and more [101].

In 2010, Fu et al. were able to link fluorophores to biotin capped GNR with an AR of 6. The emission rate was 40 times higher and the decay rate of fluorophores ligated to the longitudinal faces of the GNR faster compared to the fluorophores in solution. Lakowicz and coworkers justified the results with the radiating plasmon model as the scattering component is dominant above 600 nm [35]. The radiating plasmon model was used as an explanation by the group around Geddes, too. They reported an angular dependence for the fluorescence enhancement of a dye close to metal nanoparticles. The effect was found to be highest (2.5 fold) for larger colloids (200 nm) and an angle of  $270^\circ$  [6].

Similar to Fu et al. 2010, several groups deposited a dye at a defined distance to gold nanoparticles or GNR. They used a silica shell as a spacer and grew another dye-containing silica shell around the gold nanoparticles. Another method is that the dye was incorporated in a silica shell at a certain distance. Peng et al. detected the strongest PL enhancement at a spacer thickness of 21.9 nm and a quenching behavior below 7.6 nm, with a quenching maximum at 2.8 nm. This was accompanied by a distance dependent decrease in lifetime. In contrast to this, Nepal et al. observed fluorescence enhancement only if the dye was positioned around the GNR tips. Ming et al. found, besides a polarization dependence, the highest fluorescence enhancement, when the excitation wavelength is chosen close to the LSPR wavelength [88, 91, 99].

Duan et al. determined the radiative and non-radiative rates of emitters in the proximity of GNR with different AR theoretically. They found fluorescence enhancement for fluorophores close to single GNR with larger AR (6.5), except for the emitters close to

the tip of the GNR. Interestingly, the enhancement effect close to GNR dimers was most pronounced for GNR with an AR of 4.1 [24].

Chakraborty et al. managed to fabricate gold-tipped CdSe/CdS nanorods and studied their fluorescence behavior. As the SNR are Type I core-shell-structures, the exciton is localized in the core. Thus, the Au-tipped SNR showed a shell dependent fluorescence enhancement [16].

The Banin group found, that an AFM tip apex at a distinct distance to single QD and dot/rods contributed to the lightning rod effect and thus enhanced the fluorescence of the particles. Both systems showed more particles with enhanced fluorescence with radially polarized light than with azimuthally. The researchers observed the best conditions if the surface plasmon resonance is slightly blue shifted in comparison to the emission wavelength of the nanoparticle and if the particles exhibit a low quantum yield without enhancement [132].

In conclusion, a plethora of research groups focus on the change in optical properties in gold-fluorophore-systems. All of them detected a monotonically reducing lifetime with decreasing distance to the metal film/nanoparticles. However, the results evaluating the distance dependent PL enhancement/quenching differ almost by a factor of 10. This is a strong indication, that the system is very sensitive to all involved parameter. The excitation wavelength, QD emission wavelength, QD system, metal system and SPR wavelength matter.

## 2.4 Ordered Assemblies of GNR

Self-assembly of GNR is a challenging task if the ordered arrangements should cover several hundreds of micrometers. Stabilization, solvent, substrate, concentration, and other conditions contribute to the successful experiment. In the following, some concepts are presented that dominate the assembly process.

### 2.4.1 Coffee Stain Effect

This superior effect was published by Deegan and Witten in 1997. They analyzed, why the material is found at the periphery of the droplet after the drying process, when a

solution is drop casted on a substrate. This finding is substrate and material independent. The model explains that with a pinned contact line due to surface irregularities a volume flow outwards evolves. The droplet itself is in this electrostatic description the conductor with a fixed potential. The evaporation is much higher at the pinned edge, which leads to the volume flow outwards and subsequent material deposition at the edge. The determining factors for the effect, are evaporation flux and contact angle. A higher material concentration leads to a wider ring [20]. The droplet and the described flow outwards as well as the evaporation rate are schematically illustrated in figure 2.10.

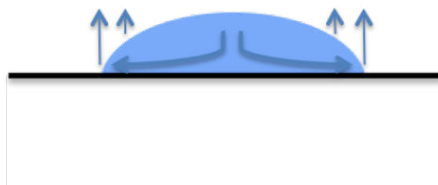


FIGURE 2.10: Sketch of how the coffee ring effect evolves.

The competing effect is the Marangoni flow, especially in organic solvents. Due to the latent heat of evaporation an additional flow to the center of the droplet is generated, depending on the surface tension gradients. In water, those recircular flows are negligibly small, although clean surfaces and interfaces enhance the Marangoni flow. Another parameter influencing this balance is the temperature [51].

Motivated by the behavior of fertilizer droplets on leaves, Hampton et al. investigated the drying of a pendant drop of an aqueous silica nanoparticle solution in comparison to a sessile setup. They observed a thin coffee ring and a central "bump" in contrast to the well known thicker coffee ring. This is explained by gravity and convection induced internal flows. The particles move towards the point of the droplet with the biggest diameter and here the concentration related aggregation starts. Due to gravity, the ordered particles do not arrive at the contact line within the drying process, but are kept in the center, which is as well the lowest point [49].

#### 2.4.1.1 The Case of Ordered GNR

There are several groups, that produce ordered GNR arrays by dropcasting the GNR solution on the substrate. Many of them use a ligand directed mechanism. The Liz-Marzan group uses a gemini surfactant, while Xie et al. achieve standing superlattices

by application of an OH terminated hexa(ethylene glycol) alkanethiol ligand [44, 127]. Iacopino and coworkers transferred the GNR into an organic solvent with a tetraoctyl orthosilicate chlorobenzene system [82]. Mitamura et al. hydrophobized the GNR with a mercaptopropyltrimethoxy silane and octadecyltrimethyl silane with an increased pH value [89]. Another concept developed by the Petukhova group utilizes the bad solubility of S-terminated polystyrene ligands in THF, where the polymer ligand supports the precipitation of ordered GNR arrays from the solution [104].

For CTAB stabilized GNR in aqueous solution, the assembly is directed by the different interactions. The influence of the aqueous solution can be estimated by the Debye length, which defines the screening length after which the electric potential drops. This means a small ionic strength describes a compressed electrical double layer and a small distance between the GNR. For GNR, calculated as charged spherocylinders, an anisotropy factor of  $\frac{L}{D} - 1$  with the length  $L$  and the diameter  $D$  is introduced. This results in a screening length of  $\kappa^{-1} = 6.5$  nm [65]. Also Peng et al. used the screening length, defined as  $\kappa^{-1} = \frac{0.3}{I^{2/3}}$ , with  $I$  as the molar ionic strength [100].

They proposed a mechanism based on the total interaction energy  $E_{total}$

$$E_{total} = E_{ele} + E_{dep} + E_{vdW} \quad (2.33)$$

in which the electrostatic potential  $E_{ele}$ , the attractive depletion force  $E_{dep}$  and the van-der-Waals force  $E_{vdW}$  are added. The assembly is dominantly determined by  $E_{vdW}$  and  $E_{ele}$ . The latter can be calculated using Derjaguin's approximation and includes the electric permittivities of the electrolyte solution. The total interaction energy as a function of the gap distance between the GNR was calculated for GNR with different AR and consequently different LSPR wavelengths with a Debye length of 3 nm. The calculations are shown in fig. 2.11. They found a minimum for the total interaction energy  $E_{total}$  at a gap distance around 7.5 nm between the GNR in the array, independent of the AR. Nevertheless, the potentials are in general lower for smaller AR (smaller LSPR wavelengths).

According to Peng et al., the GNR aggregate during the evaporation of the solvent in the solution in a side-by-side manner instead of the energetically less favorable end-to-end manner. The electrostatic potential prevents here the random attachment, while the



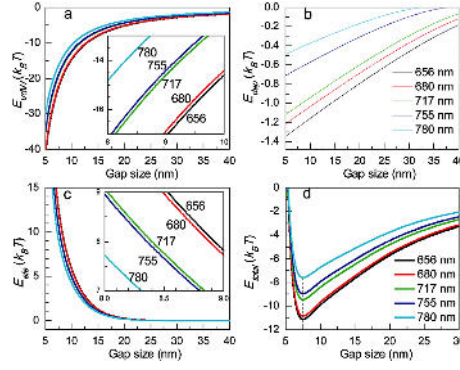


FIGURE 2.11: Graphs of the calculated potentials, that determine the interaction Energy, depending on the gap distance. Reprinted with permission [101].

attractive van-der-Waals force, mainly determined by the Hamaker constant  $A_{eff}$ , and the depletion force direct the assembly [128].

Xie et al. adapted the droplet evaporation technique and developed a two-stage mechanism. Firstly, the evaporation rate is chosen relatively high, so that the pinned contact line favoring the coffee stain effect, evolves. Secondly, the evaporation rate is reduced so that a saturated atmosphere emerges and the GNR assemble in the thermodynamic most stable manner. In agreement with Peng et al. their calculations confirmed that a side-by-side assembly is the energetically most stable configuration. The other stable configuration is the ordered end-to-end-arrangement, which is observed at lower CTAB concentrations or lower electrostatic potential [100, 128].

The concept is described by the electrical double layer (EDL) model, in which the inner Stern layer consists of the  $CTA^+$  stabilized gold surface, followed by Coulomb force attracted  $Br^-$  ions. They build the slipping plane, in which positive and negative charges are separated. This is no longer the case for the end of the Debye length, where the diffuse layer begins.

Besides the dielectric permittivity, the rods length and diameter, the surface charge density, and the CTAB concentration (determined by its critical micelle concentration) influences the electrostatic potential. Interestingly, a second energy minimum is observed, which is explained by nanoparticle assembly interaction.

As well as Peng and coworkers, Xie et al suggest an assembly of side-by-side monolayer islands in solution. When the droplet drying proceeds, due to substrate-GNR island interaction, the GNR monolayer is not homogeneously spread over the whole droplet.

Especially the denser regions at the periphery show some cracks when the solvent has evaporated [128].

## Chapter 3

# Results and Discussion

### 3.1 CdSe/CdS Dot/Rods

Three different dot/rod samples, synthesized according to Carbone et al., were used for the confocal measurements in this work [15]. They are in the following referred to as SNR-1, SNR-2, and SNR-3 . SNR-1 and SNR-2 were provided by Christopher Wolter. For the sake of rigor, only these samples, utilized in the optical measurements, are discussed in the following.

#### 3.1.1 Size Distribution

The TEM images in fig. 3.1 show the three SNR samples, which are used for the central optical measurements, respectively.

In the images it is already obvious, that the SNR have a narrow size distribution and that almost no tetrapods were formed during the syntheses. However, the length of the different samples differs, depending on the seed size, temperature and growth time after the seed addition, before the reaction was stopped (see 5.1.2). The exact dimensions were determined by measuring at least 100 SNR with the program Image J and fitting the resulting histograms. The dimensions are listed in the table below.

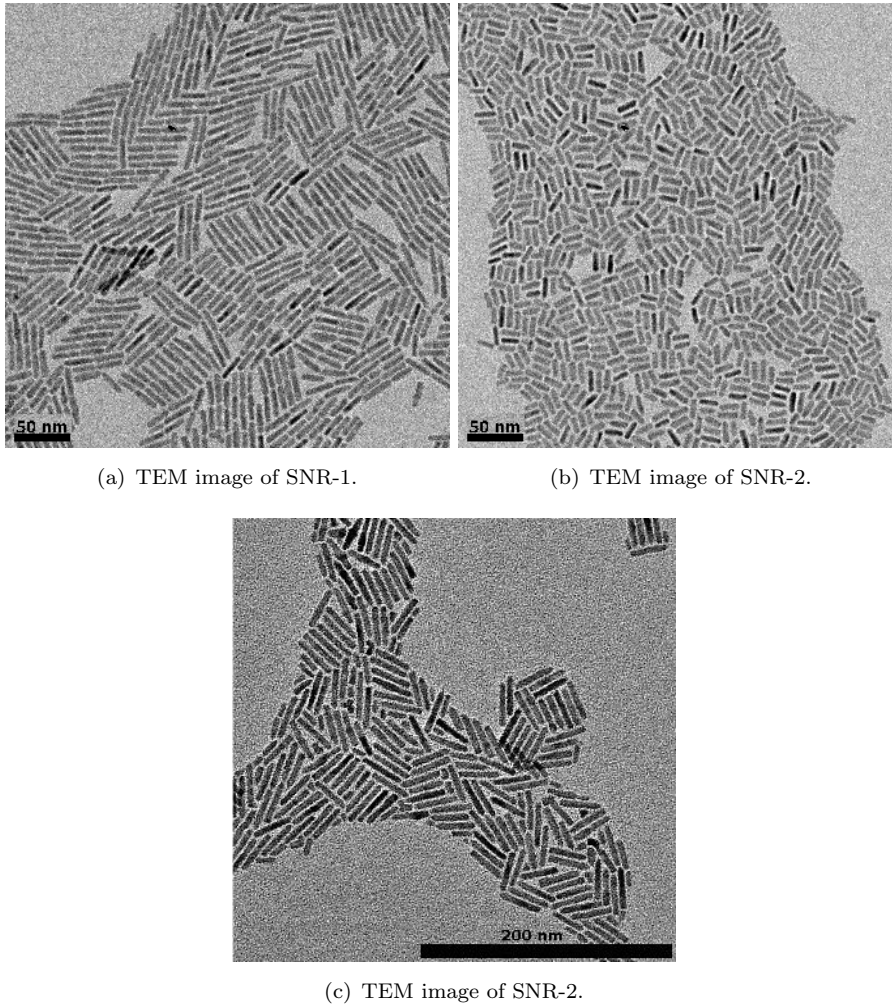


FIGURE 3.1: TEM images of the used SNR samples.

Name	Length /nm	Width /nm	Aspect Ratio /nm
SNR-1	$22.84 \pm 2.31$	$4.82 \pm 0.86$	$4.14 \pm 0.83$
SNR-2	$16.26 \pm 1.14$	$4.50 \pm 0.55$	$3.31 \pm 0.36$
SNR-3	$19.63 \pm 5.50$	$4.27 \pm 0.29$	$5.51 \pm 0.22$

The CdSe seeds used for the growth-step were  $4.64 \pm 0.36$  nm,  $4.47 \pm 1.27$ , and  $4.43 \pm 0.50$  for SNR-1, SNR-2, and SNR-3, respectively. From the comparison of the rod width and seed diameter it becomes obvious that the CdS shell is rather thin. The position of the CdSe seeds inside the SNR, determined with HRTEM is mostly symmetric. This indicates the application of enough ligands to stabilize all crystal facets. If this was not the case, Cd would preferentially accumulate on the (001) facets of the seeds, resulting in an asymmetric growth and seed position [57].

### 3.1.2 Dimerization

Interestingly, the sample SNR-1 showed a dimerization. In the TEM grid preparation, the solvent chloroform was removed immediately. This indicates, that the SNR might have already dimerized in solution. If the TEM image in fig 3.1 (a) is regarded carefully, the accumulation of SNR can be identified as SNR dimers. This becomes more evident in the following images:

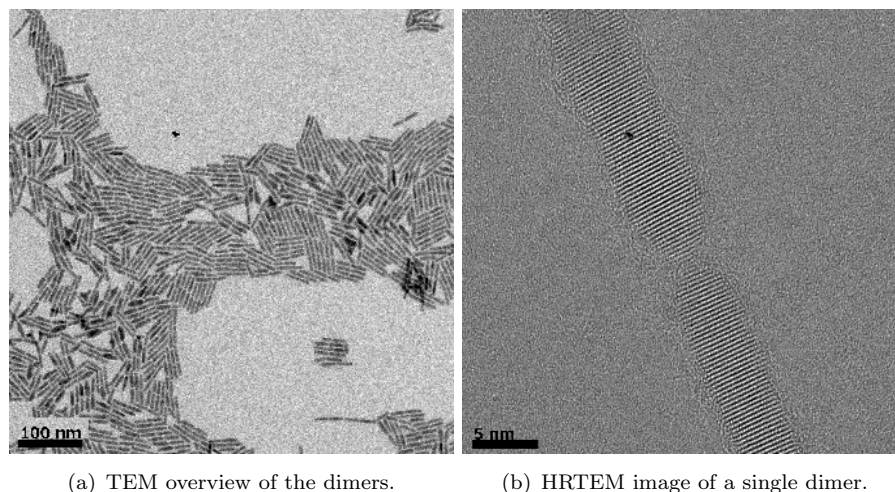


FIGURE 3.2: TEM images of SNR-1.

The SNR are connected at the tips. From fig 3.2 (b) can be deduced, that the SNR do not only lie close to each other, but are somehow interconnected with a distance of less than 2 nm. From the overview image in fig 3.2 (a), it can be seen that this dimerization is no exception and that most of the SNR have dimerized. Nevertheless, only dimers are formed instead of longer chains. It can be supposed, that longer chains would be unstable, as the SNR are linked linearly at the tip and thus at the thinnest point. Further work has to be done in order to understand the reasons why this dimerization occurred.

The point of time, at which the dimerization occurred, can afterwards not be determined. It has to be assumed that all CLSM measurements investigating SNR-1 were performed with SNR dimers.

### 3.1.3 Optical Properties and Quantum Yield

The optical properties were characterized with absorption and emission spectroscopy. The spectra are depicted in figure 3.3. The quantum yields (QY) of the samples are 84

% for SNR-1, 83 % for SNR-2, and 41 % for SNR-3. For this, the emission intensity of the SNR was divided by the emission intensity of the dye Rhodamine 6G.

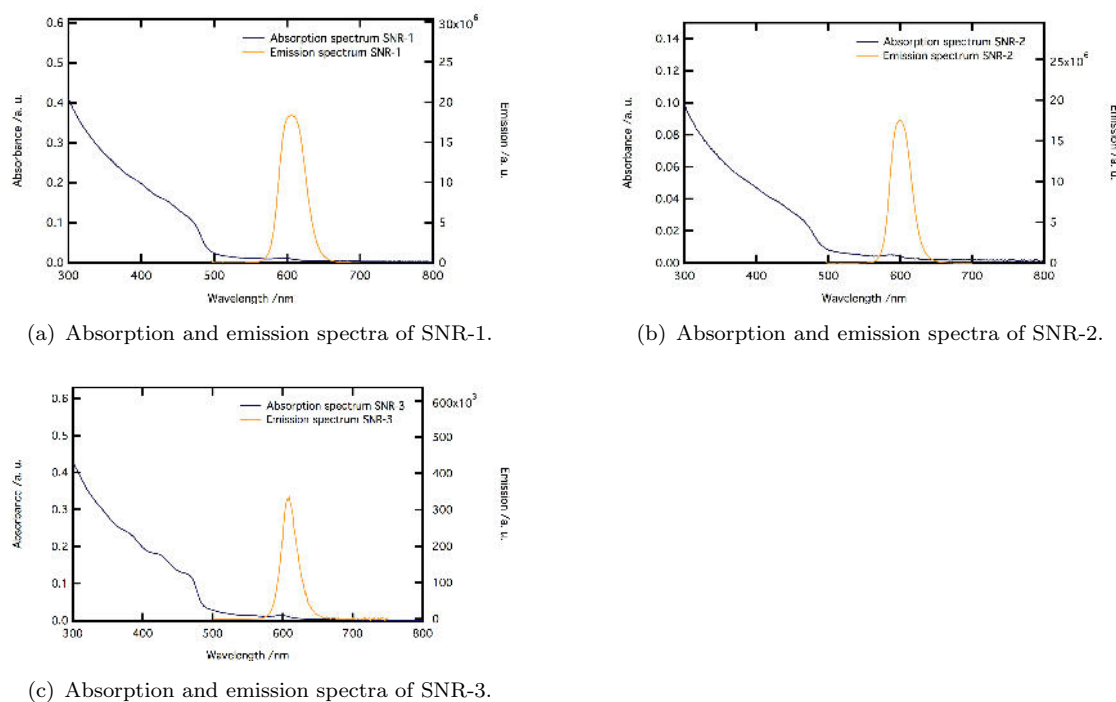


FIGURE 3.3: Optical properties of SNR-1, SNR-2, and SNR-3.

The absorption and emission spectra in fig. 3.3 give some indication about the spectral transitions. The features in the blue absorption spectrum of SNR-1, SNR-2, and SNR-3 from the lowest energy transition are at 598 nm, 589 nm, and 601 nm, respectively. The radiative recombination of these transitions can be seen in the orange emission spectra, with an intense peak at 607 nm, 600 nm, and 610 nm, respectively. In conclusion, the SNR exhibit stokes shifts of 9 nm, 11 nm, and 9 nm.

Overall, the CdSe/CdS dot/rods used for the CLSM measurements were monodisperse and showed a high QY. Nevertheless, the QY of SNR-3 is only half of the QY of SNR-1 and SNR-2, due to improvements in the preparation.

## 3.2 Gold Nanorods

### 3.2.1 Synthesis - Characterization

#### 3.2.1.1 Synthesis according to Nikoobakht et al.

**Size Distribution** The El-Sayed group developed in 2003 a synthesis that is nowadays well-established and used by many groups [94]. In this work, the synthesis yielded monodisperse GNR with less than 5 % shape impurities which can be seen in an exemplary TEM image in fig. 3.4 (a). This was achieved, after sodium boron hydride has been stored and handled under nitrogen atmosphere. The sensitivity of the results on the sodium boron hydrogen trait clearly indicates, that the synthesis is highly dependent on the amount and quality of the seeds. If sodium boron hydride was exposed to air, it partially reacted and the concentration was therefore not constant in different syntheses.

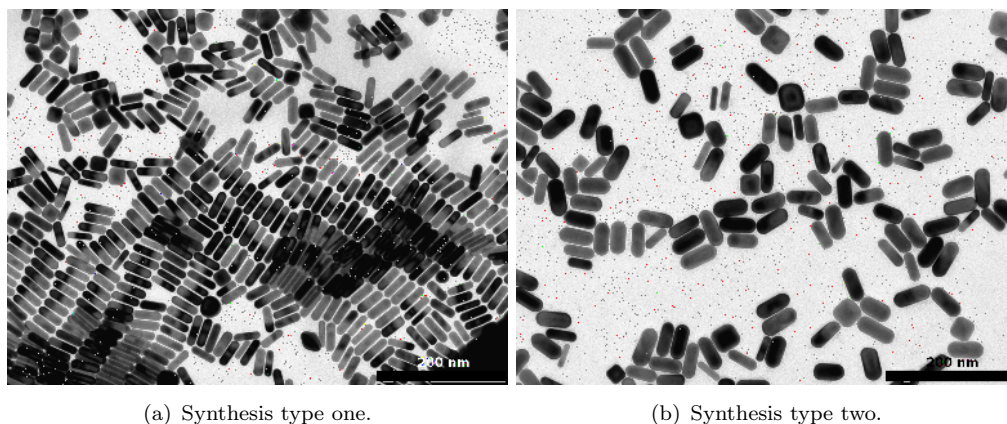


FIGURE 3.4: TEM images of GNR.

After 41 syntheses, suddenly the same and until that point reproducible procedure led to different results. The GNR solution was dark blue/green instead of pale pink. A representative TEM image of these different results are depicted in fig 3.4 (b). Although the GNR are still monodispersely rod-shaped, the dimensions are clearly altered. The size distribution of synthesis type one (first 41 syntheses) and type two (after 41) were determined on the basis of the TEM images.

Type	Length /nm	Width /nm	AR
1	$42.13 \pm 2.44$	$12.60 \pm 1.10$	$3.07 \pm 0.33$
2	$50.07 \pm 4.07$	$21.53 \pm 1.65$	$2.02 \pm 0.24$

The GNR of the type 2 had an increased length and width, but a reduced aspect ratio.

**Optical Properties** The absorption spectra of the the samples were normalized to one and are shown in fig 3.5. The two bands beautifully confirm the rod-structure of the synthesis product, as already explained in 2.2.1.

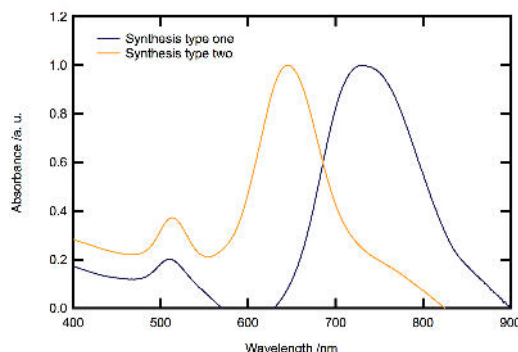


FIGURE 3.5: Absorption spectra of synthesis type one and two.

Synthesis type one shows a TSPR at 510 nm and a LSPR at 734 nm. The TSPR is almost the same for synthesis type two (513 nm), but the LSPR is blue shifted to 646 nm, which explains the different color of the nanorod dispersion. It also reflects the reduced AR, determined with TEM.

It is difficult to find a conclusive reason for this change, as the mechanism is composed of several factors and nothing was changed intentionally in the method. A possible explanation is, that less seeds are formed and less nucleation centers are available for the seeded growth. Consequently, the GNR have increased dimensions. The GNR grow at first along the longitudinal axis and afterwards with a higher growth rate on the longitudinal facets [52]. The decreased AR for the synthesis type two indicates a longer growth process, as the AR is reduced in comparison to synthesis type one. If there are less nucleation centers but the same amount of  $\text{Au}^{+1}$  ions is reduced, it can be concluded that the growth rate at one single GNR is higher, compared to the synthesis with more seeds. It can be assumed, that the longitudinal facets are only blocked until a certain threshold is reached, depending on the reagents concentrations, respectively. If now the growth rate is enhanced, this point is reached faster, and more precursor is left for the reduction on the longitudinal facets. This would result in lower AR GNR, as observed for synthesis type two.



Nonetheless, the transition between synthesis one and two was irreversible, as the sensitive equilibrium between the reactants could not be readjusted easily. As the GNR from synthesis type two exhibit a smaller AR, this synthesis was no longer adequate for this work's purpose. Hence, the just-published synthesis by Ye et al. was adopted. The fact, that this synthesis showed more reproducible properties although it was performed with the same batches of chemicals, confirmed that the change from synthesis type one to type two was not induced by contaminations or that the synthesis developed by Ye et al. is more robust.

### 3.2.1.2 Synthesis according to the Murray Group

**Size Distribution** All synthesis procedures described in 5.1.3.2 were characterized with TEM. In fig 3.7 a representative TEM image of each performed synthesis procedure is shown.

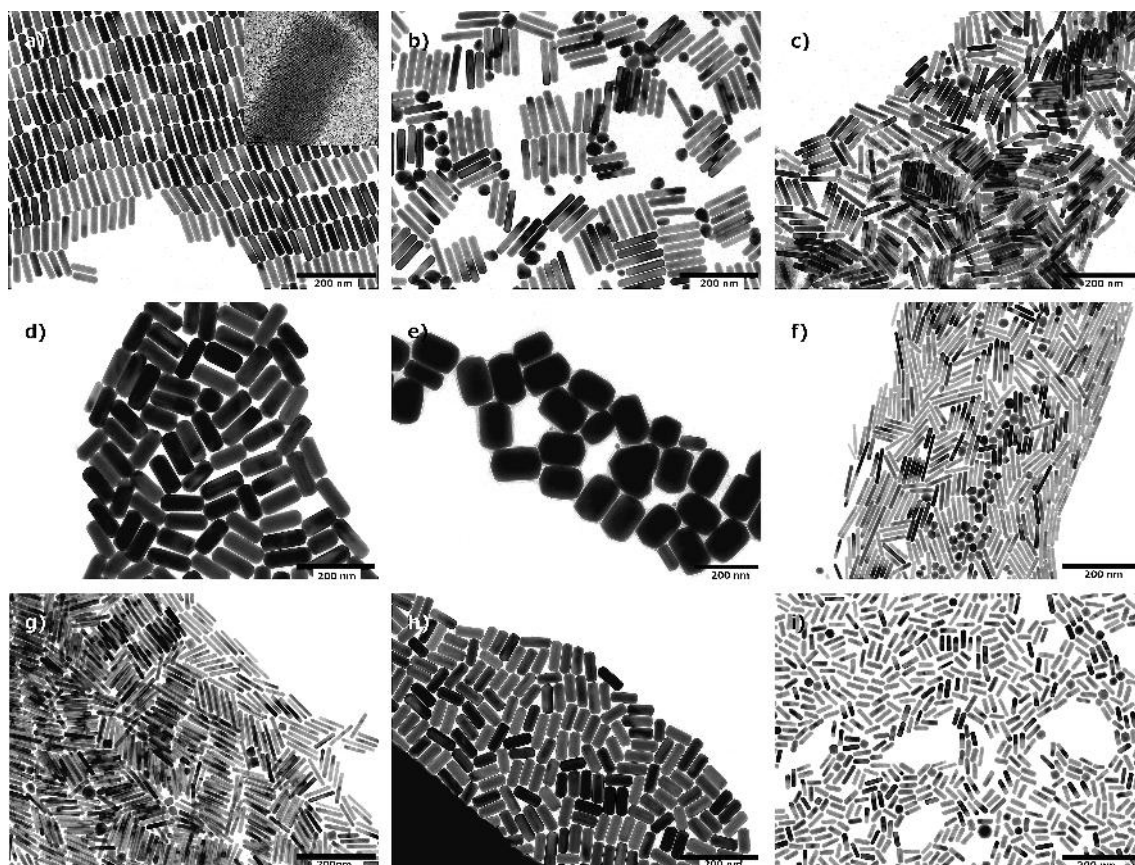


FIGURE 3.6: TEM images from the synthesis variations. Image a)-i) corresponds to synthesis procedure 1-9 respectively.

As the magnification is the same in all 9 TEM images, the resulting GNR are perfectly comparable. An inset in fig. 3.7 (a) proves the crystallinity of the rods. 200 nanorods (length and width and the corresponding AR) were measured and the size distribution was determined. The resulting dimensions of the syntheses and the standard deviations are listed in the table below. For synthesis no. 6 two size distributions are given due to a large amount of spherical impurities. The first line belongs to the rod-shaped particles and the line below to the spherical ones.

Nr.	Length /nm	Width /nm	AR
1	74.69±6.92	17.25±2.04	4.19±0.86
2	112.68±8.23	20.37±2.44	5.67±0.63
3	75.40±6.67	13.63±1.41	5.57±0.57
4	107.6±7.78	43.58±2.24	2.50±0.22
5	153.79±5.32	103.76±3.16	1.50±0.13
6	62.17±13.33	9.01±1.29	6.95±1.67
	26.48±1.95	19.47±1.66	1.22±0.12
7	76.35±9.04	10.97±1.04	6.91±0.87
8	71.28±5.18	26.07±1.86	2.72±0.27
9	42.56±5.42	12.48±1.14	3.35±0.53

With the synthesis procedures by Ye et al., a broad range of aspect ratios from, 1.50 to 6.95, can be synthesized. The standard synthesis (no. 1) leads to highly monodisperse GNR with a negligible amount of spherical impurities. The inset in fig 3.7 (a) demonstrates the crystallinity of the GNR. Unfortunately, this monodispersity could not be achieved for all synthesis procedures. This result stands in contrast with the results by Ye et al., who reported high monodispersity for all procedures [131].

From the TEM images it can be deduced that procedures for comparably long GNR with high aspect ratios tend to lead to a bimodal size distribution with a high part of spherical impurities.

Regarding the utilized reagent concentrations, the results suggest that a higher amount of silver nitrate produces more shape impurities. Relative to the other syntheses, in synthesis number 2,3,6 and 7 corresponding to the TEM images (b), (c), (e) and (f), respectively, at least 24 mL of the 4 mM silver nitrate solution was used. The images

show a considerable amount of non-rod-shaped particles. Nevertheless, the clear connection of a reagent variation and a result is not trivial. The influences of the different reagents show no clear trend. This is not completely surprising, as the mechanism of this synthesis is still not undoubtedly elucidated (2.2).

**Optical Properties** The absorption spectra of the synthesis procedures in 5.1.3.2 are shown in fig. 3.7. The spectra are normalized to one.

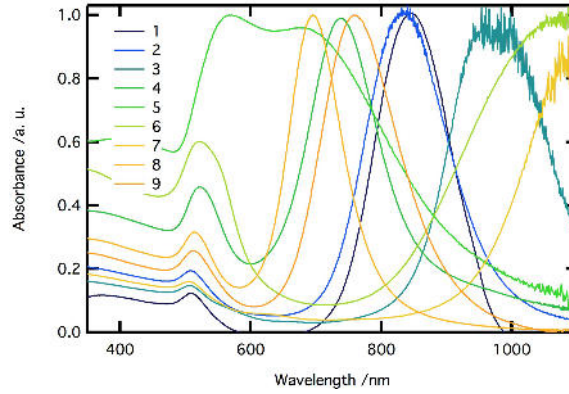


FIGURE 3.7: Absorption spectra of the different synthesis procedures.

The spectra and their LSPR position beautifully reflect the different aspect ratios determined with the TEM characterization. The LSPR of larger AR is red-shifted compared to the LSPR position of smaller AR. However, regarding the different normalized spectra, it becomes obvious that the spectra vary in their absorbance off-set between TSPR and LSPR. GNR procedures with similar AR and dimensions show a comparable off-set. When two batches have the same AR but different length and width, the sample with bigger dimensions shows a higher absorbance, which is in agreement with the higher absorption and scattering cross section. The width of the LSPR is consistent with the monodispersity of the sample. Especially for samples with a lot of shape impurities both plasmon bands are broadened. In general, the optical properties agree with the TEM images. For a monodisperse GNR sample, the LSPR and TSPR have a ratio of 1 : 10 [123]. This criterion is fulfilled for all spectra except of synthesis 5. This observation also agrees with the TEM data (fig. 3.7 (e)) and the high amount of shape impurities. Spectrum 5 exhibits not only a less intense LSPR but also a broadening which is caused by the polydisperse size distribution.

### 3.2.1.3 Growth Monitoring

The standard synthesis was monitored by time-resolved UV/Vis spectroscopy during the growth. The resulting spectra are shown in fig. 3.8.

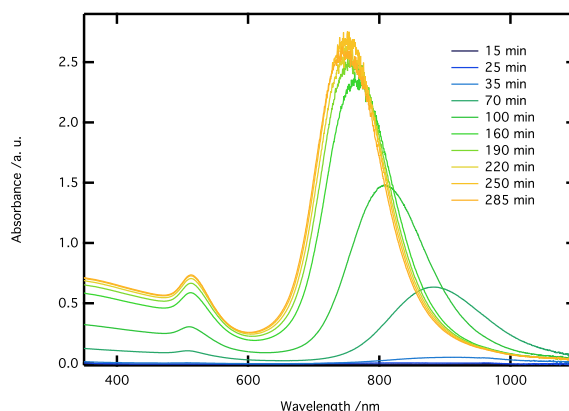


FIGURE 3.8: Absorption spectra taken during the GNR growth.

The spectra show a shift of the LSPR to smaller wavelengths during the growth. As the LSPR depends on the AR of the rods, the optical properties during growth reveal the growth kinetics. Initially, the GNR grow along the  $\langle 001 \rangle$  axis, exhibiting a LSPR at higher wavelengths. After 35 minutes growth time, the LSPR shifts towards smaller wavelengths, meaning a decrease in AR. Thus, the growth at the longitudinal facets is faster than the one at the tips. After 160 minutes, the LSPR more or less stabilizes, which means that the AR does not change anymore. After this point, the growth rates on the longitudinal and transversal facets are similar and only the overall absorbance increases. The GNR grow in both directions simultaneously and at a similar speed. The growth kinetics agree well with the published data [52].

### 3.2.1.4 Influence of the different Parameters

The parameters of the reaction were varied, starting from the standard synthesis. The absorption spectra of the products are depicted in fig 3.9.

The sodium boron hydride concentration reduction of a factor of 0.166 did not result in a reaction at all. No color change was induced by the addition of the reducing agent. Thus, the necessary reduction potential was too low to exceed the supersaturation limit, which would have started the nucleation.

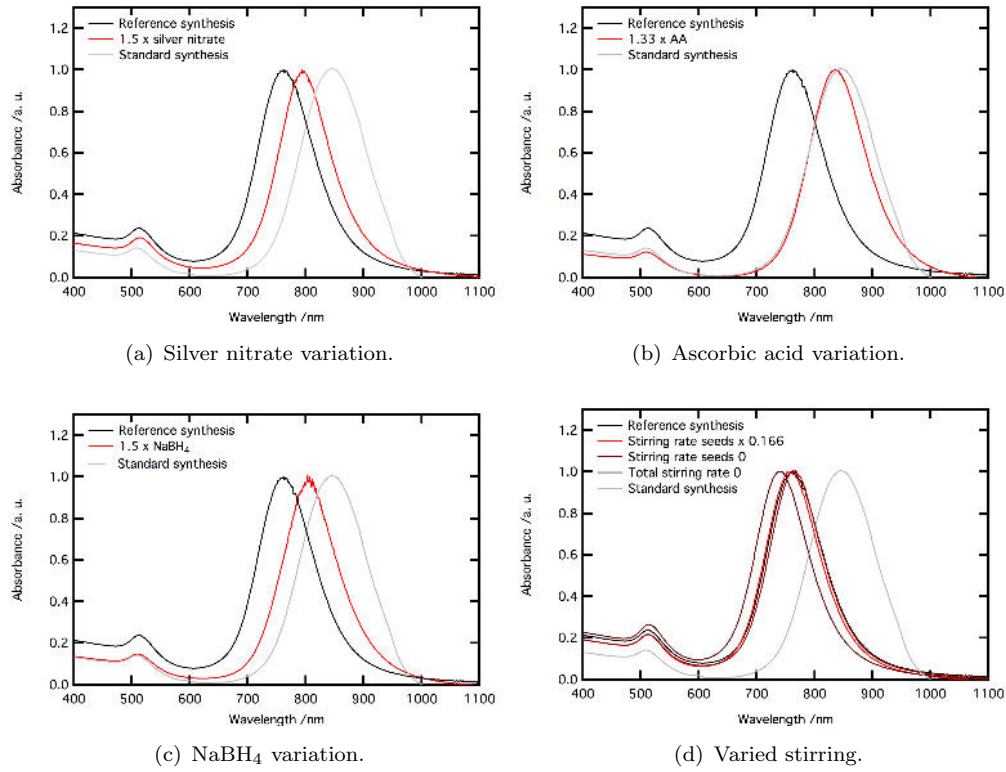


FIGURE 3.9: Absorption spectra from the parameter variations.

The red spectra in fig 3.9 show the optical properties from the varied synthesis, respectively. The grey spectra are from the standard synthesis which was discussed above. Parallel to the variations, a synthesis with standard procedure was performed and is called reference synthesis (black spectra) in the following.

Firstly, what is rather evident from fig. 3.9 is that the standard and reference synthesis differ remarkably in their LSPR band position, although being based on the same synthesis procedure. One has to conclude, that the reaction without any varied parameters shows a fluctuation in the AR. Furthermore, since none of the LSPR of the red spectra is broadened, it can be deduced that the varied parameters did not have a severe influence on the monodispersity of the GNR. This was confirmed by the TEM images (see appendix fig. A.1). The position the LSPR bands of all red spectra is in between the ones of the reference synthesis and the standard synthesis. Thus, the AR variation is inside the reproducibility thresholds of the synthesis. Overall, the only conclusion that can be drawn from these variations, is that the the production of the seeds is a crucial parameter. Not surprisingly, the necessary concentration of the reducing agent has to be injected to overcome the critical concentration for nucleation. Besides this, the reaction

turned out to be very robust within the varied boundaries.

### 3.2.2 Ligand Exchange

#### 3.2.2.1 Octadecanethiol

After the ligand exchange with octadecanethiol and subsequent lyophilization, the solid is redispersible in toluene and chloroform. Nevertheless, the solution appears more purple, in comparison to the aqueous GNR dispersion. The TEM characterization reveals the following results:

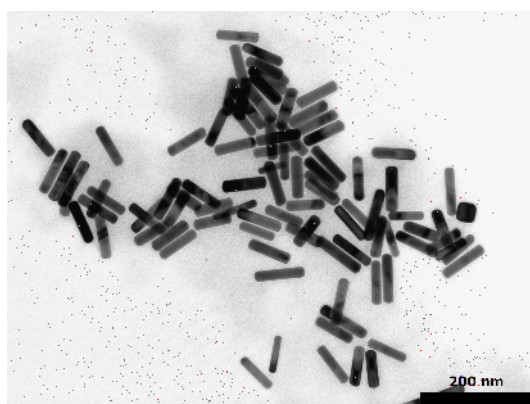


FIGURE 3.10: TEM image of the standard synthesis after the transfer to chloroform.

The GNR obviously maintained their shape. The size distribution, determined based on the TEM data, confirmed the steady dimensions. In contrast to this, the absorption spectra depict altered optical properties:

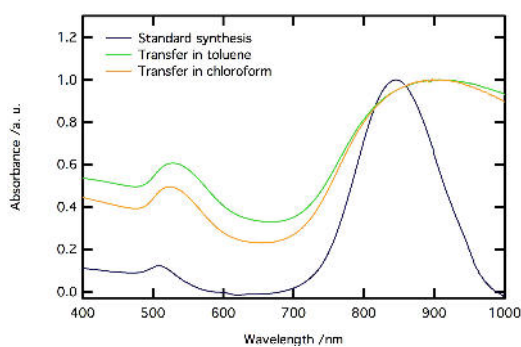


FIGURE 3.11: Absorption spectra of the standard synthesis before and after the transfer to chloroform and toluene, respectively.

All three spectra in fig. 3.11 are normalized to one. While the standard synthesis shows a ratio of 10:1 (LSPR absorbance to TSPR absorbance) with a LSPR wavelength of

845 nm, the spectra in toluene and chloroform show a broad LSPR around 900 nm and the ratio between LSPR and TSPR is only 2:1 (in chloroform) and 3:1 (in toluene). In addition to this, the spectra in organic solvents have a larger absorbance off-set. The spectrum in toluene shows, additionally to the larger width, a slight red shift compared to chloroform.

Since the aspect ratio and monodispersity of the GNR in organic solvents did not change according to the TEM evaluation, the modification affects only the optical properties. These results are in good agreement with the dependence of the GNR optical properties on the refractive index. The refractive index of water at 845 nm is 1.3290, while it is 1.4368 and 1.4839 at 900 nm for chloroform and toluene, respectively [48, 63]. Perez-Juste et al. discussed the influence of the refractive index according to Gans theory. Also experimentally, they found a linear dependence of the LSPR position on the refractive index of the solvent. The increased peak absorption and width is confirmed in their review. This sensitivity of the LSPR peak on the refractive index is more and more intensified when the AR of the rods increases. The peak position  $\lambda$  can be described with the following relation:

$$\lambda^2 = \lambda_p^2 (\varepsilon^0 + \varepsilon_m (\frac{1}{L} - 1)) \quad (3.1)$$

where  $\lambda_p$  is the plasmon frequency of the metal,  $\varepsilon^0$  is the initial dielectric constant,  $\varepsilon_m$  the dielectric constant of the medium and  $L$  the depolarization factor [103]. They calculated absorption spectra for GNR with an AR of 3.5 in different solvents. A strong red shift with increasing polarizability of the solvent substantiates the experimental results.

In conclusion, the red shift for higher refractive index/more polarizable solvents can be explained with Mie-Gans-theory. The experimental results from GNR after the ligand transfer to octadecanethiol and the transfer into an organic solvent exhibited different optical properties according to the changed dielectric environment.

### 3.2.2.2 PEGMUA - Cyanide Etching

The exchange of the CTAB bilayer with the polymer opens the door for biological and medical application. For this very reason, the ligand exchange has to be complete, as CTAB exhibits cytotoxicity. Whether the PEGMUA has entirely substituted CTAB, and thus whether the CTAB was removed quantitatively, can be evaluated with oxidative cyanide etching. The charged CTAB ligand shell does not protect the GNR towards cyanide ions over time.

**Etching of Extracted Samples - Monitoring** In contrast to other ligand systems such as citrate stabilized gold nanoparticles, the ligand exchange with the polymer does not take place immediately after ligand addition. When KCN was added to fresh stock solutions with GNR and PEGMUA (without incubation), the rods were instantaneously dissolved. Thus, the polymer was still free in solution and did not bind to the GNR.

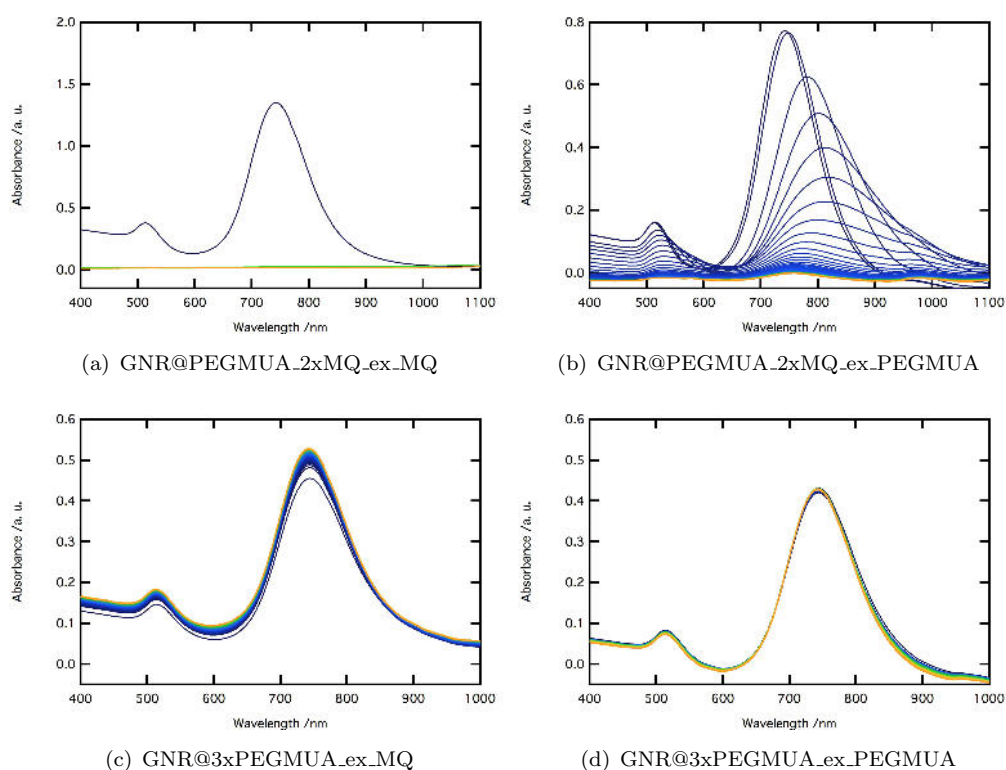


FIGURE 3.12: Monitoring of the extracted samples in 25 mM KCN, interval 5 min. (a) stock solution that was washed only once with PEGMUA, stabilized with water after the extraction, (b) stabilized with PEGMUA solution after extraction, (c) stock solution that was washed three times with PEGMUA, stabilized with water after the extraction and (d) stabilized with PEGMUA after extraction.



Based on these pretrials, the CTAB system was destabilized by extraction with chloroform, where the in chloroform well-soluble CTAB migrated to the organic phase. After the extraction, either a PEGMUA solution or the same volume of ultrapure water was added. In the following, a preparation dependent nomenclature is used for the different samples. It summarizes chronologically how the samples were treated before the cyanide etching was started. The @ symbol emphasizes the ligand exchange wherefore the GNR should now be stabilized by the polymer ligand instead of CTAB. In general, there are two different stock solutions: GNR@PEGMUA\_2xMQ and GNR@3xPEGMUA. The CTAB stabilized solution was after synthesis for the preparation of both stock solutions centrifuged for three times. In the first stock solution, the centrifugate was substituted once with PEGMUA solution and twice with water, while for the second stock solution the centrifugate was replaced three times with polymer solution. The term \_ex stands for extraction and the following abbreviation represents with which solution (MQ water or PEGMUA) it was stabilized afterwards. For a detailed description of the proceedings see 5.1.5. The time resolved UV/Vis-spectroscopy with results of the etching in 25 mM KCN solution are shown in fig. 3.12. During the ongoing etching reaction a spectra was taken every 5 minutes.

It is rather obvious, that the sample which was washed once with PEGMUA solution before the extraction (GNR@PEGMUA\_2xMQ\_ex\_MQ) is still CTAB stabilized after extraction and ultrapure water addition. The absorbance vanishes completely in less than 5 minutes, which indicates the complete oxidative etching (graph (a)). This proves, that the amount of PEGMUA present after one washing step was not enough to replace CTAB, with additional destabilization.

On the contrary, the spectra of the GNR sample washed for three times with PEGMUA solution before the extraction (GNR@3xPEGMUA\_ex\_MQ) did not change (besides a shift in the baseline which can be attributed to a measuring inaccuracy, graph (c)). Even though no polymer ligand has been added after the extraction, there was sufficient free PEGMUA in the solution to stabilize the destabilized GNR. Not surprisingly, when to the stock solution GNR@3xPEGMUA, PEGMUA was added after the extraction, the GNR were stable towards etching, too, (graph (d)). This indicates a quantitative ligand exchange.

In graph (b) the spectra of the stock solution GNR@PEGMUA\_2xMQ to which PEGMUA was added after the extraction are shown. The GNR show a higher stability towards KCN than the sample which was stabilized with ultrapure water (MQ) after the extraction. Nevertheless, the absorbance is almost zero after approximately 60 minutes. The ligand exchange appears to be not quantitatively, so that the remaining CTAB provides possible etching sites for  $\text{CN}^-$  ions. Interesting here, is how the spectra change with time. The LSPR does not only decrease in absorbance, but is also broadened and red shifted during the etching process. The spectra even allusively show a second peak after some time at higher wavelengths. This can be interpreted to the effect that when the etching process is started, a defect site is created in the GNR ligand shell. But instead of completely dissolving, the GNR are restabilized by free PEGMUA from the solution. The affected GNR have now a partially decreased width and hence, at the attacked sites an increased aspect ratio, leading to a longer wavelength LSPR. Thus, the second two overlapping peaks evolve due to different widths of the GNR (sometimes even in one single GNR).

This proposed mechanism of how the GNR are etched by cyanide was confirmed with TEM. For this experiment, the etching rate was increased by the double KCN concentration. Samples were taken and investigated with TEM after 30, 50 and 70 minutes. Representative images are depicted in fig. 3.13.

Only a minority of the GNR in image (a) show damages after 30 minutes etching. Interestingly, instead of the complete dissolution of a GNR once attacked by cyanide, the PEGMUA from solution stabilizes the pitted areas. After 50 minutes (image (b)), the etching reaction has proceeded and more GNR exhibit wormhole-like sites, while others remain completely unchanged. This development agrees perfectly with the spectroscopic data. The wormhole-like defect sites, create areas of smaller width, with higher AR. This changed geometry results in the optical feature at longer wavelengths. The initial LSPR is red-shifted and broadened due to the reduced monodispersity. Image (c) after 70 minutes depicts the advanced etching reaction. Only few GNR have retained their shape and resisted the cyanide reaction. From most of the GNR only the "skeleton" is left. Based on the relatively undamaged GNR, it can be assumed that the probability that an already attacked GNR is etched further, although being restabilized, is higher than the evolution of a completely new etching site. The etching sites seen in the TEM images are in agreement with the findings by Jana et al. for high AR GNR [56]. Although their

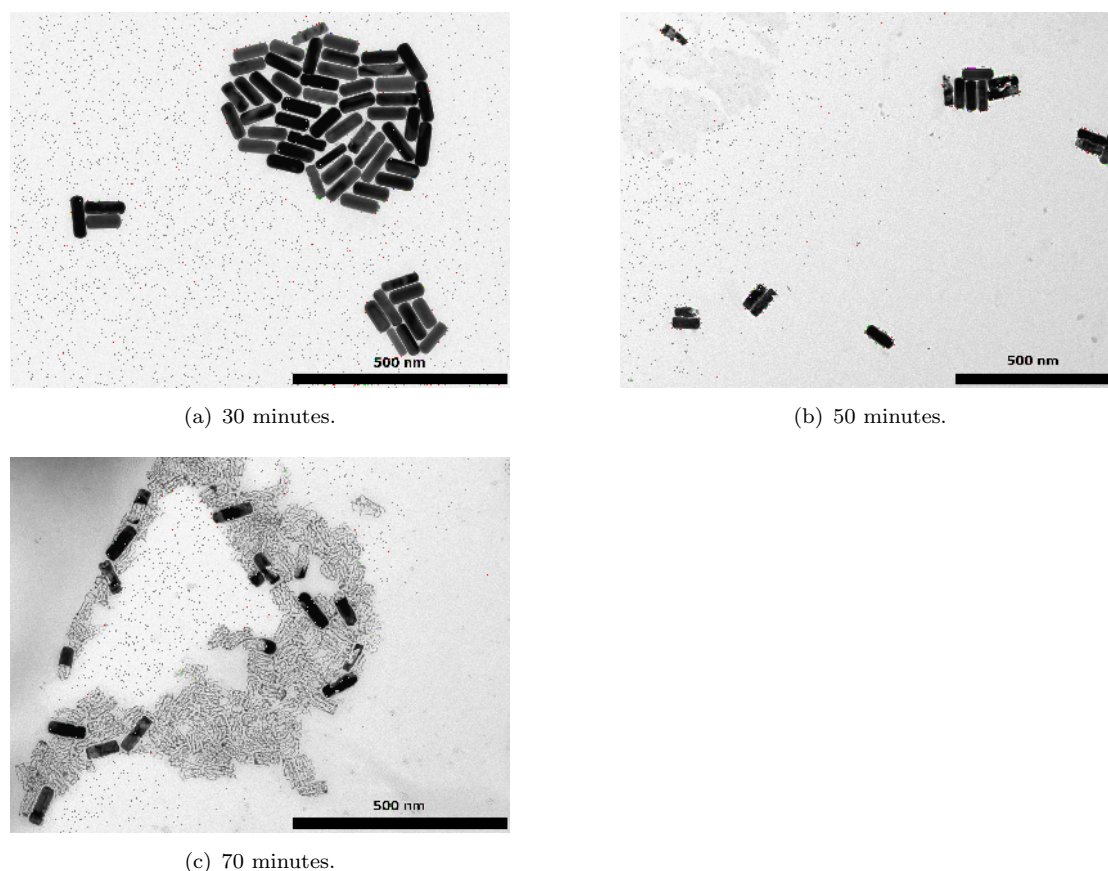


FIGURE 3.13: TEM monitoring of the cyanide etching.

explanation that defect sites in the crystal are advantageously attacked seems plausible, the fact that another etching mechanism is observed for the exact same GNR synthesis batch (see fig. 3.14) makes a ligand shell based mechanism more likely. The etching mechanism depends on the complete or incomplete polymer ligand shell and possible restabilization of already attacked sites by free PEGMUA, instead of on defects in the GNR crystallinity.

Overall, the thorough washing of the GNR with PEGMUA for three times sets the basis for the ligand exchange. If the GNR are only washed once before the extraction, a worse result is obtained. Although the extraction seems to be a prerequisite for the immediate ligand exchange (without incubation time), the ligand exchange is facilitated when the polymer is present in solution during the destabilization. The PEGMUA addition afterwards cannot lead to the same polymer stabilization. The polymer ligand has to be present in large excess during the extraction, in order to accomplish a qualitative ligand exchange.

In general, from these experiments it can be concluded, that the addition of PEGMUA after the extraction provides a closer polymer ligand shell. This raises the question, if the subsequently added PEGMUA contributes to the ligand shell or if the higher concentration in solution generates a competing ligand binding rate. For a better understanding, the samples with PEGMUA addition after the extraction were purified (washed with ultrapure water). The resulting spectra are shown below.

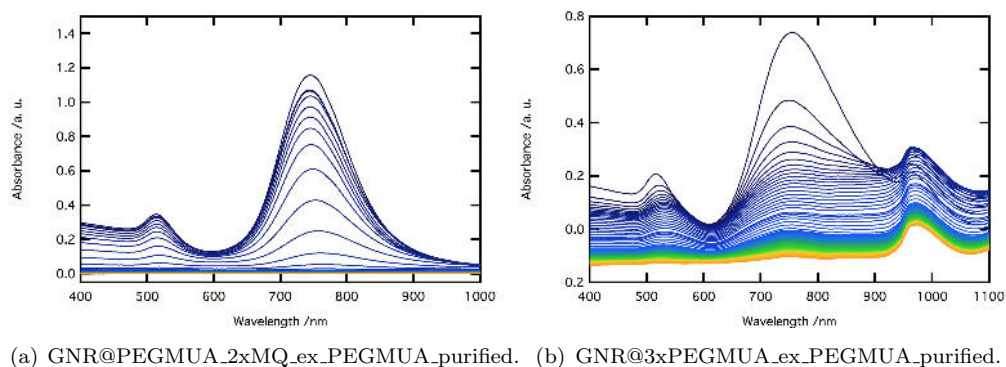


FIGURE 3.14: Monitoring of the purified extracted samples in 25 mM KCN, interval 10 min.

Both stock solutions show a different behavior in the UV/Vis monitoring with purification than without. Both show a decreased resistance against cyanide, which means a reduced stabilization by PEGMUA. While the stock solution that was washed with PEGMUA for three times seems to react under the same mechanism as observed before, the etching of the stock solution washed only once with PEGMUA before the extraction shows a different temporal evolution. The LSPR in graph (b) is shifted to longer wavelength with the generation of a second band as in fig 3.12 (b). However, the wavelength of the LSPR in graph (a) remains constant while its intensity is reduced. This behavior suggests that there is just a decrease in GNR concentration and no change in shape. It indicates, that the PEGMUA concentration in solution is below a critical concentration, so that already etched sites cannot be restabilized. A rod that is once attacked, is dissolved completely by KCN.

**Etching - How much PEGMUA is needed?** A large excess of PEGMUA is needed for a ligand exchange. After all, the economical aspect of this ligand exchange should not be ignored. Hence, the applied amount of polymer ligand has to be minimized. The critical concentration for the stabilization was investigated by concentration series.

At first, different amounts of PEGMUA were added and incubated for 16 h without extraction. The samples were tested against cyanide etching. This series is compared with equally prepared purified samples. In these experiments, only the GNR stability and not the LSPR position was evaluated over time. Thus, the absorbance at 450 nm is plotted ( $A_{450}$ ) against the PEGMUA concentration.  $A_{450}$  is concentration-sensitive but relatively insensitive towards shape. The corresponding graphs are depicted in figure 3.15.

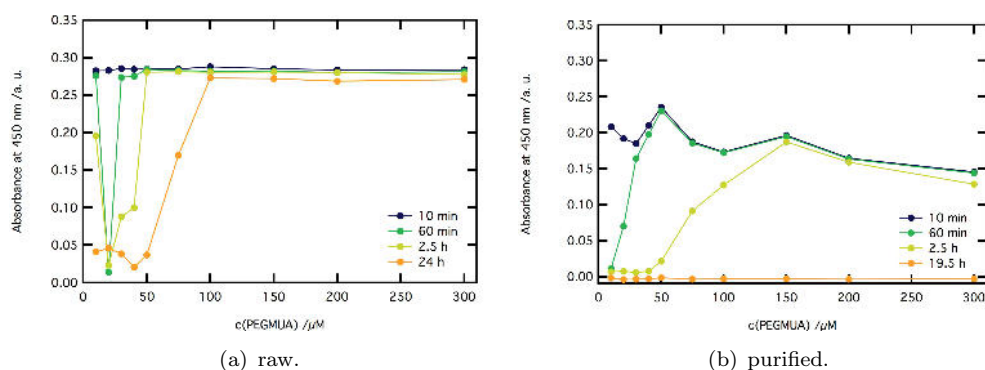


FIGURE 3.15: Absorbance at 450 nm for different PEGMUA concentrations incubated for 16 h.

The total absorbance of the purified samples in the right plot is lower due to material losses during centrifugation. In fig 3.15 it is obvious, that the unpurified samples are in general more stable. The raw samples with a PEGMUA concentration above 100  $\mu\text{M}$  are resistant against 25 mM KCN even after 24 h, while the purified samples are completely dissolved for all PEGMUA concentrations at this time. Even after 2.5 h at least 150  $\mu\text{M}$  PEGMUA is needed to stabilize the ligand shell of the purified samples, while the raw samples withstand KCN with only 50  $\mu\text{M}$  PEGMUA. This critical concentration is even lower for shorter times after the KCN addition. Overall, as the long-time stability is the aspect of most concern, a PEGMUA concentration of at least 100  $\mu\text{M}$  is needed. The free PEGMUA in solution is necessary for a stable ligand shell, as the ligand shell is otherwise incomplete.

Fig. 3.15 shows results of unextracted GNR samples. Naturally, the influence of the extraction on the critical PEGMUA concentration is of great interest. As the monitoring experiments showed that PEGMUA addition before the extraction improves the stability even without incubation time, different amounts are added and incubated for 16 h before the extraction and concentration series afterwards.

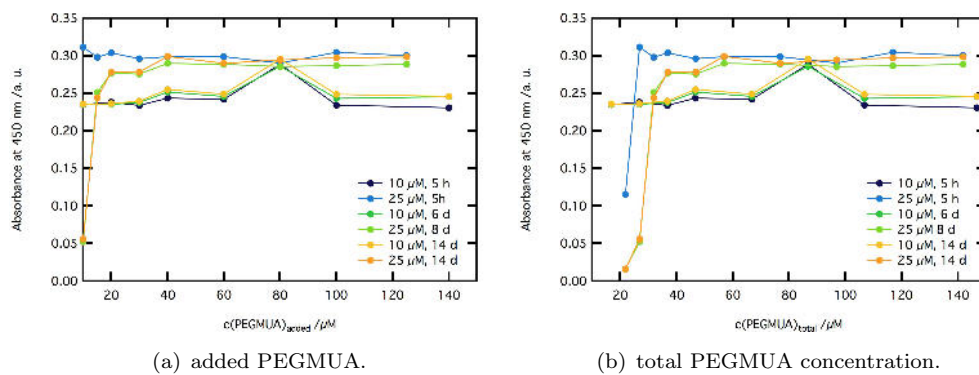


FIGURE 3.16: Absorbance at 450 nm for different PEGMUA concentrations, 10  $\mu\text{M}$  and 25  $\mu\text{M}$  PEGMUA addition before extraction.

Fig 3.16 confirms, that the extraction facilitates the ligand exchange, also with incubation time. This is in agreement with the data from the monitoring experiments, as they already indicated an improved stabilization with extraction. The GNR have a close PEGMUA ligand shell and are therefore resistant against cyanide etching, even for 14 d. If the PEGMUA concentration was adjusted to 25  $\mu\text{M}$  before the extraction, only at least a concentration of 10  $\mu\text{M}$  had to be added. Above this concentration, the absorbance and thus the concentration was stable over the entire evaluation period. If the PEGMUA concentration was 10  $\mu\text{M}$  before the extraction, only an at least 20  $\mu\text{M}$  PEGMUA addition stabilized the polymer shell. As the difference is not drastic for a concentration between 10 and 25  $\mu\text{M}$  PEGMUA before the extraction, especially in the total concentration, a 10  $\mu\text{M}$  PEGMUA concentration is chosen for the following experiments.

The influence of the incubation time before the extraction becomes even overt in fig 3.17. While the samples that were incubated for 16 h had a close and time-stable ligand shell with a PEGMUA concentration of 20  $\mu\text{M}$  or more, at least a concentration of 80  $\mu\text{M}$  PEGMUA was unavoidable for the 2 h incubated GNR. Again, the critical concentration was reduced with decreasing etching time.

Towards the overall goal of this experiment: to vet the different ligand exchange methods regarding the utilized amount of PEGMUA, all concentration series are plotted in one graph in fig. 3.18. The purified samples without extraction are not included in this illustration, as they were not stable enough. The cyanide etching may serve as a ligand exchange test for GNR in general and can be transferred to other ligand systems. A

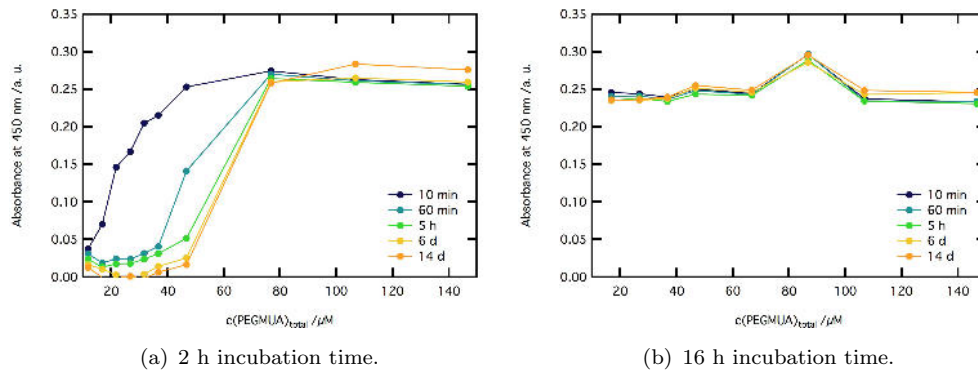


FIGURE 3.17: Absorbance at 450 nm for different PEGMUA concentrations, 10  $\mu\text{M}$  PEGMUA concentration before extraction with different incubation times.

prerequisite for this is a higher/lower temporal stability against cyanide etching than the reference system which is in this case CTAB.

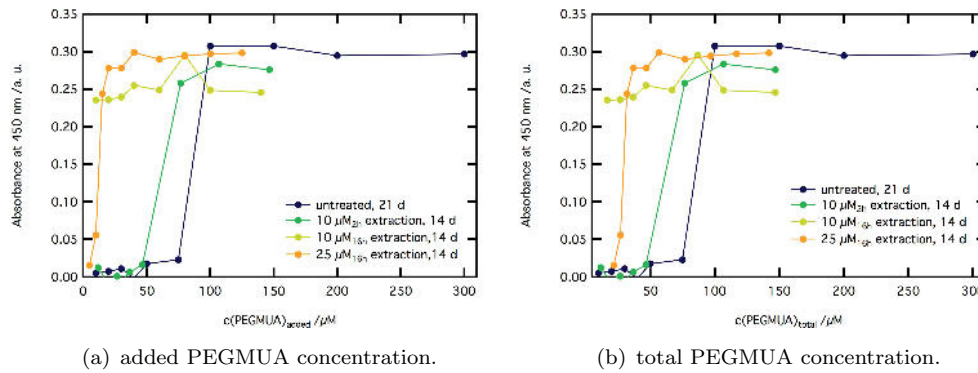


FIGURE 3.18: Absorbance at 450 nm for all experiments after at least 14 d 25 mM KCN exposition/reaction.

Graph (a) and (b) show the added PEGMUA and the total PEGMUA concentrations, respectively. Both graphs reveal clearly the required PEGMUA concentrations for a close ligand shell. Only the completely close shell in comparison to the charged  $\text{CTA}^+$  bilayer prevents the instantaneous oxidative etching by cyanide. While without extraction a higher PEGMUA concentration is mandatory, the required amount of PEGMUA is reduced when excessive CTAB is extracted. If the GNR are incubated in 10  $\mu\text{M}$  PEGMUA solution for 16 hours, the amount of applied PEGMUA is only one tenth of critical concentration for the unextracted samples (10  $\mu\text{M}$  instead of 100  $\mu\text{M}$ ).

Based on the performed experiments, a three-step ligand exchange procedure seems to be most promising:

- 1. Incubation with PEGMUA
- 2. Extraction with chloroform
- 3. Stabilization with PEGMUA

This procedure guarantees the ligand exchange with a biocompatible polymer ligand.

### 3.3 Ordered GNR Assemblies

In order to develop a substrate with ordered GNR for the optical measurements the assembly process had to be understood. The GNR alignment in a controlled manner, demands a profound understanding of the GNR-GNR interaction.

#### 3.3.1 Establishing a Fabrication Method

A variety of possible fabrication methods was explored. The different interactions were studied via a matrix of substrates and film deposition techniques.

##### 3.3.1.1 Film Deposition Techniques

**Spin Coating** An in the group well-established preparation method for gold nanoparticle films with layer-by-layer spin coating set the basis for the spin coating experiments from solution [111]. The deposition was tested with various rotational speeds and with several layers of highly concentrated GNR in aqueous solution. Nonetheless, due to the low wettability of the solvent, these experiments led to extremely low coverages of arbitrarily distributed horizontal GNR. The hydrophilisation of the substrate or the improvement of the wettability with addition of ethanol or dioxane did not show any improvement.

Consequently, GNR in organic solvent were tested. The solvent of choice was toluene, being commonly used for spin coating. Although resulting in a slightly higher coverage,



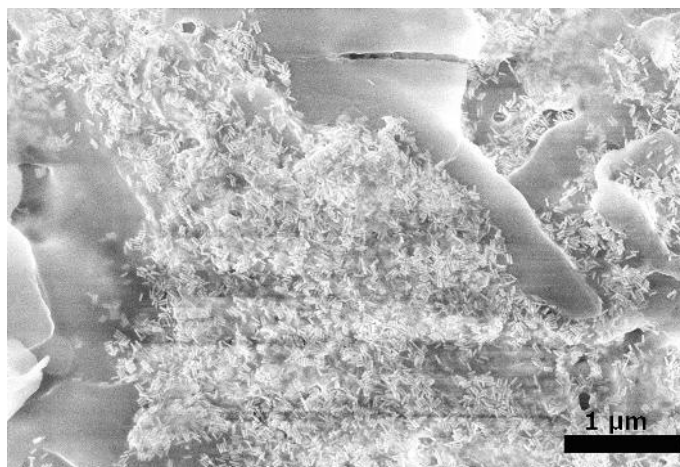


FIGURE 3.19: SEM image of octadecanethiol stabilized GNR deposited via spin coating.

still not enough GNR were deposited on the substrate and they did not show any ordering. In addition to this, too much ligand had to be used for the GNR stabilization, so that organic contamination was visible in the SEM images, as exemplarily shown in figure 3.19. The GNR are not ordered and are embedded and/or covered with organic contamination, which is imaged unstructured in the SEM image. Due to the lack of conductivity it causes a charging of the sample.

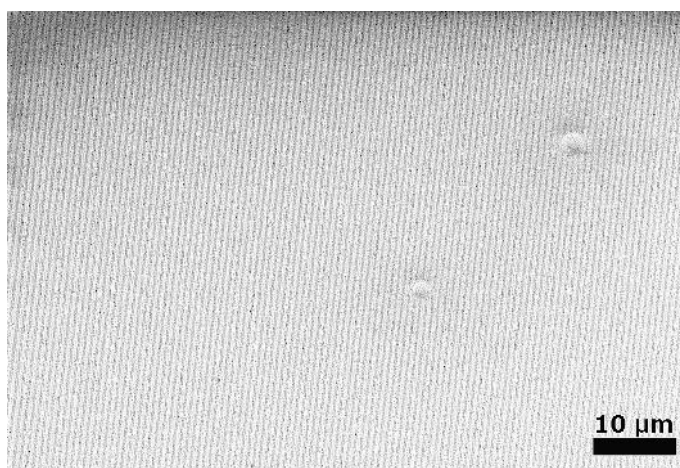
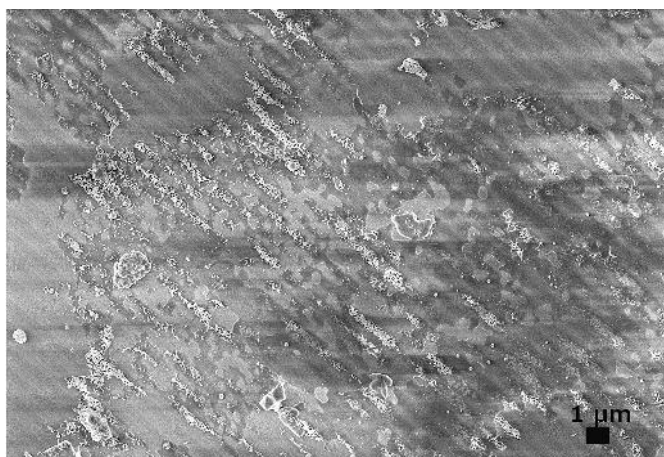


FIGURE 3.20: SEM image of the patterned substrate.

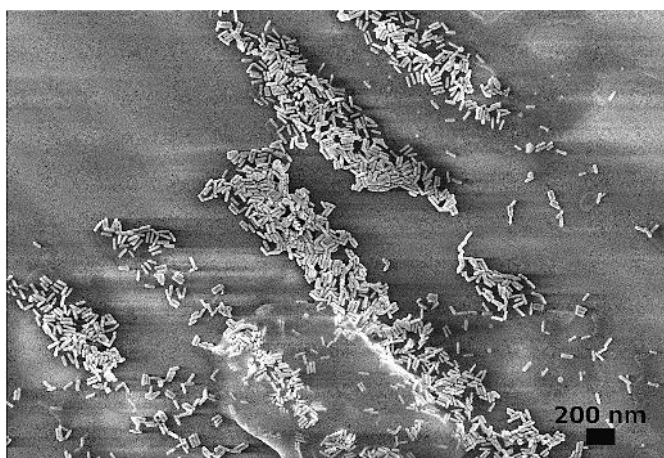
In another spin coating approach  $\mu$ -patterned substrates that were fabricated with a stamping technique. These glass slides with silicate or polystyrene patterns were used as spin coating substrates. In previous projects, this was found to be a successful method to produce patterned gold nanoparticle samples [84].

Fig. 3.20 shows a SEM image of such a periodically patterned substrate. As can be seen, TMOS and PS patterns over several  $\text{mm}^2$  can be produced.

Nevertheless, the approach of the GNR self-assembling in the channeling of the pattern did not lead to the desired result. In organic solvent with octadecanethiol as ligand, the ligand excess led to similar results as for unpatterned substrates (fig. 3.19). No orientation of the on the pattern can be observed.



(a)



(b)

FIGURE 3.21: SEM images of GNR in aqueous solution with dioxane addition spin coated on a patterned substrate.

In aqueous solution the GNR arranged in drying rings, without any change due to the pattern. Dioxane addition for increased wettability reduced the drying rings. The GNR assembled according to the pattern, as shown in fig. 3.21 (a). Nevertheless, the SEM image in fig. 3.21 (b) with a higher magnification does not show an ordering of the

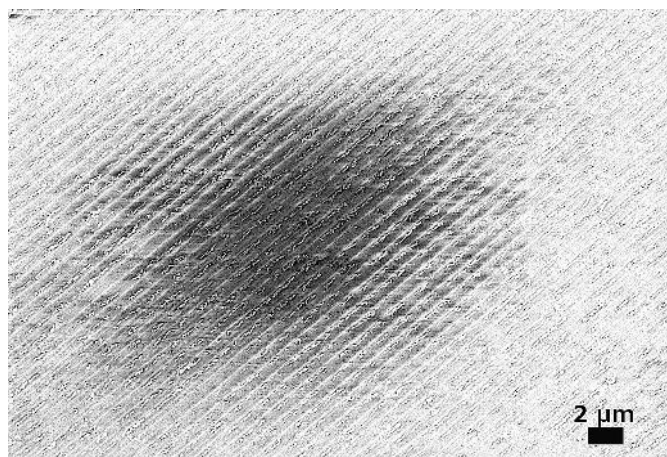
GNR. They form an arbitrary arrangement. Another negative influence was, that the solvent dissolved the pattern partially, visible in the indefinite contours of the pattern.

Overall, spin coating cannot be used for the ordering of the investigated GNR systems.

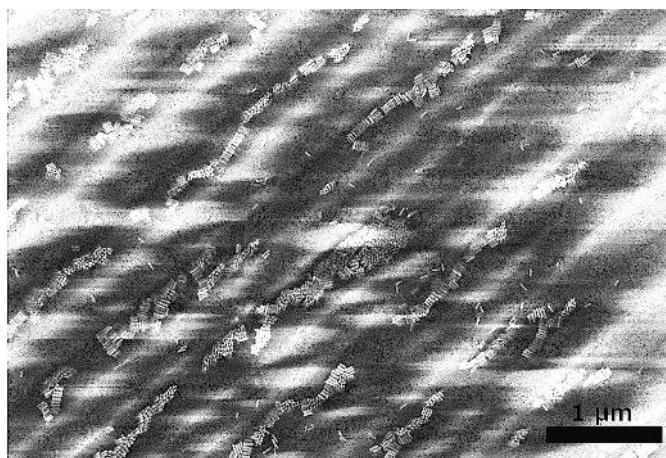
**Dip Coating** The technique uses the solvent's capillary effects. The model of convective deposition is based on the slow draw out of the wettable substrate from the solution. The particle size should be chosen slightly larger than the thickness of the meniscus on the substrate [22]. The wettability of the TMOS or PS structures (either thin PS film or a PS pattern) was intrinsically very low. Although it could be slightly improved with oxygen plasma treatment, the still too low wettability and weak surface adhesion were the reasons for the small amount of material deposition. The best results were obtained with the slowest draw up speed.

In figure 3.22 SEM images depict the results. In comparison to the samples prepared with spin coating which were discussed before, more material is deposited on the pattern with dip coating. In the images (a) and (b), there are preferably standing arrays of GNR on the patterned substrate after PS has been ashed with oxygen plasma. This can be seen in more detail in the SEM image with higher magnification (b). The attractive force in between the hydrophilic GNR is higher than the attraction to the substrate. Thus, they arrange in such a way that they exhibit the smallest possible area towards the substrate and arrange vertically. The slow deposition technique yields in the most stable state. On the ashed PS film (image (c)), the same trend is observed. The system tries to minimize the interface with the substrate and forms GNR islands instead of a homogeneous coverage of the whole substrate. In contrast to the islands in the patterned substrate, the GNR assemble more often in a horizontal manner on the PS film, which might be explained with a lower concentration.

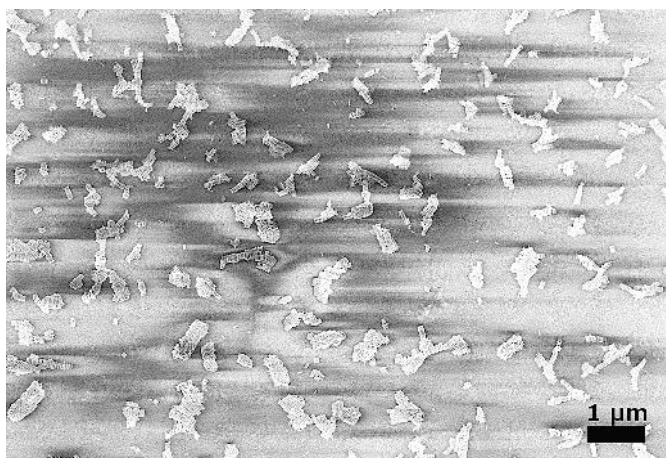
Nevertheless, the concentration of the GNR solution was still too low for larger areas of ordered rods. The technique is not feasible since at least twice the volume of GNR solution would be needed for a film preparation. For a standard fabrication method the volume of 72 mL GNR standard solution is too high. Unfortunately, as the higher concentrated solutions are not stable, storing of an already used GNR solution is not feasible.



(a)



(b)



(c)

FIGURE 3.22: SEM images of GNR in aqueous solution dip coated on a patterned substrate (a) and (b) and on a thin PS film (c).

**Langmuir-Blodgett** The film preparation with Langmuir-Blodgett technique should in theory lead to well ordered films. It is based on the hydrophilic-hydrophobic interaction of material and aqueous sub phase. The method from Lin et al. with GNR in chloroform was adopted [72]. After compression and subsequent transfer to the hydrophobic substrate, a representative SEM image of the product is shown in fig. 3.23.

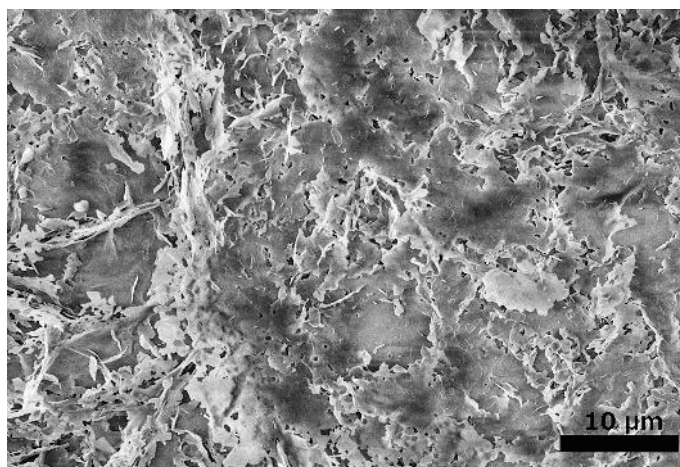


FIGURE 3.23: SEM image of a sample prepared with Langmuir-Blodgett deposition.

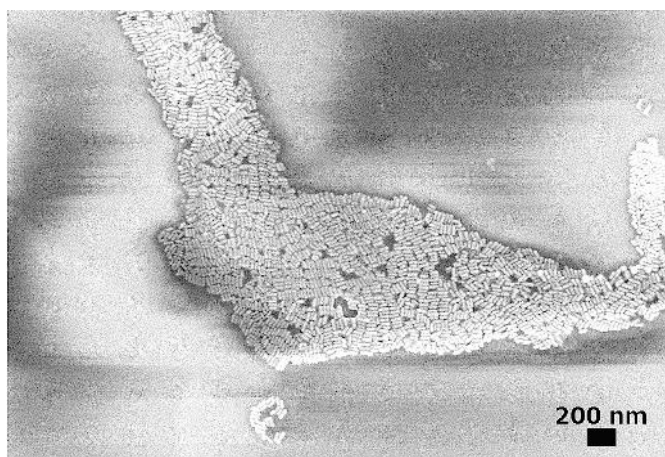
Instead of the expected ordered GNR, the preparation did not work and resulted in few GNR without ordering and with a huge ligand excess (fig 3.23). The SEM image shows only the ligand and no GNR structures can be observed. The higher concentration and further purification did not improve the results, but destabilized the GNR solution completely.

### 3.3.1.2 High Voltage Cell

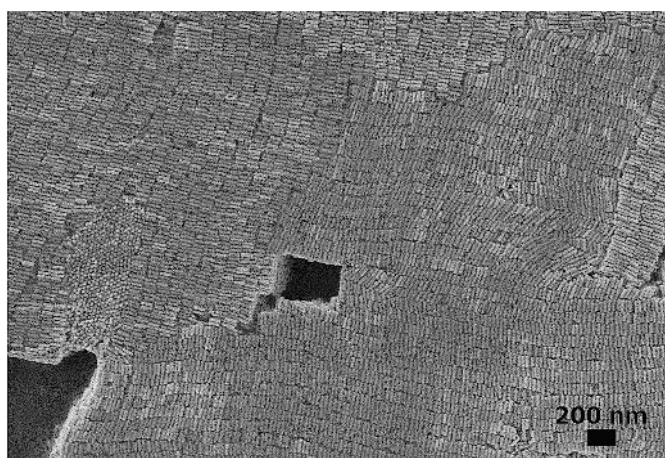
The drying of a GNR solution droplet under 2.0 kV resulted in a skimming of the material. In fig. 3.24 (a) can be seen that the GNR are reduced in size in comparison to the GNR shown before.

The size distribution of the same sample before and after HV treatment is given below.

	Length /nm	Width /nm	AR
After HV	56.79±9.45	18.42±2.29	2.83±0.53
Before HV	81.03±6.94	20.22±2.15	3.74±0.41
%	70	91	76



(a) After 2.0 kV.



(b) Without applied voltage.

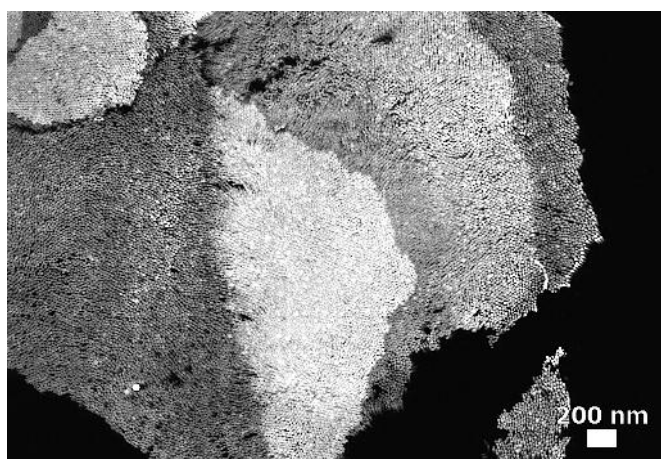
FIGURE 3.24: SEM images of GNR with (a) and without (b) applied voltage of 2.0 kV.

Especially the percentage evaluation clearly shows a decrease in width and length. It sets the size before high voltage (HV) as 100 %. The stronger decrease of the length than of the width (reduction of 30 % and 9%, respectively) indicates that the reaction was three times more pronounced at the tips than on the longitudinal facets (fig. 3.24 (a)). Image (b) shows the results of GNR drying in the cell without applied voltage. The slow evaporation of the solvent over 7 days makes the GNR self-assemble in a well-ordered multilayer structure due to the reduced drying speed. In the SEM image (b) the sides of the horizontally ordered stacks of GNR can be seen. The rectangular gap in the center evolved when the different ordered GNR islands, that crystalized in solution, met. A lower voltage than 2.0 kV did not show any other result than the cell dependent slower drying.

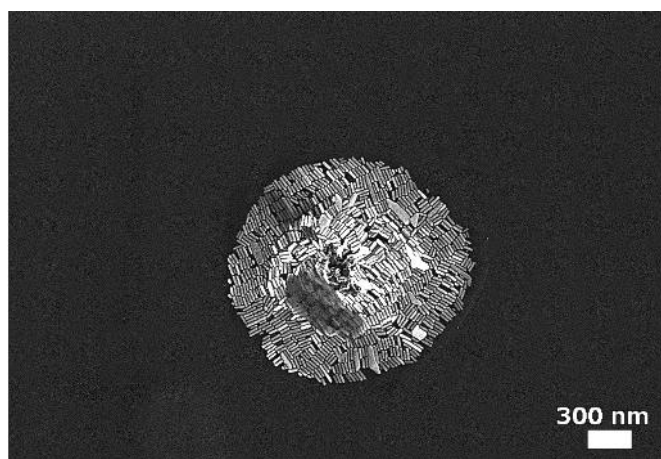
In conclusion, the GNR were not stable towards HV treatment above 1.2 kV. The voltage induced enhanced skimming on the tips, indicating that the GNR are less stable at their transversal facets.

### 3.3.1.3 Influence of the Substrate

In order to understand the substrate-GNR interaction, a large variety of surfaces was investigated by means of droplet evaporation.



(a) On glassy carbon.



(b) On an amorphous C film.

FIGURE 3.25: SEM images of GNR drop casted on different substrates.

Fig. 3.25 shows SEM images of GNR deposited on a polished glassy carbon (GC) disk (a) and an amorphous carbon layer (b), respectively. While the image of the GC substrate (a) depicts an island of highly ordered vertically arranged GNR, from which only the tips are visible in the view from above, the island in image (b) consists of lying GNR only with a short range order.

The result of the exactly same sample preparation on different substrates proves that the choice of substrate has a tremendous influence. The same material in different modifications has an opposing impact on the GNR assembly. On the flat GC surface, the GNR have enough time to assemble in solution and afterwards dry in vertically ordered arrays as described in the droplet evaporation mechanism (2.4.1.1). On the amorphous carbon layer, the droplet is spread out over approximately 4 times the area of the droplet on the GC. This is a consequence of the different wettability. The GNR solution wets the amorphous, rough carbon layer better than the highly hydrophobic GC. Consequently, this improved wettability leads to a larger droplet and thus a lower local GNR concentration. This lower GNR concentration leads to horizontal GNR arrangements. Another effect observed here is that the rough surface of the amorphous carbon film prevents the ordering. Nevertheless, the unpolar surface of both substrates makes the GNR accumulate. This is why GNR islands are formed instead of a statistical distribution of single GNR over the whole substrate.

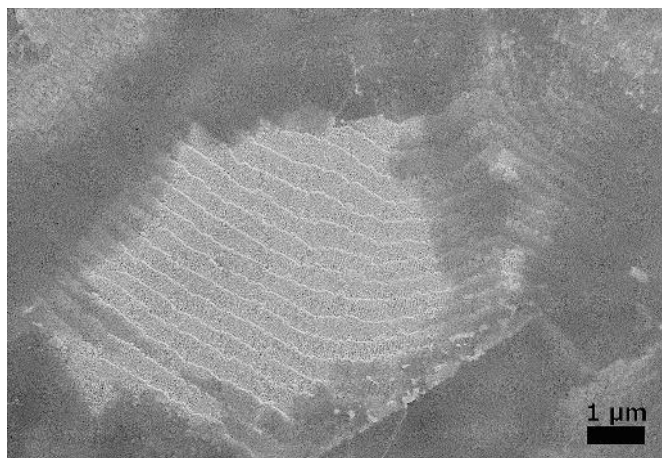
### 3.3.2 Properties and Trends

Overall, the method of droplet evaporation was chosen as the most promising. Highly-ordered arrays of horizontal and vertical GNR over several hundreds of  $\mu\text{m}^2$  were fabricated.

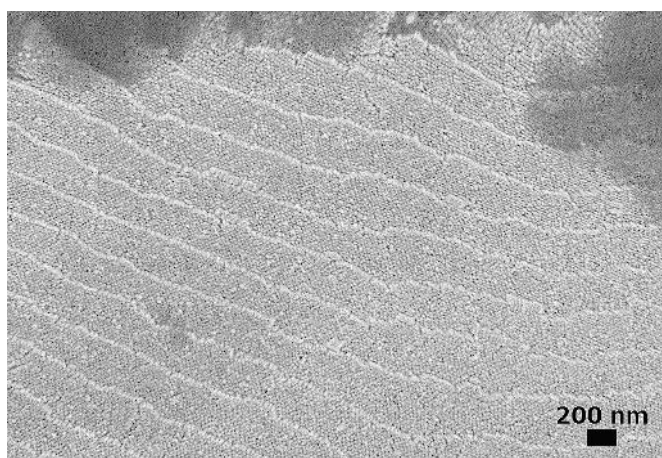
Three different zones on the substrate can be distinguished. A thick coffee ring is formed at the contact line, which is mainly composed of vertically ordered GNR (fig. 3.26 (a) and (b)). In this zone 1, the multilayered structure shows several brighter step-edges, which are energetically more favorable than a flat film. Again, only the heads of vertical GNR structure can be seen, appearing almost as spherical particles, as the longitudinal longitudinal sides are oriented parallel to the SEM optical axis.

At the periphery of the coffee ring, as in fig. 3.26 (c) and (d), the GNR are oriented in a horizontal orientation to the substrate. In these zone 2 areas of horizontally ordered GNR, the concentration is slightly lower. With SEM, the longitudinal sides of the rods are imaged, depicting a beautiful multilayered structure. In addition to the well ordered GNR, also cracks that appear darker in the SEM image, can be seen where different GNR islands meet. These cracks can be explained with substrate-GNR island





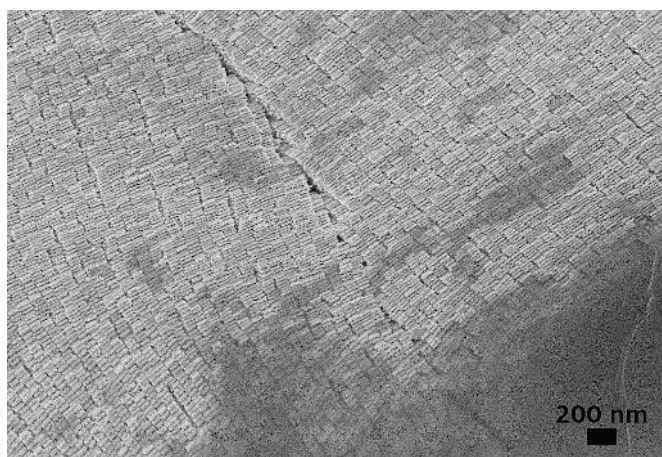
(a) Overview coffee stain.



(b) Detailed image of the coffee stain.



(c) Overview periphery coffee stain.



interaction. When the defect sites in the assembly in solution are filled with free GNR, the film is exposed to mechanical stress. As a consequence, these cracks evolve [128].

Sputtering with a focused ion beam setup and the characterization with SEM afterwards reveals the alignment of the GNR over the whole height of the coffee stain. An SEM image of this is shown in fig. 3.27. The image illustrates the perfect alignment of the layers of side-by-side oriented GNR over the whole height of the coffee ring marked in green. The sample was rotated by 90 degrees, which gives the changed imaging direction. What appears homogeneously grey in the lower part of the SEM image is the substrate along the breaking edge.

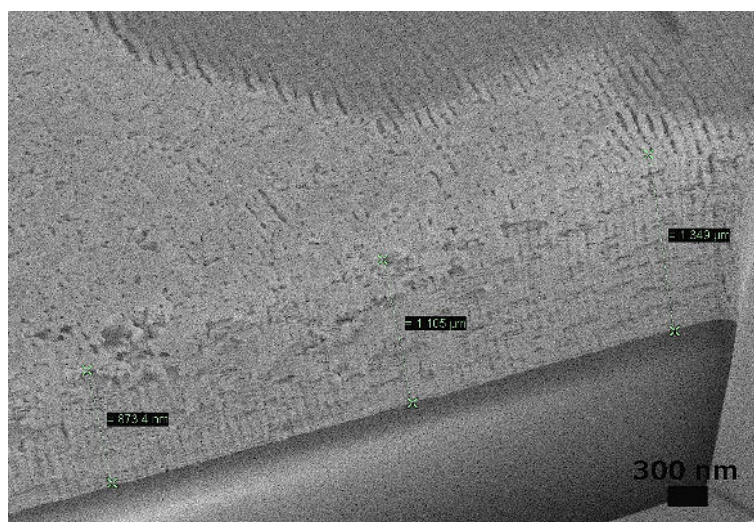


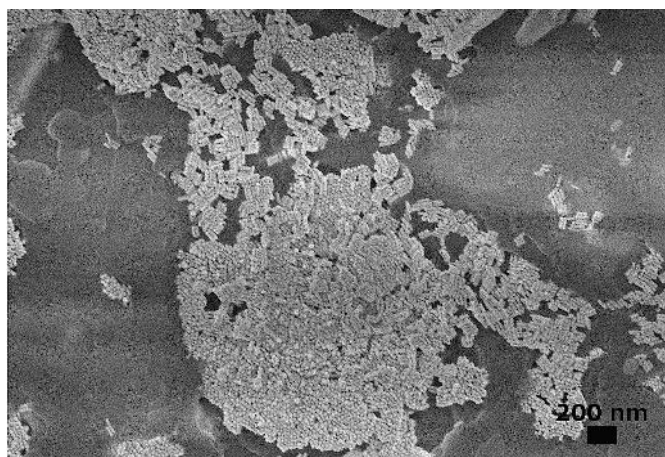
FIGURE 3.27: SEM image of the height of the coffee stain.

The center of the droplet, zone 3, shows the lowest ordering, due to a low GNR concentration. The GNR orient in solution, but since the volume flow direction is outwards, there is not enough material left in the droplet center to form larger arrays. Thus, there are around 2-20 GNR in a side-by-side orientation, but no long-range ordering is observed.

### 3.3.2.1 Drying Speed

Based on the underlying mechanism during the droplet evaporation, the drying speed is a crucial parameter. In fig. 3.28 SEM images of the same GNR solution, where the droplets dried with different speeds are shown. The drying speed is varied between 5  $\mu\text{L}/0.5$  h (fast), 5  $\mu\text{L}/2$  h (medium), and 5  $\mu\text{L}/4$  d (slow).

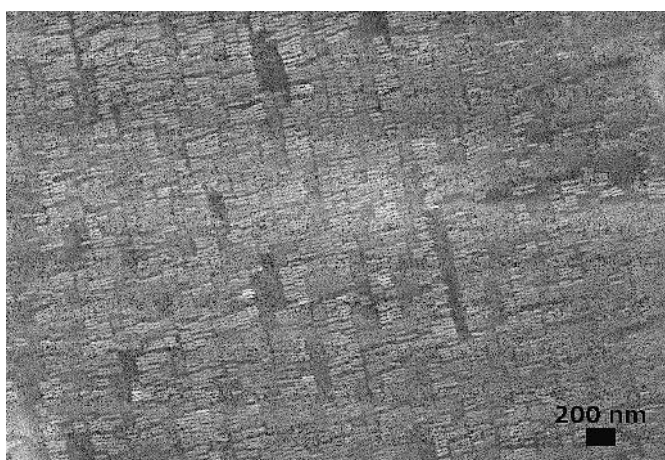
A clear trend can be identified regarding the drying speed. If the solvent is evaporated really fast (a), the GNR are still in the stadium of orienting in solution, when the solvent is evaporated. Thus only small islands of GNR can be seen in the SEM image with no clear orientation, neither vertically nor horizontally. However, the SEM image from a sample prepared with medium drying speed (b), already shows some ribbons or planks of horizontally aligned GNR. Nevertheless, the orienting phase still has not been completed to the most favorable state. This finished orientation can be seen in the coffee ring of the slowly dried sample. The GNR are perfectly ordered (image (c)). In this case, the GNR have arranged in a horizontal manner and have assembled uniformly over large areas.



(a) fast



(b) medium



(c) slow

FIGURE 3.28: SEM images of GNR assemblies prepared by droplet evaporation with different drying speeds.

### 3.3.2.2 Droplet Volume

The droplet volume should basically influence the contact angle and have with different contact lines for different volumes a possible impact on the assembly.

In fig. 3.29 the representative SEM images of the experiment do not show a significant influence of the droplet volume. In all three images large, areas of horizontally ordered GNR islands can be seen. Between the bright islands, darker cracks are visible which will be explained in detail in 3.3.2.4. The reason for the lack of influence of the droplet volume are the small GNR dimensions (nm) compared to the droplet diameter of several  $\text{mm}^2$ . This is a difference of 6 orders of magnitude. As a result, the different contact lines and angles do not effect the GNR solution assembly.

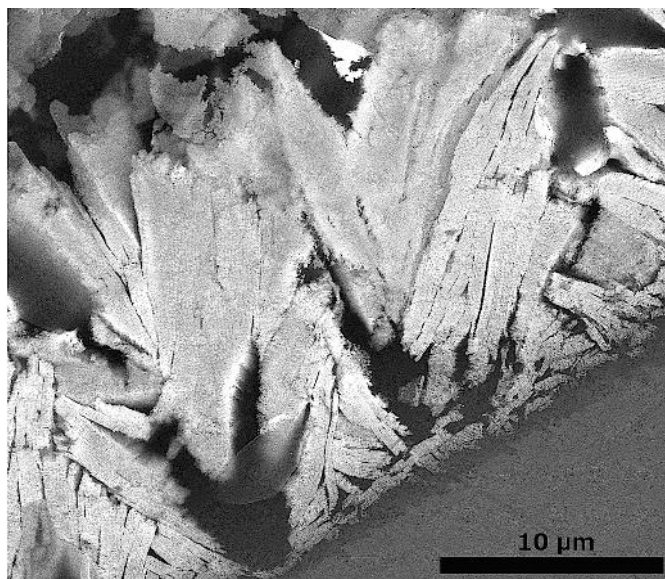
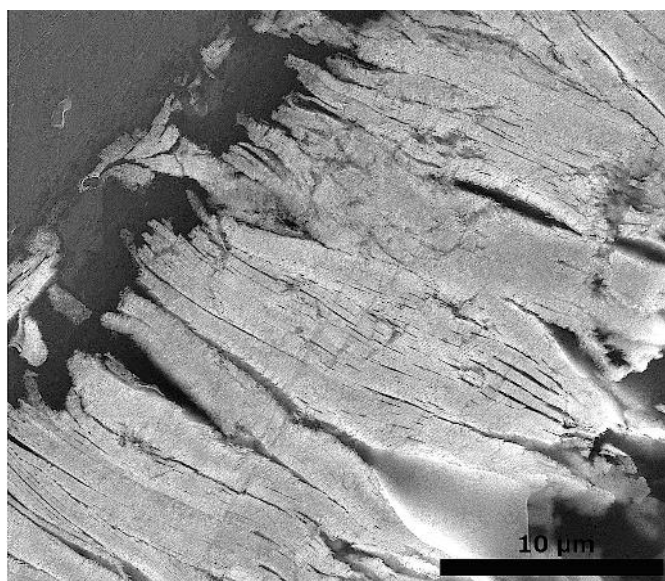
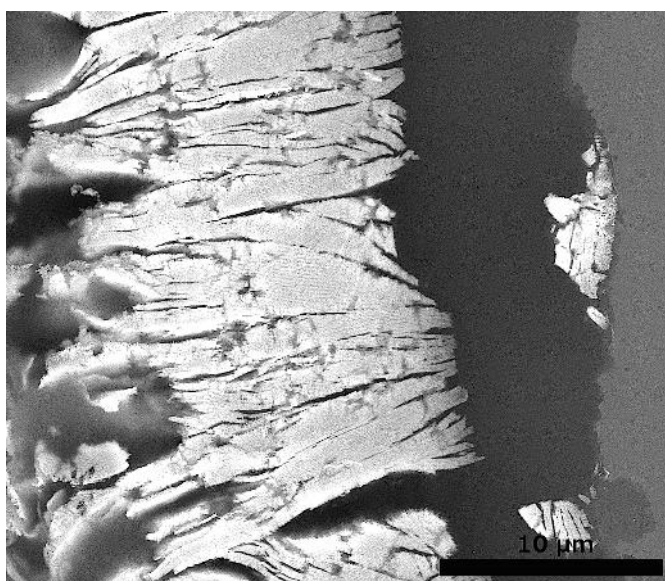
(a) 5  $\mu\text{L}$ (b) 10  $\mu\text{L}$ (c) 15  $\mu\text{L}$ 

FIGURE 3.29: SEM images of GNR assemblies prepared with a different droplet volume.

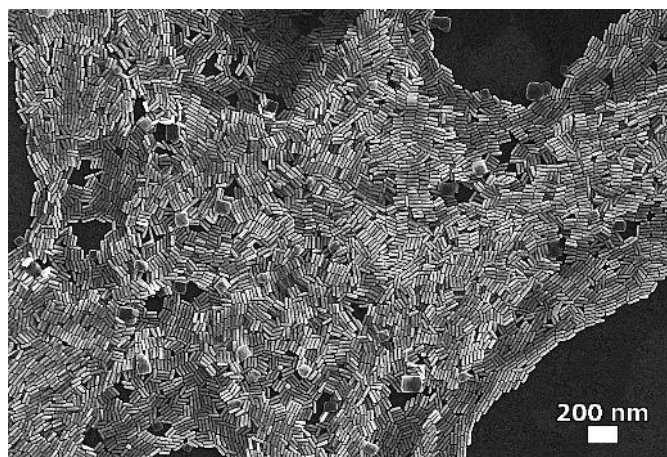
### 3.3.2.3 GNR Concentration and the Role of CTAB

The concentration of the GNR and of the surfactant CTAB are key parameters for the successful assembly of the GNR.

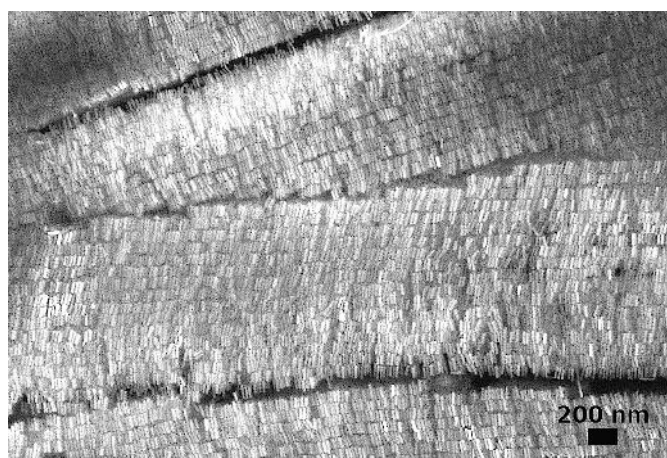
A sufficiently high concentration of GNR and CTAB is a prerequisite. This becomes obvious in the SEM image of structures drop casted with low CTAB and low GNR concentration in fig. 3.30 (a). A low GNR (around 2 nM) and low CTAB concentration prevents the solution assembly and ordering during the drying process, which results in the arbitrarily oriented GNR in image (a). In contrast to this, droplets with a medium CTAB concentration and high GNR (75 nM) concentration dry in well-ordered assemblies. The attractive forces are more pronounced than the repelling ones and lead therefore to the desired results. Fig. 3.30 (b) depicts the already discussed horizontally ordered structures. Interestingly, only one parameter, either CTAB concentration or GNR concentration must be high in order to trigger the GNR assembly. These findings agree with the study of Xie et al. [128]. As can be seen in figure 3.30 (c) the with high CTAB concentration GNR are perfectly ordered, but also covered with an organic film formed by the excessive surfactant, which leads to the blurry image. It aggravates electron microscopy resolution.

As a consequence, a medium CTAB concentration (around 1 mM) and a high GNR concentration (around 75  $\mu$ M) are the chosen parameters applied for the GNR assembly preparation.

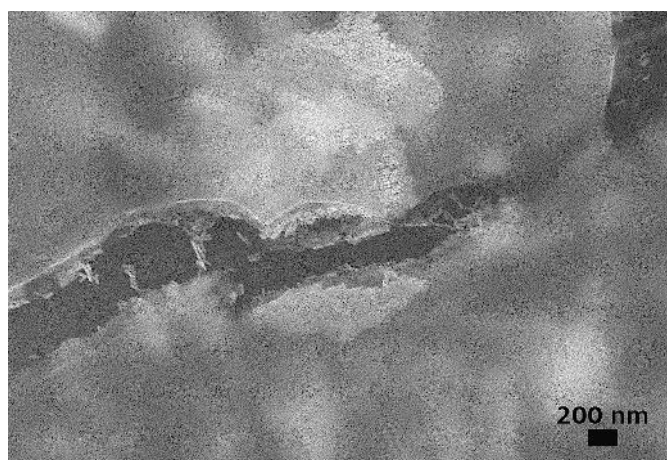




(a) Low CTAB, low GNR concentration.



(b) Medium CTAB, high GNR concentration.



(c) High CTAB, low GNR concentration.

FIGURE 3.30: SEM images of GNR assemblies prepared with different CTAB and GNR concentrations.



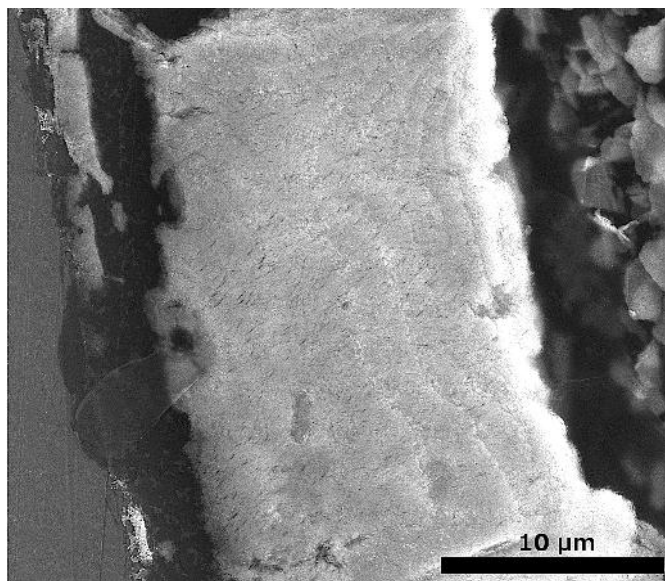
### 3.3.2.4 Horizontal vs. Vertical Assemblies and Resulting Cracks

GNR assemble in a vertical manner at regions with higher local GNR concentration e. g. at the center of the coffee ring. Nevertheless, at samples with lower CTAB concentration, for example after the removal of excessive CTAB, the GNR tend to form horizontal arrays. The reason for this behavior might be the reduced ionic strength and consequently the reduced electrostatic potential, which is directly related to the CTAB concentration [128].

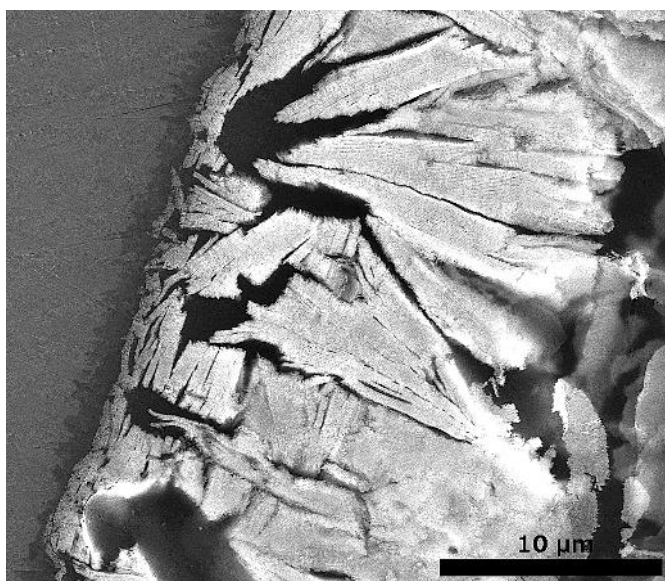
The energetic difference between end-to-end and side-to-side arrangements is reduced for lower CTAB concentrations. The GNR assemble horizontally, since in this structure the amount of end-to-end configurations is increased.

Peng et al. explained the evolving cracks at lower CTAB concentration with the reduced electrostatic repulsion and thus, the GNR being pulled closer together due to the van-der-Waals force [100]. This explanation seems partially valid for this work although, in contrast to the results of Peng and coworkers, with a lower CTAB concentration, preferably horizontal arrangements are observed. However, which agrees with the Xiong group, more cracks are found for assemblies with lower CTAB concentration. In general, there are more cracks in horizontal assemblies (with lower CTAB concentration) (b) than in vertical ones (a), as can be seen in fig. 3.31. For the purpose of the long-range orientation the SEM overview images are shown, with a size scale so that the whole coffee ring can be seen. In the vertical assembly in image (a) only the tips are visible in the SEM image, which stand tightly packed, leaving no free substrate in between. In contrast to this, the darker substrate can be seen in the SEM image of a horizontal arrangement between the islands in image (b).

When the assemblies that were formed in solution hit the substrate, the mechanical stress induced by this is the most relevant parameter. This mechanical stress for vertical arrangements is probably lower and, what might be even more important, due to in increased GNR-GNR interaction area, the vertical arrangements are more stable than the horizontal ones.



(a) Vertical assembly.

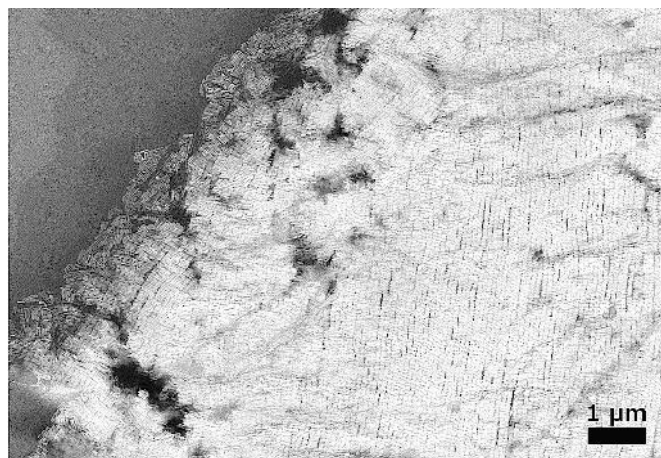


(b) Horizontal assembly.

FIGURE 3.31: SEM images of vertical and horizontal GNR assemblies.

### 3.3.2.5 Upside-Down-Drying

The sample preparation developed to simulate the drying conditions of droplets on leaflets resulted in GNR droplets with a smaller diameter. The corresponding SEM images can be seen in fig. 3.32. The coffee ring in image (a) is composed of densely packed horizontally aligned GNR, while in the image of the center of the droplet (b) depicts ordered islands, disrupted by free substrate areas.



(a) Coffee stain.



(b) Center of the droplet.

FIGURE 3.32: SEM images of a sample dried upside-down.

The material flow outwards is still noticeable. Thus, more material is deposited on the rim of the droplet. Nevertheless, a second nucleation site evolves in the center of the droplet, yielding ordered GNR, too. This gravitationally favored site improves the overall ordering, although the coffee ring effect cannot be completely suppressed.

However, this setup requires larger substrates, so that the droplet can be properly deposited. Otherwise, the sample cannot be turned upside-down, without destroying the droplet.

### 3.3.2.6 GNR AR and Monodispersity

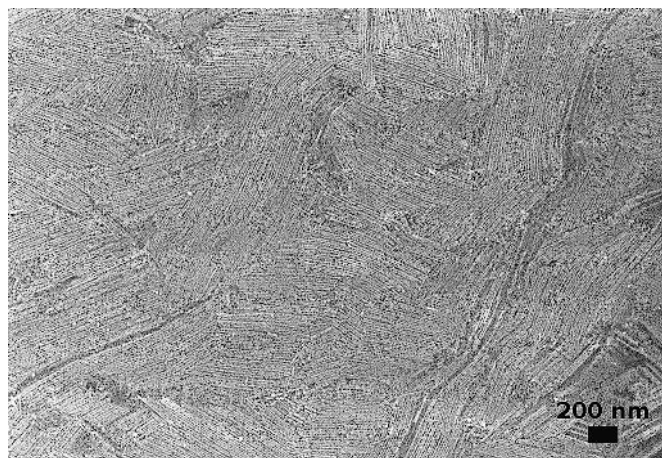
Several AR were investigated regarding their ability to self-assemble into ordered arrays during the droplet evaporation. In general, ordered arrays of GNR could be obtained for

all investigated AR as long as the sample had a narrow size distribution. For GNR with an AR between 2.0-4.5, vertical and horizontal arrays were formed depending on the relative GNR and CTAB concentration and on the surface properties of the substrate.

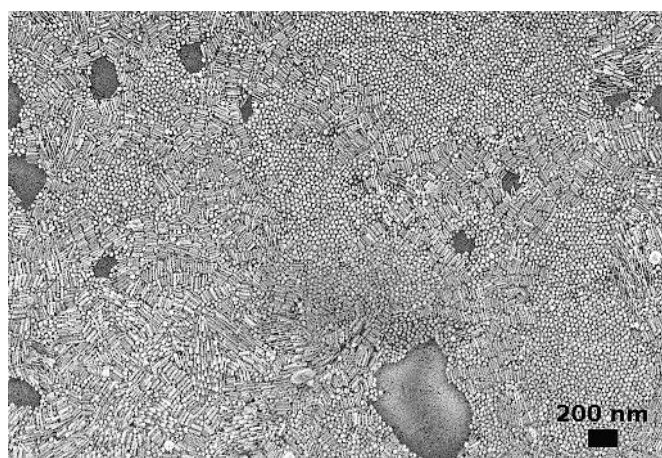
In fig. 3.33 SEM images of the sample with an AR of 6.95 are shown. The ordered arrays of assembled GNR are composed of interdigitate horizontally ordered long GNR (a). As already discussed, the sample showed a bimodal size distribution. Hence, there are also areas of spherical impurities and smaller AR GNR (b). Obviously, the long GNR prefer horizontal instead of vertical ordering. There are no regions of standing arrays on the sample. The long and thin GNR have a different geometry and therefore another center of gravity. Nonetheless, the gravitational force is four orders of magnitude smaller than the electrostatic force, which is why another effect must be more important. What might be the driving force for the horizontal ordering is the lower concentration of the shape, respectively. The actual concentration of long thin GNR is much lower than the overall concentration of a sample with a monodisperse size distribution.

Another important effect can be observed in this sample, too. Most of the shape impurities are segregated from of the monodisperse structures. The above depicted GNR with a length above 150 nm self-assemble separated from the shorter GNR and spherical impurities (image (b)). This result agrees with the findings from Ming et al. who observed that binary mixtures with different GNR diameters self-segregate [87]. Ahmad et al. studied this shape-segregation in detail. Instead of focussing on the importance of depletion interaction during the separation of the rod-rich phases and sphere-rich phases, they discussed DLVO (Derjaguin-Landau-Verwey-Overbeek) theory. The GNR favor a side-by-side assembly in solution and move as a consequence of the pinned contact line outwards. The spherical particles are during this process captured in-between which is why they form a sphere-rich phase although the interaction energy minimum is not that pronounced. Besides finding the interaction potential minimum for side-by-side aligned GNR they also proved, that the thicker GNR form more stable arrays, which is why the smaller AR are more suitable for ordered assemblies. In addition to this, the CTAB bilayer supports the shape segregation. Due to the different curvature of the spheres and rods, the surfactant interpenetrates more effectively from sphere to sphere and from rod to rod, respectively [1].

In addition to what was discussed above, the rodlike particles are polydisperse, with



(a) Ordered GNR.



(b) Impurities of the sample.

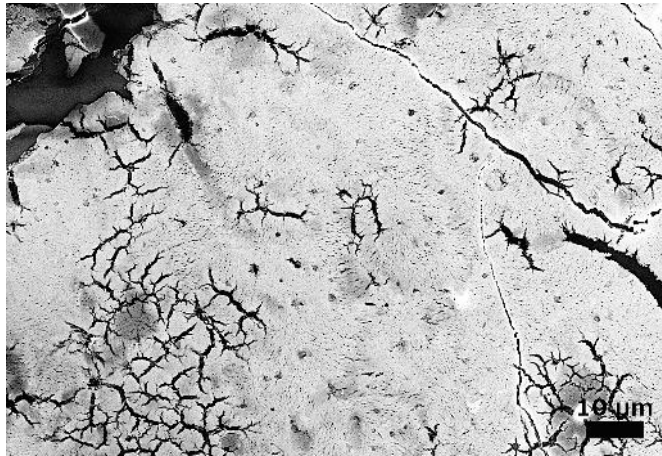
FIGURE 3.33: SEM images of GNR arrangements of a sample with a bimodal size distribution.

a length varying from 100 to 200 nm. The influence of the rod polydispersity was theoretically calculated by Lang. He found, that polydispersity drastically changes the depletion potential for the interaction of rods and spheres. The potential for a standard deviation above 25 % is less steep and has a smaller range [71]. Also in regard to samples containing only rod shaped particles, the narrow size distribution is essential for a large area ordering of the GNR, which is confirmed in the images in fig. 3.33.

### 3.3.2.7 Mechanical Cleavage

The GNR assemblies could be transferred with adhesive carbon tape, usually used for SEM. Based on the graphene fabrication by mechanical cleavage from Novoselov et al.

[96] this method was employed in order to see how strong the GNR assembly-substrate interaction is.



(a) Overview.



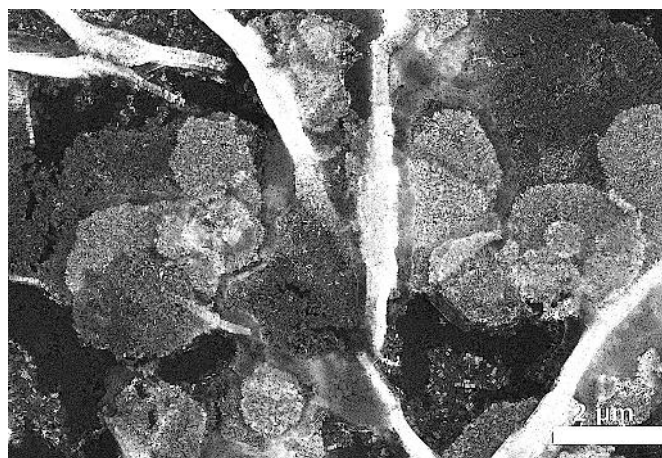
(b) Detailed image.

FIGURE 3.34: SEM images of GNR assemblies transferred by mechanical cleavage.

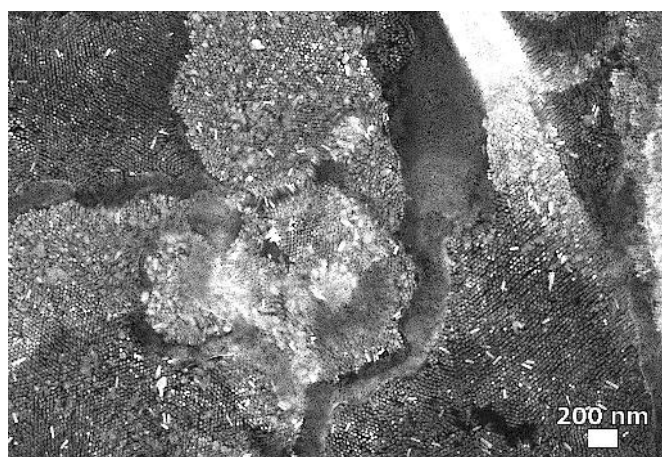
It was impressively demonstrated that the GNR-GNR interaction due to adhesive forces in-between the GNR is much stronger than the GNR-substrate interaction as the assembly could be almost completely be transferred with the mechanical cleavage technique, instead of the original idea of removing only a few layers. In the overview SEM image of the transferred assembly in fig. 3.34 (a), besides the tips of the vertically ordered GNR arrays the already discussed cracks can be seen, too. Image (b) shows this perfectly hexagonal superstructure with a higher magnification.

### 3.3.2.8 Influence of Dimercaptosuccinic Acid and NaCl as Additives

The addition of NaCl based on a method published by Peng et al., for the formation of a monolayer of vertically aligned GNR lead to the following results in fig. 3.35 [100].



(a) Overview.

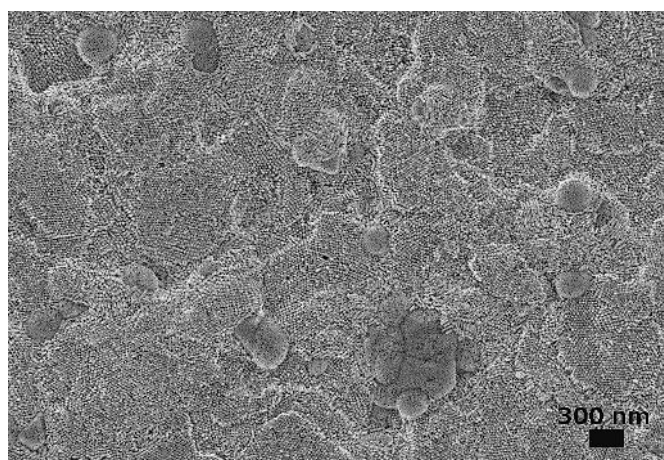


(b) Detailed image.

FIGURE 3.35: SEM images of GNR assemblies fabricated under the addition of NaCl.

The addition of sodium chloride should adjust the ionic strength of the electrolyte and thus influence the electrostatic potential during self-assembly. In the SEM images closer to the center of the coffee stain in fig. 3.35, it can be seen that spherical islands of vertically ordered GNR are formed even closer to the center of the droplet. However, not only a monolayer but in most regions a multilayered structure is obtained. In addition to this, more contamination on the sample is observed, leading to charging effects in SEM.

According to Sreeprasad et al., the addition of DMSA should drastically improve the formation of GNR superstructures [118]. This was justified with a charge neutralization under the formation of a  $\text{CTA}^+$ -DMSA complex. In the conducted experiment the same volume of a GNR solution was drop casted, with an increasing DMSA concentration. SEM images of the results with lowest and highest DMSA concentration are shown in fig. 3.36.



(a) 0.2 mM DMSA.



(b) 3 mM DMSA

FIGURE 3.36: SEM images of GNR assemblies dried with added DMSA.

Instead of DMSA concentration dependent GNR structures, only two different results could be observed. The structures are vertically ordered for low DMSA concentrations (below 2 mM, image (a)) and without ordering and considerable charging effects resulting in white stripes in the SEM image when high DMSA concentrations (image (b)) were utilized. Most probably, the contrasting results are due to the different substrate characteristics. Sreeprasad et al. deposited the solution on TEM grids (carbon coated



copper), while in this work clean glass slides were used. Similar to the addition of NaCl more contamination is detected with SEM, when DMSA was added.

To conclude, the use of additives deteriorates the quality of the SEM images. In addition to this, it does not drastically enhance the ordering compared to the preparation without additives. With regard to the sensitivity of the CLSM measurements, it was decided to use no additional substance.

### **3.4 Fluorescence Intensity Enhancement and Quenching of single SNR on GNP Films**

This sample setup should be discussed here only briefly. It was designed and investigated as a model system and a first approach to the phenomenon of enhanced fluorescence intensity. In the spin coating process of the GNP film production, the amine stabilized GNP were deposited on the substrate. Due to the thiophilicity of gold, the ligand is exchanged easily with the thiol and the bifunctionality of the dithiol results in a cross linked film of GNP (see appendix A.2). The close GNP membrane was on one half of the glass slide removed (see 5.2.3.1), which made the direct assignment whether a fluorescence point was "on gold" or "on glass" possible. This correlation was done on the basis of the transmission (TM) image and the corresponding PL image. In the following, this is exemplarily shown for one sample.

The darker areas in the TM image in fig. 3.37 (b) correspond to the GNP film and the lighter ones to the pure glass substrate. The fluorescence points stem from SNR. The entire sample was covered with a polymer film of a thickness of 11.3 nm in this case. In the PL intensity image (a) it is obvious, that the PL intensity of the SNR on the GNP film is qualitatively lower than on glass.

The quantitative fluorescence intensity (FI) was extracted from the PL images with intensity line profiles of the fluorescence points. The integration under this profile gave the intensity value on gold or glass, respectively. 5 profiles from different directions were taken of each fluorescence point. The process is described in more detail for the GNR substrates. A spectrum was taken on each fluorescence point and the FWHM below 20 nm (in the representative spectrum 16 nm) assured that it was a single SNR (fig. 3.39) [110].

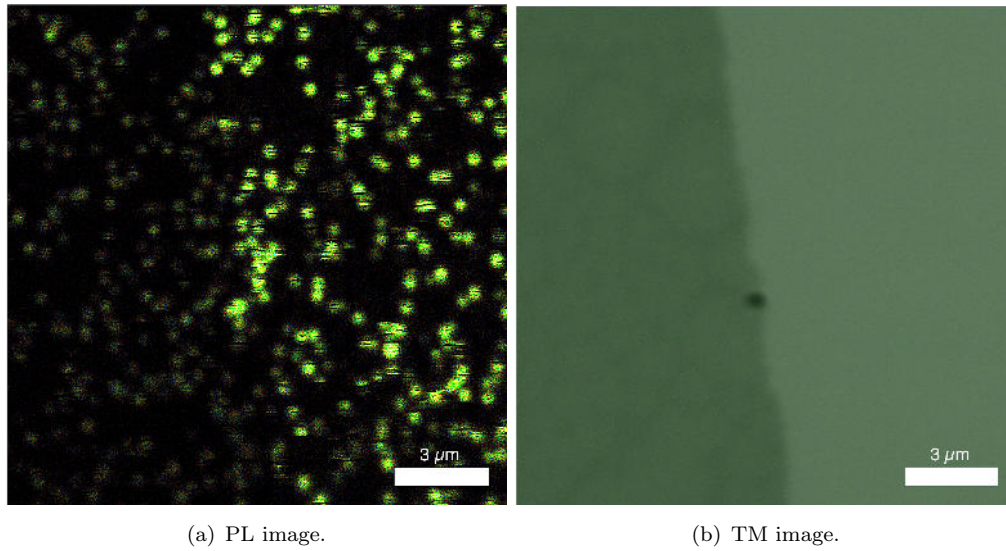


FIGURE 3.37: FI image and the corresponding TM image of a GNP sample with a distance of 11.3 nm.

100 line profiles of single SNR on gold and 100 on glass were taken into account for each distance for this statistical evaluation. In addition to this, 30 blinking curves from SNR on gold and 30 on glass were recorded for each sample and the percentile on and off time was determined. The intensities on gold and on glass were weighted according to the percental on-time. The resulting normalized intensities meaning  $I_{GNP}/I_{glass}$ , before and after blinking correction are plotted in fig 3.38.

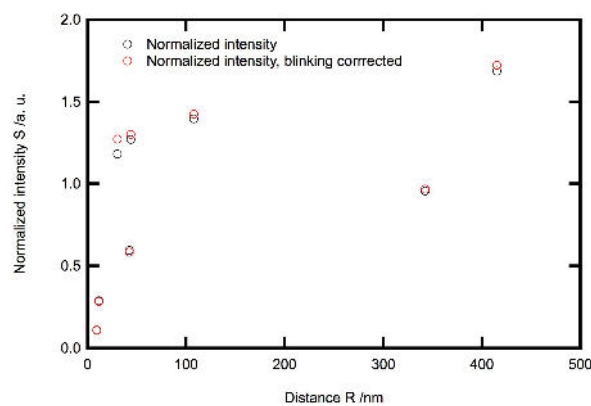


FIGURE 3.38: Graph of the distance dependent normalized FI.

The graph of the normalized intensity shows first of all, that the values with and without blinking correction, do not differ profoundly. Furthermore, no clear trend regarding the FI enhancement and quenching can be recognized, which is why the data points are not fitted to a model, or linked with a line at all.

At a closer look, distance regions for quenching and fluorescence intensity enhancement can be distinguished. If the normalized intensity is below 1, the intensity for SNR on glass is higher than on the GNP film which means that the fluorescence is quenched in the vicinity of the GNP. This is the case for samples with a polymer film thickness of  $R = 9.3$ ,  $11.3$  and  $42.3$  nm, respectively. Whereas, the quenching is much higher (a normalized intensity below 0.5) for the distances around 10 nm, in comparison to the distance of 42.3 nm which showed a normalized intensity of above 0.5. The result, that the fluorescence intensity is quenched around a distance of 10 nm to metallic nanostructures is in good agreement with the literature values [62, 101, 121]. At this gap between SNR and GNP, the non-radiative rate is higher than the radiative rate and ET from the SNR to the GNP occurs. Nonetheless, a quenching at 42.3 nm contradicts with data points near by, which have a completely different normalized intensity.

When the normalized intensity is around 1, both intensities, on GNP and on glass are in the same region, which means neither FI enhancement nor quenching is detected. This was found only for a distance between SNR and GNP film of 342.3 nm.

FI enhancement, a higher FI of SNR on gold than on glass was detected for the distances  $R = 30.3$ ,  $43.7$ ,  $107.8$  and  $415$  nm. No trend is recognizable in these results. Two data points, that only differ for 1.4 nm exhibit quenching and enhancement. In addition to this, the detected FI enhancement of below 2, is rather small compared to the values reported in literature [50, 53, 61, 66, 83, 99]. The distances for which enhancement is observed, are too high for the direct interaction of the surface plasmons of the GNP with the SNR. Although the emission spectrum and the absorption spectrum of the GNP film and the SNR overlap, the experimental setup appears to be problematic. The GNP film shows a surface plasmon resonance around 550 nm, while the SNR are excited with a laser at 488 nm, which is not in the band maximum (fig. 3.39). Thus, a reason why the FI enhancement was relatively low, might be that the surface plasmons of the GNP film were not excited at the band maximum.

Nonetheless, the contradicting results, are mainly a consequence of the sample setup. In the SEM characterization of the GNP film small spots without GNP (see appendix A.2) can be seen, which produce an incorrect assignment of the SNR's environment (glass or GNP film). In addition to this, a change in the film height, when the polymer layer

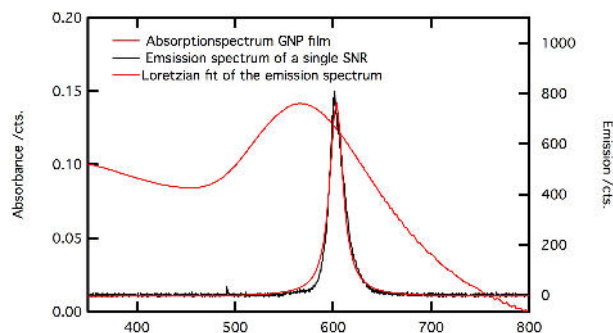


FIGURE 3.39: Emission spectrum of a single SNR and absorption spectrum of the GNP film.

was deposited cannot be neglected. This influences the distance between GNP film and SNR, although being not incorporated in the distance determination by AFM.

However, what was confirmed by two data points and thus many line profiles, is that the fluorescence of single SNR is quenched at a distance of around 10 nm. FI enhancement was found but without a clear trend. This made further interpretation difficult. Nevertheless, the thorough investigation of exciton-plasmon interaction seemed promising.

### 3.5 Sample Setup for Confocal Laser Scanning Microscopy Measurements on GNR substrates

The gathered conclusions, drawn from the study of ordered GNR assemblies were used to design the substrate for the CLSM measurements. The setup, how the measurement could be performed, was apparent. Firstly, the optical measurements of the single SNR at a defined distance to the ordered GNR had to be done. For this both the transmission mode and confocal mode of the microscope had to be used. This made the identification of the GNR islands and the later PL detection possible.

Afterwards, the CLSM measurements had to be correlated with SEM. The simple correlation of TM and PL image was not sufficient as the orientation of the GNR is essential for the interpretation. Unfortunately, spectra from single SNR could not be taken because of the decreased detector sensitivity and the huge scattering of the GNR in comparison to the one of GNP films. The CLSM measurements had to be performed before EM characterization, as the electron beam quenches the SNR fluorescence.

From these prerequisites, requirements for the sample could be deduced:

- Optical transparency - for the transition mode
- Sufficient conductivity for SEM, but still not quenching of the PL in the CLSM
- Variable distance between GNR and SNR
- Suitability for spin coating of single SNR
- Flatness - for the droplet evaporation method

Sadly, the spacer between SNR and GNR could not be sputtered. The roughness and fluctuating height of the GNR arrays (see fig. 3.27) made it impossible to deposit a homogeneous and close film for thicknesses below 10 nm. Secondly, no PL intensity image of good quality could be taken with and without GNR in the same frame with the same focus, if the SNR were deposited above the varying GNR arrays. The height differs in the size regime of 1-2  $\mu\text{m}$ . The height was determined from the coffee ring cross section obtained by focussed ion beam sputtering (see fig. 3.27).

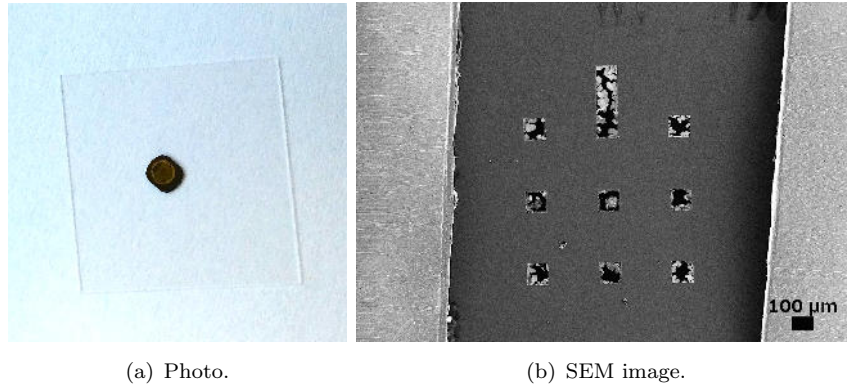


FIGURE 3.40: Photography and SEM image of a prepared SiN substrates.

Finally, after careful tests and research, a substrate was chosen. The substrate that fulfilled all requirements were SiN membranes purchased from Plano GmbH. These membranes could be ordered in different thicknesses. The composition of 8 plus one windows made the correlation possible. The SNR and GNR were deposited from different sides of the sample. In fig. 3.40 (a) an image of the small substrate on a glass slide with the bronze-colored GNR coffee ring is shown. Figure 3.40 (b) depicts an SEM image of the 8 quadratic plus one rectangular meshes, where the GNR islands on the back side are already visible in the overview image.

### 3.6 Fluorescence Properties of Single SNR on Ordered GNR

The investigation of the fluorescence properties of single SNR in the vicinity of ordered GNR is the centerpiece of this work. In total, 95 samples were investigated with fluorescence techniques. It is noteworthy, that even with the most thorough sample preparation, some of the membranes cracked before or during nanorod deposition. This fact abrogated the spatial separation of GNR and SNR and led to non-utilizable results. This is one of the main reasons why most of the data points, especially for the photoluminescence intensity determination were extracted from 7 samples. The following subsections focus mainly on the valuable data obtained from the measurements. Nevertheless, on behalf of reliable scientific practice, possible drawbacks of the picture are discussed.

#### 3.6.1 Photoluminescence Intensity

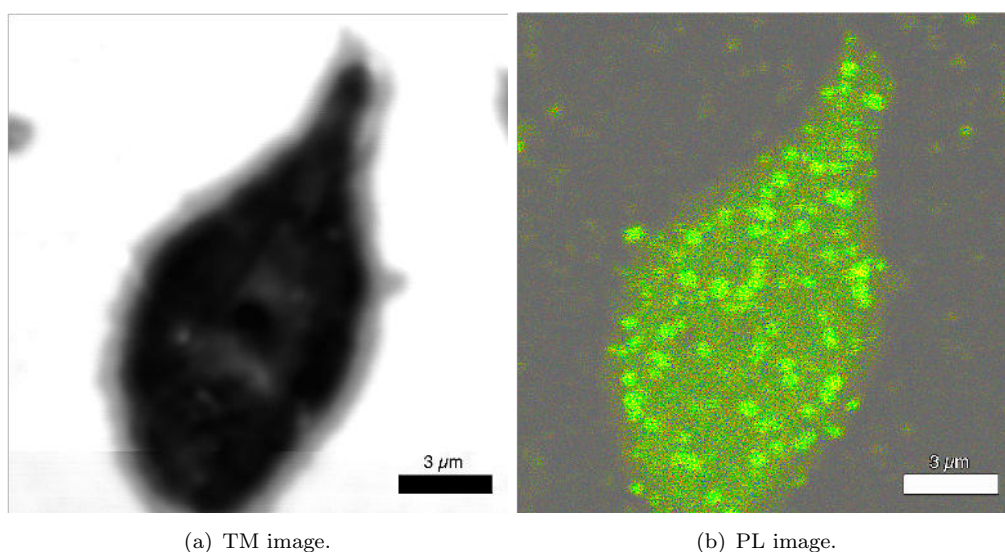


FIGURE 3.41: TM and PL Images of the same sample frame of a 50 nm membrane.

In the vicinity of the GNR, a distance dependent variation of the photoluminescence intensity was expected and could also be observed qualitatively during the measurements. Consequently, for a quantitative description of the results, the normalized intensity of the single SNR was determined. Only those fluorescence points originating from single

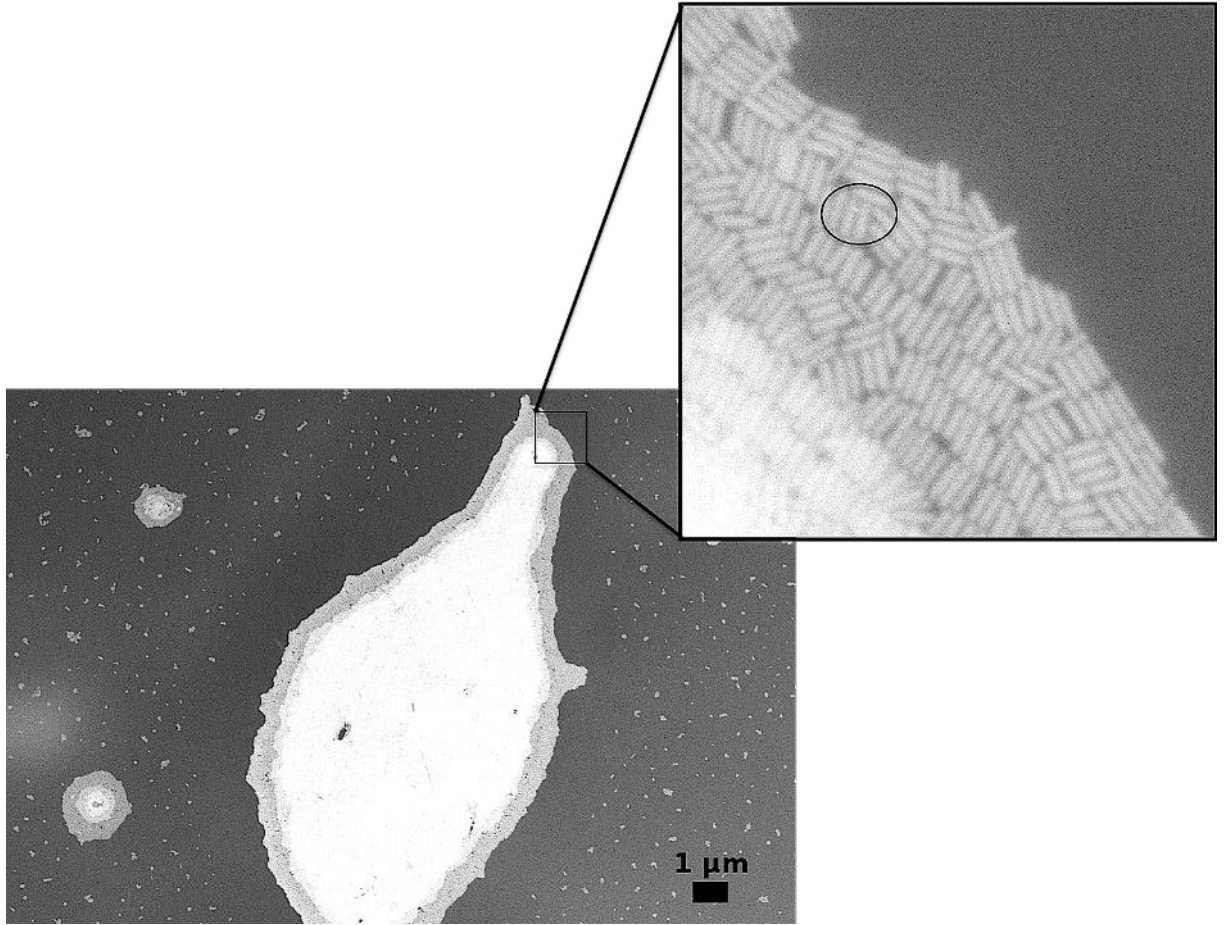


FIGURE 3.42: SEM overview image of a 50 nm membrane, corresponding to the TM and PL images shown before. The inset depicts a single SNR on GNR.

SNR were taken into account. This was ensured by the correlation with SEM. A representative TM image (a) and the corresponding PL intensity image (b) excited with the cw laser diode at 488 nm are shown in fig. 3.41. The transmission image (a) depicts the the shape of the GNR island, which absorbs the incident light partially, darker. The areas, where only a monolayer of GNR was deposited appears grey, while the transmission of thicker GNR assemblies is imaged almost black. The PL intensity image (b) shows the fluorescing SNR in light green.

The characteristic shape of the GNR island from the TM image can be easily recognized in the SEM overview image 3.42. The SEM image with higher magnification, here shown as inset in the overview image, enables the identification of fluorescence points originating from single SNR. The single SNR on ordered GNR is encircled in black.

The identification characteristics were transferred for fluorescence points with the same plasmonic/electromagnetic environment (horizontal or vertical GNR) and a similar PL



intensity. Of each fluorescence point from SNR on GNR, 5 fluorescence intensity line profiles (LP) were taken. In the following this process is exemplarily shown.

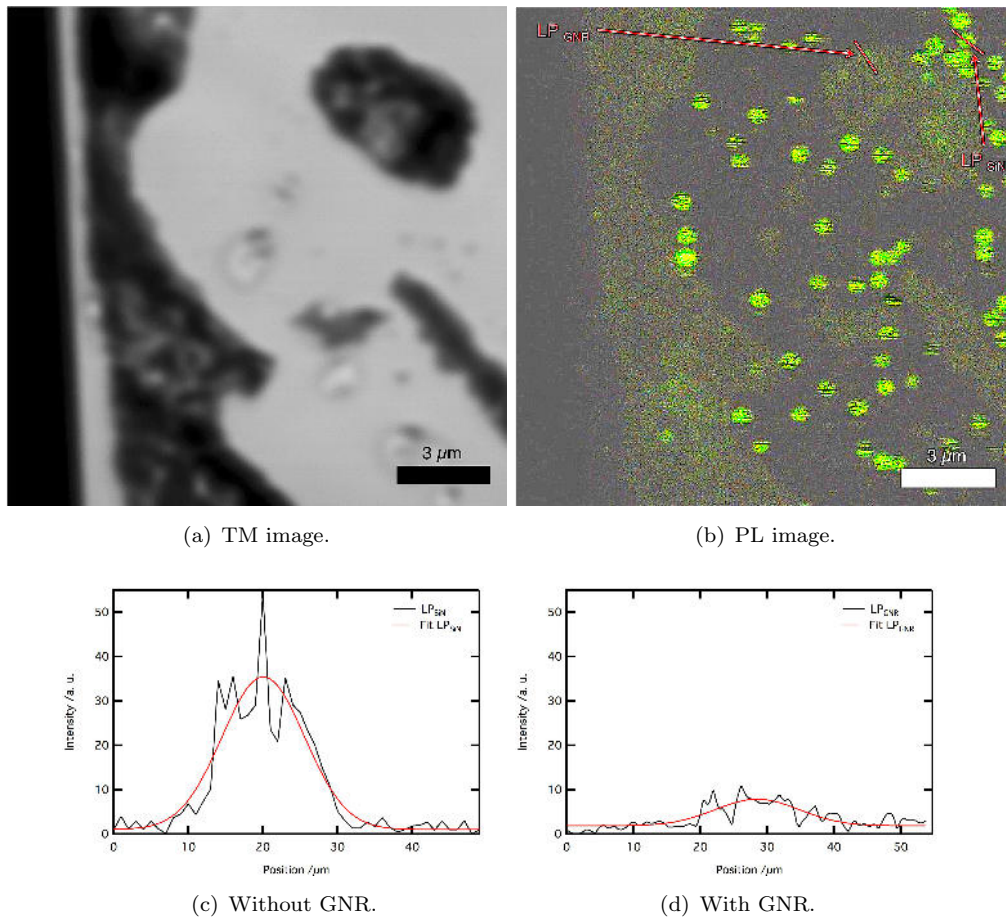


FIGURE 3.43: TM and PL image of the same sample frame of a 5 nm membrane and the extracted LP.

In fig. 3.43 the transmission image (a) and corresponding PL image (b) from a 5 nm membrane are shown. In the PL image the GNR islands are clearly visible, due to insufficient suppression of the GNR scattering by the filter. The line profile on GNR ( $LP_{GNR}$ ) and on SiN ( $LP_{SiN}$ ) are marked in red and shown below in image (c) and (d). In the PL image it is already qualitatively apparent, that the PL intensity is reduced if only 5 nm are in between SNR and GNR. In the line profiles the blinking of the particle obviously influences the fitted curve, which is why the additionally obtained percentage on-time from the blinking curves was not incorporated into the fluorescence intensity. The line profiles in fig. 3.43 were fitted with a gaussian distribution and the areas under the fitted curves were integrated. The values for SNR on GNR were normalized with the average value from SNR on SiN. This operation resulted in the normalized fluorescence intensity. It has to be mentioned that the dimers of SNR-1 (3.1.2) are normalized by



the fluorescence intensity of a semiconductor nanorod dimer on SiN, which is why their resulting normalized FI can be compared to the other data points.

An additional washing step for the GNR before droplet deposition could minimize impurities from the GNR solution. However, the reduced free CTAB during the assembly led mainly to horizontally ordered GNR or sometimes, when the coffee ring was found outside the windows of the substrates, even horizontal GNR islands with reduced ordering. Nonetheless, these effects were less severe than the contamination, which made the evaluation impossible. But consequently, there are less data points for SNR on vertically ordered GNR than on horizontal GNR assemblies.

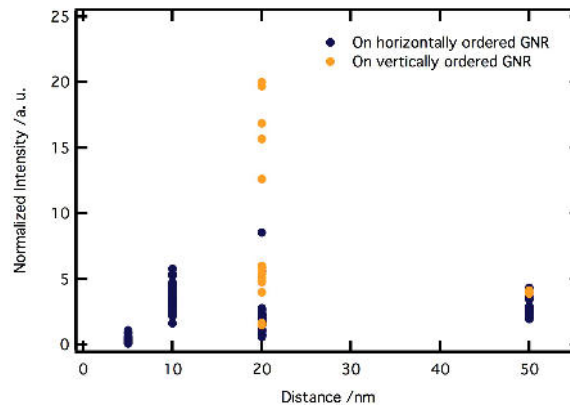


FIGURE 3.44: The normalized PL intensity of SNR on GNR plotted vs. the distance.

In fig. 3.44 the normalized PL intensity was plotted against the distance between SNR and GNR. The FI on horizontal (blue points) and vertical GNR (orange points) was distinguished. Although, the normalized intensity for SNR on vertically ordered GNR at a 20 nm distance is distinctly increased in comparison to the intensity on horizontally arranged GNR, no clear distance-dependent trend can be identified. At a distance of 5 nm the PL is quenched and consequently the normalized intensity is below 1, while for all other distances, values above one, which means an enhanced PL intensity from SNR on GNR can be argued based on this graph.

As explained in 2.2.1, GNR exhibit comparably large scattering cross sections [54]. Consequently, the scattering could not be blocked completely with the utilized longpass filter and dichroic mirrors. This can be seen in the PL intensity images, as the GNR islands are depicted (fig. 3.41 and 3.43). Logically, this scattering is noticeable in the line profiles. Thus, the line profiles taken from SNR on GNR have an increased background.

The intensity of this background varies drastically, depending on the substrate and GNR assembly height, respectively. This off-set distorts the result.

Furthermore, for SiN membranes with a thickness of 10 nm, an intrinsic quenching and reduced lifetime was found, which will be discussed and substantiated with the data in the following subsections. Due to these circumstances, the line profiles from single SNR with and without GNR extracted from the PL intensity images shown in fig. 3.45, deliver biased results.

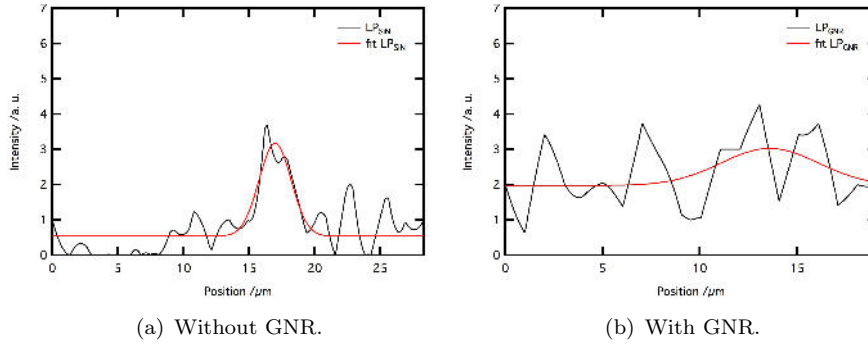


FIGURE 3.45: The corresponding line profiles with and without GNR beneath, on a 10 nm membrane.

The line profile with GNR at a 10 nm distance shows predominantly noise (b). Due to the before mentioned scattering of the GNR, the background is relatively high, compared to the one in the line profile without GNR (a). Subsequently, the area under the fitted curve of  $\text{LP}_{\text{GNR}}$  is 462.78, while the one from  $\text{LP}_{\text{SiN}}$  is only 154.17. This representative example proves, that the normalized intensity in fig. 3.44 for 10 nm is unrealistic.

The photoluminescence points on the 50 nm membranes show in contrast to the ones on 10 nm membranes a distinct intensity, but the scattering from the GNR is considerable. Two exemplary LP from an SNR with GNR and without GNR on a 50 nm membrane are depicted in fig. 3.46.

On that account, the background of the line profiles is subtracted manually and the baseline is set to zero. No adequate "automatic" method could be established for this, as each line profile has a different off-set, according to the GNR height, focus and substrate. Nevertheless, since this treatment is performed for all line profiles, even when the off-set was negligibly small, a comparability is given.

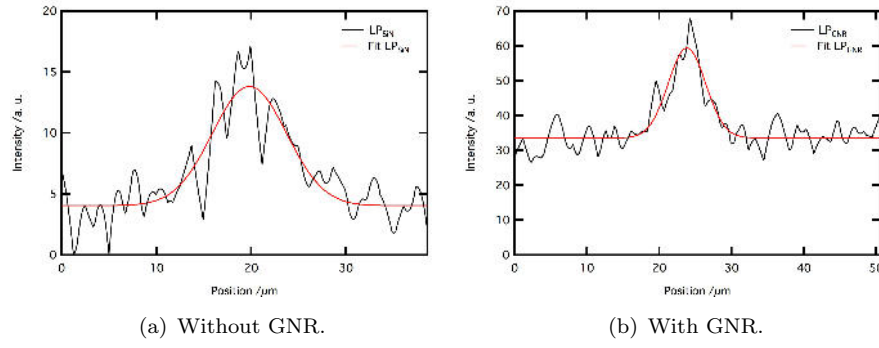


FIGURE 3.46: The corresponding line profiles with and without GNR beneath, on a 50 nm membrane.

Finally, the further evaluation and baseline adjustments leads to the corrected normalized intensity, depicted in fig. 3.47.

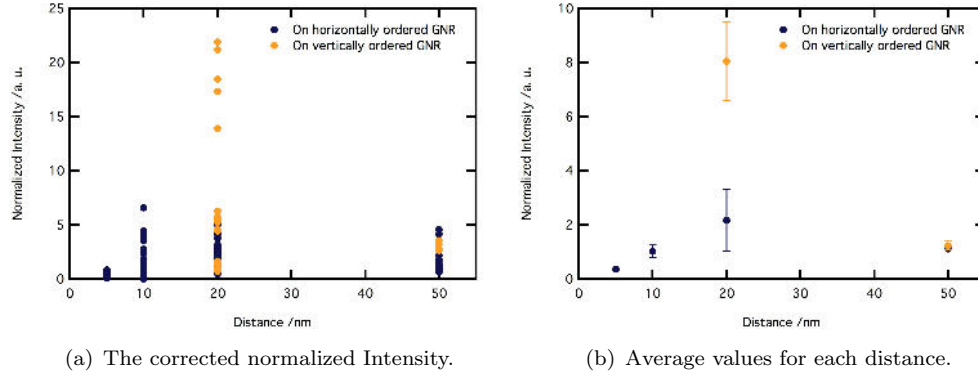


FIGURE 3.47: The plots of the corrected normalized PL intensity.

The graph, including all data points in fig. 3.47 (a) now illustrates the normalized intensity of the SNR in the vicinity of GNR. Just like in the gold nanoparticle film setup, a normalized intensity above one indicates an enhanced photoluminescence intensity of the semiconductor nanorod on GNR in comparison to the PL on silicon nitride without gold. The graph (a) shows a broad variation in data points. This can be explained by different foci (if the sample is not mounted perfectly planar) and most likely more important, different SNR environments. Two SNR, both on vertical GNR arrays can still see another plasmonic environment. The SNR can either be situated directly on the tip, and thus be on the hot spot of the GNR. It can also be between two of those hot spots, which means still a plasmonic interaction but not as pronounced as on the tips. The analogous situation is possible for an SNR on a horizontally arranged GNR. The semiconductor nanorod can be directly in the center, parallel or with an angle to the gold nanorod. Hence, it can be aligned to the transversal or to the longitudinal facets of the

GNR, which has a drastic influence on the radiative rate of the fluorophore. The utilized method, even the correlation with SEM, does not allow a more specific analysis of the SNR-GNR position, owing to the procedure. Nonetheless, the differentiation between horizontally and vertically oriented gold nanorods already opens plenty of room for discussion.

The average normalized intensity in graph (b) now can be analyzed. The error bars give the standard deviation of the mean, including the number of data points. The normalized photoluminescence intensity of SNR on GNR is only 0.36 at a distance of 5 nm. At a 10 nm distance the PL reaches almost exactly one. For 20 nm the normalized intensity on GNR is 2.2 on horizontal assemblies and 8.1 on vertically aligned GNR. For a 50 nm distance the normalized intensity is again around one, for both GNR orientations.

This behavior can be interpreted according to the exciton-plasmon interaction. The PL intensity of SNR at a 5 nm distance to the GNR is smaller compared to the one without GNR, which proves a quenching of the PL by the metal. The non-radiative energy transfer to the metal is more pronounced and so the energy is transferred from SNR to GNR. The value around one at a distance of 10 and 50 nm indicates either no interaction or an increase in radiative and non-radiative rate, so that the intensity remains the same. For a 50 nm distance the first case is most likely, as the exciton-plasmon interaction has a shorter range. It is possible, that for 10 nm distances the radiative rate and non-radiative rate are both simultaneously increased. However, the quenching substrate does not only quench the SNR on the membrane but may also interfere into the SNR-GNR interaction. This creates a more complex situation, which would require a different analysis. It could only be evaluated thoroughly, if the origin of the quenching could unambiguously be determined and if the two processes (SNR-substrate interaction and substrate-GNR interaction) could be decoupled.

For a distance of 20 nm between SNR and GNR, the normalized PL intensity is unambiguously above one. The PL is enhanced by a factor of 2.2 from the GNR whose transversal sides are in line with the SNR. For gold nanorods whose longitudinal side is in line with the fluorophore, the PL is even enhanced by a factor of 8.1. This means that the PL enhancement from vertically ordered GNR is 3.7 times larger than in the vicinity of horizontal assemblies. The most obvious reason for this might be that the LSPR band is more intense than the TSPR band; the longitudinal surface plasmon resonance is 10

times stronger than the transversal [123]. In addition to this, the surface plasmon resonance for vertically ordered GNR is around 600 nm, which matches the emission from the SNR at 600 nm [101]. It is as well broad enough to be excited from the laser excitation wavelength at 488 nm. The resonance of the GNRs surface plasmons boosts the radiative rate from the SNR and thus leads to an increased photoluminescence intensity.

### 3.6.2 Time Traces and Power Law

Many time traces of the SNR on the different SiN substrates with GNR assemblies were recorded. For their evaluation a binning of 50 ms was used. The initial blinking behavior of SNR on the different SiN membranes was studied, too.

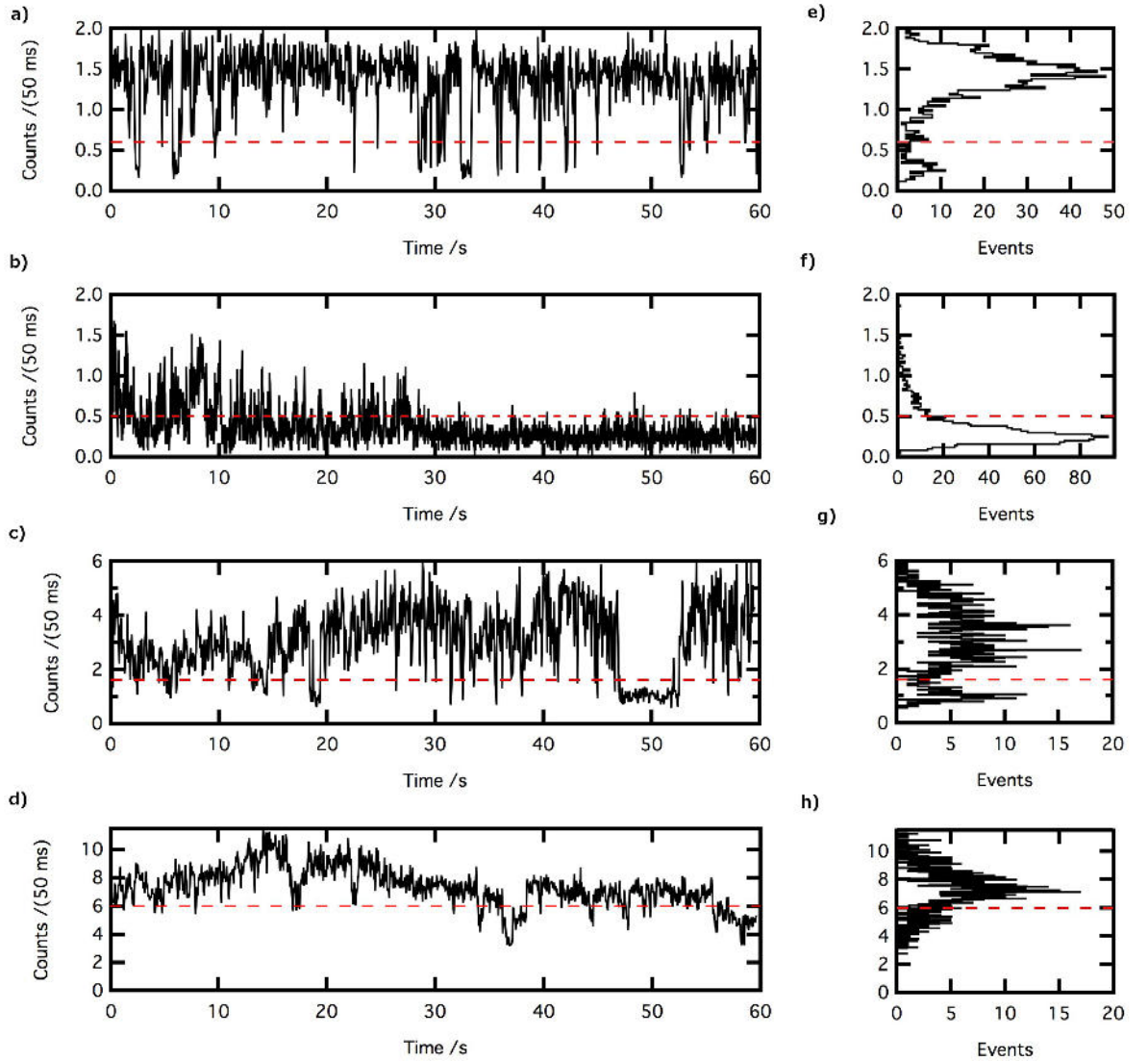


FIGURE 3.48: Time traces of SNR on 5 nm (a), 10 nm (b), 20 nm (c) and 50 nm (d). (e-h) show the corresponding intensity histograms.

In fig. 3.48 representative blinking curves (a-d) and the corresponding intensity histograms (e-h) are depicted, with a binning of 50 ms. Obviously, the blinking behavior on the different membranes is diverse, even without GNR.

The time trace for SNR on the 5 nm SiN membrane (a) shows distinct on- and off-states. The PL intensity is interrupted by dark states which are referred to as trap states. The corresponding models are explained in chapter 2. Averaged over all recorded and evaluable time traces, the SNR on 5 nm SiN membranes are 86 % of the time in the on-state. This percentage is comparable to the QY of the ensemble measurement. SNR on 20 nm and 50 nm membranes exhibit comparable percentage on-times, with average values of 84 % and 85 %, respectively. However, the time traces taken on 50 nm substrates (d), show a relatively large off-set. In principle, an enhanced off-state efficiency was found in thick shell CdSe/CdS dot/rods by Rabouw et al., generated by the so called gray states, which stand for the negative trion state [106]. Since in the presented measurements were performed on thin shell dot/rods, the intrinsic existence of gray states can be excluded. However, as this enhanced off-state intensity was only found for 50 nm membranes and partially for 20 nm SiN membranes, it is more likely, that it is induced by the different focal lengths of the experimental setup.

The blinking behavior of SNR on the used 10 nm SiN membranes (b) is completely different. The shorter on-time intervals are apparent. Qualitatively, the percentage on-time is reduced by more than four times. In the temporal evolution, the SNR spend only 20 % of the time in the on-state. This means, that their PL is intrinsically quenched on these substrates. This finding confirms the PL intensity results.

The probability density of the on- and off-times are plotted on a log-log scale, which was established by Kuno et al. [67]. The data points in fig. 3.49 weighed according to their nearest neighbor are plotted in black and afterwards fitted linearly. The fit is depicted in red.

The average slopes of the linearly fitted on- and off-time probability densities on the four different substrates are shown in the table below.

	5 nm	10 nm	20 nm	50 nm
$m_{on}$	1.22	2.39	1.32	1.34
$m_{off}$	2.35	1.61	2.71	2.53

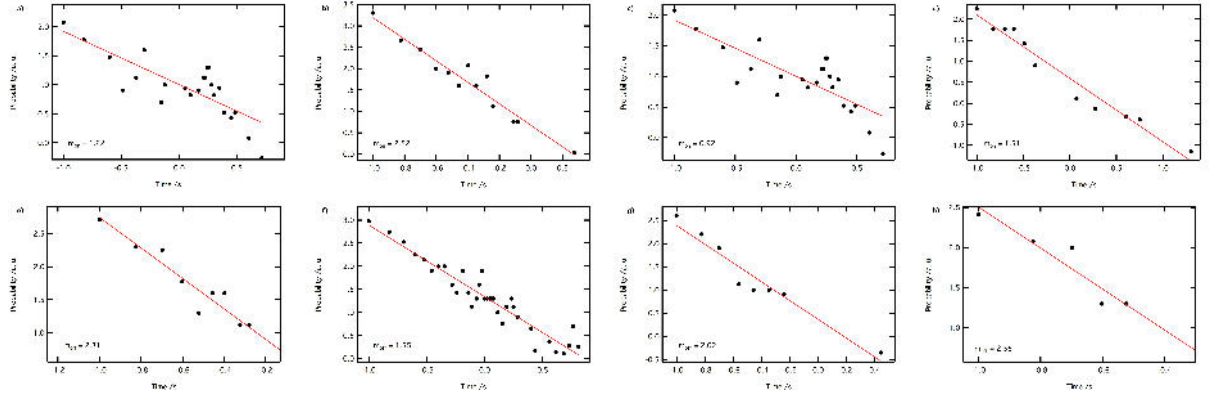


FIGURE 3.49: Probability density of on- (a-d) and off-times (e-h) of the different membrane thicknesses. (a) + (e) 5 nm, (b) + (f) 10 nm, (c) + (g) 20 nm and (d) + (h) 50 nm.

Based on the assumption that the mean on- and off-times depend on the recorded time window  $m_{on}$  and  $m_{off}$  are typically in-between 1 and 2 [18, 32, 40]. Nevertheless, different values have been reported, revealing that the power law might be not as universal as expected [78]. The observation time of 60 s was chosen in order to prevent photooxidation of the CdSe/CdS dot/rods in air. The embedding into a polymer layer was with regard to the SEM characterization not practicable. Although, this approach enabled the full exploration of the PL intensity and lifetime properties, a longer time frame might have improved the probability density statistics.

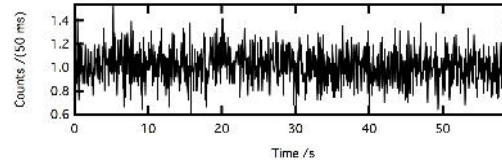


FIGURE 3.50: Representative time trace on GNR with low intensity.

The evaluation of the recorded time traces of SNR on GNR did not lead to insightful results and is therefore not shown in detail in the following. A small laser power was used (0.2 mW) in order to reduce multi-exciton generation. Due to reasons of comparability and reproducibility, this was maintained for all experiments. While the decay curves could be evaluated as the photons are accumulated over the experiment time, the time traces show as mentioned before the temporal evolution of the emission behavior. For most of the point measurements, the intensity variation was not pronounced enough to set a threshold that separates on- from off-state, respectively. This is illustrated by a representative time trace in fig. 3.50. Qualitatively, the time trace shown in fig. 3.50 looks like as if the blinking is reduced. Researchers found this elimination

of blinking and instead the fluctuation between on- and lower intensity gray-states, so that the off-state was avoided, in proximity to gold nanostructures [77]. However, for reliable scientific information, a reproducible procedure has to be established that can be applied on different samples. This was not possible in this work, as the counts for the on-/off-/gray-intensity could not be defined. It changed from membrane thickness to membrane thickness and even from substrate to substrate. Consequently, the inconstant intensity baseline due to different substrate dependent scattering did not allow a distance dependent interpretation.

### 3.6.3 Fluorescence Lifetime

The fluorescence lifetime is a paramount fluorescence property and highly susceptible to the environment of the fluorophor. 61 evaluable decay curves were taken from 12 different samples. Figure 3.51 shows a representative decay for each GNR-SNR distance.

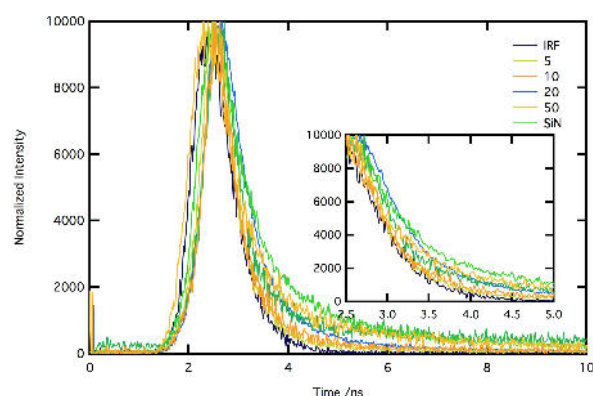


FIGURE 3.51: Graph of the normalized decay curves.

The decay curves are plotted with a logarithmic scale and normalized to 10000. The instrument response function (IRF) as the fastest decay that can be determined, is depicted in the plot as well (dark blue curve). Unsurprisingly, the SNR show the slowest decay on SiN without GNR. The decay of the 50 nm membranes exhibit a similar behavior, whereas the on-set of the curve is shifted to smaller times. Hence, the plasmon-exciton interaction range is below 50 nm, which is again consistent with the PL intensity results.

The SNR with the smallest distance to the GNR, on the 5 nm membranes, decay with a smaller FWHM than the IRF, meaning that the exciton lifetime is shorter than what was measured for the IRF standard, which was here the quenched dye fluorescein. Both,



the SNR at a 10 and 20 nm distance to the GNR decay much faster than without GNR. It can be undoubtedly stated, that for 5, 10 and 20 nm distances of GNR and SNR the surface plasmons of the GNR influence the fluorescence lifetime. Since the evaluation of the decrease in lifetime has to be seen relative to the lifetime without GNR the decays are plotted relative to the decay on SiN.

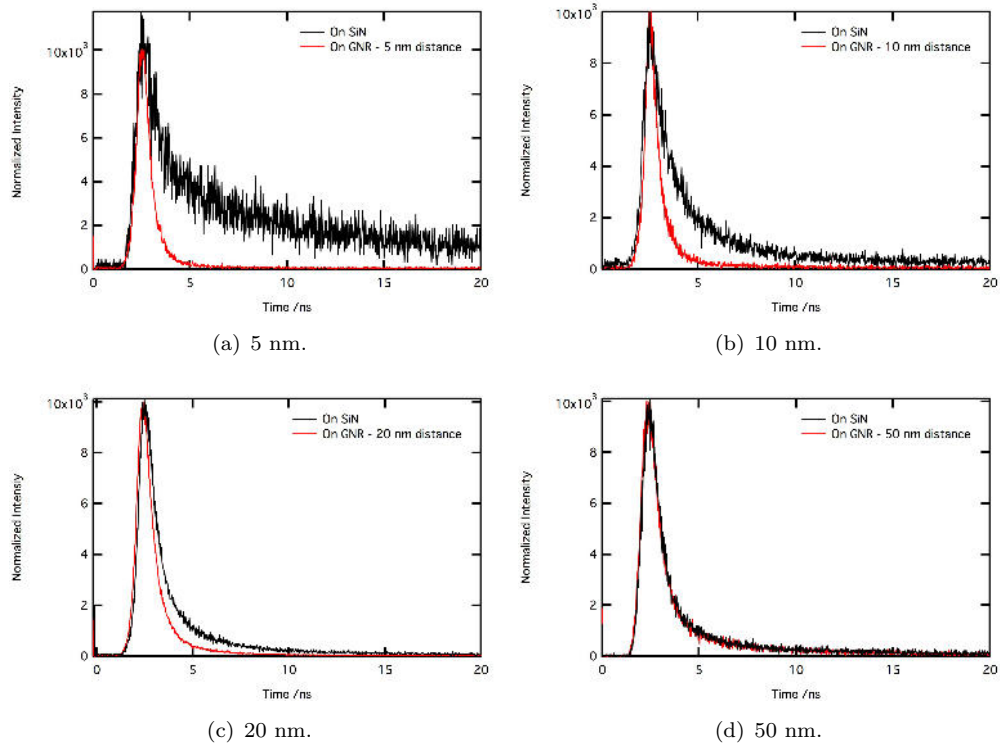


FIGURE 3.52: Graphs of the decays on the different membrane thicknesses, relative to the decay on SiN, respectively.

Figure 3.52 makes change in the decay of SNR in the vicinity of GNR more obvious. For 5, 10 and 20 nm membranes, the decay on GNR is faster than without. For 50 nm distances, no influence of GNR on the decay of SNR could be detected. For the other investigated membrane thicknesses the decay on GNR becomes steeper, antiproportional to their distance to the GNR. The relative decay change is most pronounced for 5 nm membranes and less pronounced for 20 nm membranes. Hence, the plasmon-exciton interaction increases with decreasing distance.

For a quantitative evaluation of the decay curves, the lifetime data has to be extracted. Not all decay curve measurement positions could be correlated with SEM and some lifetime data belonged to more than one SNR. Nevertheless, it could be unambiguously differentiated between SNR on GNR and on SiN with the present transmission images.

The lifetime was obtained with a reconvolution fit. Chosen was the biexponential decay model in the FluoFit software with the lifetime  $\tau$ .

The function used for curve-fitting was:

$$I(t) = \int_{-\infty}^t IRF(t') \sum_{i=1}^n A_i e^{-\frac{t-t'}{\tau_i}} dt' \quad (3.2)$$

The second, shorter lifetime although revealing plasmon-exciton dynamics, was again distorted due to scattering. Thus only the longer lifetime was taken into account. It was averaged over all lifetimes on GNR and on SiN, respectively. Thus, the influence of having determined the lifetime of more than one fluorophor was statistically minimized.

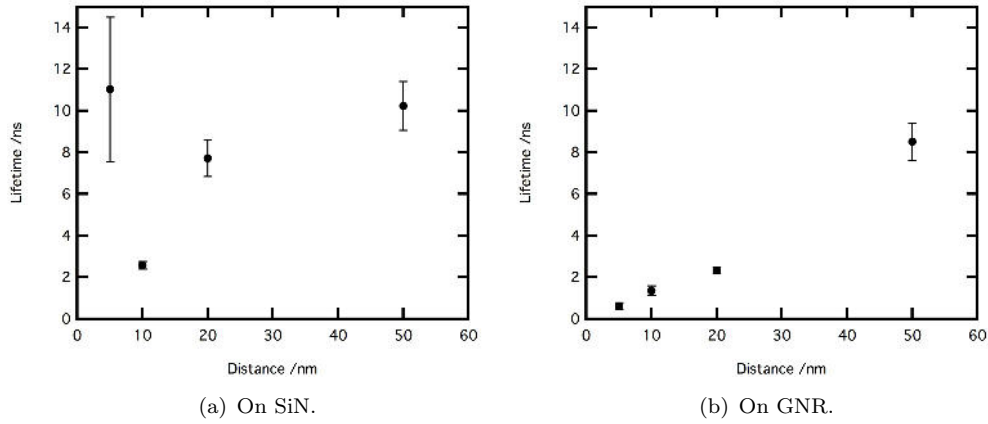


FIGURE 3.53: Graphs of lifetime vs. distance.

In fig. 3.53 plots of the average lifetimes dependent on the membrane thickness are shown, with the corresponding error bars calculated from the standard deviation of the mean. Plot (a) depicts the results on the SiN substrate without GNR and plot (b) the results on GNR. As can be seen, the lifetime of the SNR with a distance of 5 and 20 nm is clearly reduced with respect to the lifetime on SiN. The lifetime of the SNR on membranes with a thickness of 10 nm is extremely low even in the absence of GNR. This confirms that these membranes quench the fluorescence of the SNR intrinsically and is in agreement with the results of FI and blinking. A possible reason for this, is a contamination of the membranes with quenching ions during the preparation of the company. If some batches were produced when quenching ions such as copper were still in the atmosphere of the preparation chamber, these ions could have changed the substrate composition, as the membranes are prepared with high energies. Another unexpected result is that the lifetime is reduced by the GNR even in 50 nm distance.

In order to make the decrease in the lifetime more comparable in between the different distances, the lifetime on GNR is normalized by the lifetime on SiN, which leads to Fig. 3.54.

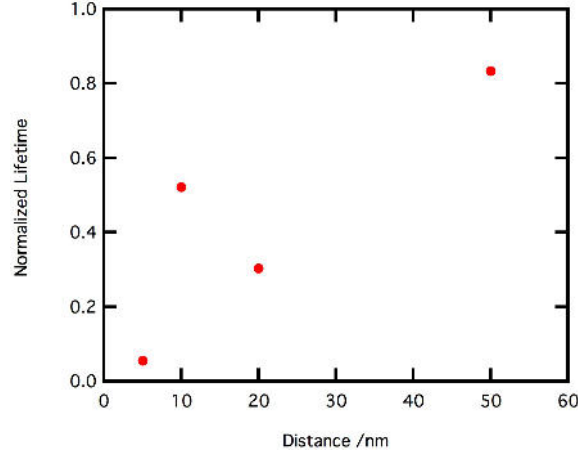


FIGURE 3.54: Graph of the normalized lifetime.

For the interpretation of the results it has to be mentioned that some of the decay curves from the SNR with a 5 nm distance to the GNR could not be evaluated since even with the reconvolution fit, the lifetime was too short for precise determination. Consequently, the decay curves that could be fitted, originated most probable from more than one SNR. For the non-fittable curves the shortest detectable lifetime (450 ps) was used for the evaluation. What can be concluded from fig. 3.54 is that the normalized lifetime for distances of 5 nm between SNR and GNR is only 0.06. The lifetime of SNR at a distance of 20 nm to GNR experiences a reduction to 0.30. Even the intrinsically quenched lifetime of SNR at a 10 nm distance to GNR is shortened by half. Although a slight reduction in lifetime is determined for a 50 nm distance between SNR and GNR this decrease is attributed to the statistical variation of the calculated lifetimes. In addition to this, the scattering of the GNR could not be completely suppressed by the filter. This might have a slight impact on the fitting results.

A more general picture can be obtained by the rates of the different factors. The interaction rate or energy transfer rate  $k_{GNR-SNR}$  can be calculated according to:

$$1/\tau_{GNR} = k_{SiN} + k_{GNR-SNR} \quad (3.3)$$

with  $k_{SiN}$  being the rate on SiN and  $\tau_{SiN(GNR)}$  being the lifetime of the semiconductor nanorods on SiN(GNR) [83]. As the lifetimes have been determined experimentally, the energy transfer rate can be accessed via:

$$k_{GNR-SNR} = 1/\tau_{GNR} - 1/\tau_{SiN} \quad (3.4)$$

The energy transfer rate is plotted vs the distance between gold and semiconductor nanorods in fig. 3.55.

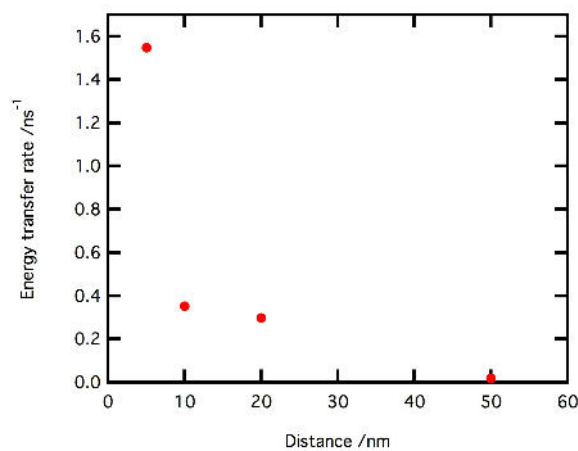


FIGURE 3.55: Graph of the energy transfer rate depending on the distance between GNR and SNR.

The plot illustrates beautifully the increasing interaction between excitons and surface plasmons. The transition is accelerated for a distance of 5 nm to  $1.55 \text{ ns}^{-1}$ , while it is reduced with increasing distance to  $0.30 \text{ ns}^{-1}$  and  $0.35 \text{ ns}^{-1}$  for distances of 10 nm and 20 nm, respectively. For 50 nm distances, the interaction rate is negligible ( $0.02 \text{ ns}^{-1}$ ).

The interpretation of the decrease in lifetime in the proximity of GNR can be substantiated by the fluorescence lifetime imaging microscopy (FLIM) images obtained for the GNR-SNR distances 5, 20 and 50 nm. Unfortunately no such image could be taken from a 10 nm membrane due to the intrinsic quenching of the membrane and the lower intensity and worse focus of the pulsed 405 nm laser diode. Figure 3.56 confirms the hypothesis that the lifetime reduction of SNR on a 50 nm membrane might have other reasons than the interaction with the GNR. The FLIM image (a) corresponds to the TM image (b). The lifetime variation here is only due to the number of SNR. It has to be noticed, that FLIM delivers an image of the average lifetime.

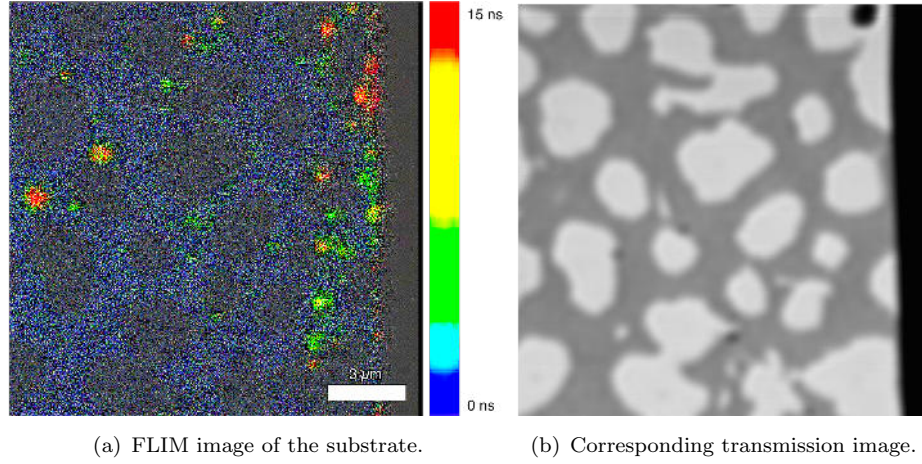


FIGURE 3.56: GNR-SNR distance: 50 nm.

This is why on one hand, no direct lifetime variation can be connected to the proximity of GNR on the lifetime resolved image 3.56 (a). What is on the other hand obvious, is that the scattering of the GNR is detected with FLIM. Thus, the scattering contributes to the lifetime of the GNR, visible in the blue, short-living parts of the image and thus explains its slight distortion. These blue areas can be directly correlated to the darker parts in the transmission image. The longer-living fluorescence points originate from semiconductor nanorod aggregates.

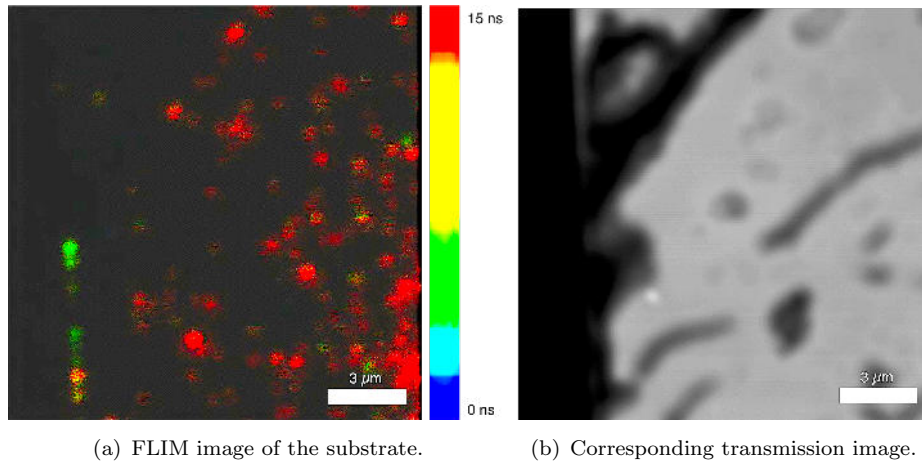


FIGURE 3.57: GNR-SNR distance: 5 nm.

In comparison to this, the FLIM images from 5 nm membranes show a distinct lifetime variation depending on whether the SNR are in the vicinity of GNR. Fig. 3.57 shows a FLIM image (a) and the corresponding frame, imaged in the transmission mode (b). The SNR show a reduced lifetime and intensity close to GNR. Owing to the drastically

reduced FI at a 5 nm distance, an image with aggregates of semiconductor nanorods is chosen, resulting in longer lifetimes relative to fig. 3.56.

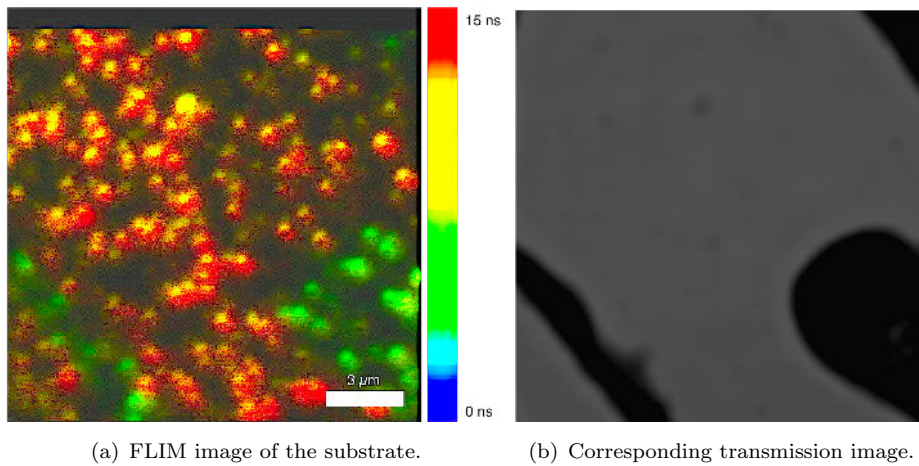


FIGURE 3.58: GNR-SNR distance: 20 nm.

At a 20 nm distance between SNR and GNR, the decrease in lifetime can be beautifully illustrated by the FLIM data in fig. 3.58. The lifetime in image (a) is reduced where SNR are located in the proximity of GNR, verified by the transmission image (b). An important observation here, is that the GNR scattering is more pronounced for 50 nm membranes as can be seen by the detection in the FLIM image. This substantiates the deduction that the normalized FI is slightly biased, which was compensated via the baseline adjustment for all evaluated line profiles.

## Chapter 4

# Conclusion

### 4.1 Semiconductor Dot/Rods

Based on the method developed by Carbone et al., monodisperse thin shell CdSe/CdS dot/rods with a hexagonal wurtzite structure were synthesized [15]. The amount of product with the cubic tetrapod structure was negligibly small. The sample used in the GNP film experiments emitted at 607 nm and the QY was determined to be 41 %. The SNR analyzed within the experiments with the GNR substrates exhibited an even narrower size distribution and emitted around 600 nm or 607 nm with impressively high QY above 80 %. Interestingly, one of the SNR samples had dimerized. In order to understand the driving force behind this change further experiments are necessary.

### 4.2 Gold Nanorods

Two synthesis methods, one developed by the El-Sayed and one by the Murray group were successfully performed [94, 131]. They led to highly monodisperse GNR. A thorough investigation of the different parameters revealed that both methods are strongly dependent on the seed size and seed concentration. In the first method this manifested itself as an irreversible change in GNR dimensions after 41 syntheses. However, with the second method, an even higher monodispersity, larger batch sizes and tunable aspect ratios were achieved, which is why the synthesis by the Murray group was chosen for further experiments. The standard synthesis procedure resulted in perfectly monodisperse

GNR with an AR between 3 and 4. A further study of different synthesis procedures showed that procedures to synthesize GNR with AR above 4.5 or small AR but high GNR dimensions led to broader size distributions. A wide range of parameter variations in the standard synthesis procedure allowed the identification of essential steps and reagents in the complex GNR formation. The variations indicated, that the stirring is unexpectedly irrelevant. The seed generation with a sodium boron hydride concentration above a critical concentration was found to be crucial for the GNR generation. This confirmed again the strong influence of the seeds on the GNR growth. Overall, the results agree with previous reviews, in which the synthesis mechanism was described as complex [74, 75]. The different processes are interconnected, which is why only the regulating screws but no direct proportionality could be found.

A ligand exchange with octadecanethiol allowed the desired transfer of the GNR into organic solvent. The red shift of the LSPR wavelength substantiated the success of the experiment. The influence of the dielectric environment on the GNR optical properties is confirmed by Mie-Gans theory [102].

With the cyanide etching after the ligand exchange with PEGMUA, a powerful tool for testing the completeness of the ligand exchange was established. The ligand exchange with PEGMUA and subsequent testing with oxidative etching showed, that only one tenth of the polymer ligand is needed for a quantitative ligand exchange, if excessive CTAB is extracted with chloroform. The additional step of destabilizing the initial ligand system by extraction made the process most effective. The experiments proved, that three washing steps with PEGMUA and an incubation with PEGMUA for 16 hours before the extraction led to the best results, regarding the complete ligand exchange and minimized amount of applied PEGMUA.

### 4.3 Ordered GNR Assemblies

A plethora of GNR deposition techniques were tested. In contrast to commonly-used film deposition techniques, no ordered arrays over larger areas could be obtained with spin coating, Langmuir-Blodgett technique or dip coating without huge costs of material. However, the drying by droplet evaporation was determined to be an easy to handle and potent technique. Based on the coffee stain effect, areas of several hundreds of square



micrometers of horizontally and vertically GNR arrays were fabricated. For a successful experiment, the ionic strength of the solution has to be above a critical value (either with excessive CTAB or other ionic additives) in order to assure the GNR ordering. The experiments confirmed, that a reduced drying speed and high GNR concentration resulted in assemblies with the highest ordering, while the variation of the droplet volume did have no notable influence on the ordered area. An optimized setup that reduced the drying speed to 3  $\mu\text{L}$ / 5 days was designed and used for the later production. The investigation of various surfaces suggested, that vertically ordered arrays were produced most preferable on unpolar surfaces. Areas of high GNR concentration as well as slowest drying speed led to perfectly vertically ordered GNR.

#### **4.4 Single SNR in the Vicinity of Ordered Gold Nanostructures**

As a first approach towards the investigation of distance dependent fluorescence intensity of SNR in the proximity of gold nanostructures, gold nanoparticle films were studied as a model system. The perfect anisotropy of the gold nanoparticles set the strategic focus on the distance dependent fluorescence quenching and fluorescence enhancement. These GNP films could be deposited over 1  $\text{cm}^2$ , the distance to the SNR could be adjusted with a polymer spacer layer and the reference without GNP was readily accessible. This first setup made the detection of distance dependent FI enhancement and quenching possible. Besides the fluorescence quenching around 10 nm distance, FI enhancement of a factor 2 was detected. Unfortunately, this enhancement did not show a clear trend regarding the distance between SNR and GNP film. Reasons for contradictory results might be an inconstant spacer thickness. During the spin coating process with different polymer concentrations, the GNP film could have been partially torn up yielding in a thicker GNP-SNR distance at these spots. Additionally, defects in the film might have resulted in a varying sample height. In addition to the probably nonuniform GNP-SNR distance, the filter system of this sample setup is improvable. The reflections of the GNP film could also have influenced the results. Besides the mentioned drawbacks of this sample setup, these first measurements paved the way for a distance and conformation dependent setup.

Thereupon, the setup for the distance dependent measurements from single SNR and ordered GNR was carefully chosen. It was successfully realized by a two-sided deposition of ordered gold nanorods and single semiconductor dot/rods, with a thin SiN membrane as a spacer in-between. The optical measurements were correlated with SEM so that the optical properties of one definite fluorescence point could be directly assigned to one single SNR. SNR with 5, 10, 20, and 50 nm distance to ordered GNR were investigated in terms of photoluminescence intensity, blinking behavior and fluorescence lifetime.

The photoluminescence of SNR on membranes with a thickness of 10 nm was intrinsically quenched, even without GNR. This was consistent in all investigated properties. A reduced fluorescence intensity, as well as a reduced lifetime and reduced on/off state ratio extracted from the time traces was found for SNR on 10 nm membranes.

The normalized lifetime was reduced with decreasing SNR-GNR distance, due to stronger plasmon-exciton interaction. Confirming this, no change of the lifetime of SNR with and without GNR at a distance of 50 nm was detected. FLIM images reflected the reduced lifetime on GNR, for all distances except for 50 nm, impressively. The energy transfer rate from semiconductor to metal nanorod was calculated. The rate was significantly enhanced at a 5 nm distance. The energy transfer rate is reduced with increasing SNR-GNR distance.

The normalized photoluminescence intensity confirmed the results from the fluorescence lifetime. Neither enhancement nor quenching of the SNR PL intensity was found for a 50 nm distance of GNR and SNR after scattering effects had been subtracted. This clearly determined the plasmon-exciton interaction to be a phenomenon with a range below 50 nm. For a short distance of 5 nm, the PL of SNR on GNR was drastically reduced, which can be attributed to an energy transfer from the SNR to the GNR. This was confirmed by an enhanced interaction rate between gold and semiconductor nanorods. The situation of SNR on the 10 nm membranes was found to be exceptional, as the membrane as a quenching material is brought in-between plasmonic structure and fluorophore. The normalized PL intensity of around one at a 10 nm distance might indicate an enhanced radiative and non-radiative rate. Anyway, it is understandable that the results of this changed setup of plasmonic structure, quencher and fluorophore in a row, is out of sequence. The energy transfer rate still confirms the trend to be increased with decreasing distance between semiconductor nanorods and gold also at a

distance of 10 nm. At a 20 nm distance between GNR and SNR the PL is enhanced by a factor of 2.2 for horizontally arranged GNR and even by a factor of 8.1 for vertically ordered GNR. This beautifully corresponds to the higher absorbance of the LSPR in comparison to the TSPR. In conclusion, the interaction of the GNR structure with the single SNR at a distance of 20 nm leads to an enhanced radiative rate or a reduced non-radiative rate [28, 101]. The results are in good agreement with the radiating plasmon model [6, 35]. The surface plasmon band of vertically ordered GNR around 600 nm enhances the SNR's radiative rate and the large scattering intensifies the emission in the far-field [76, 101].

Time traces on silicon nitride without GNR could be evaluated. They confirmed the QY determined from the ensemble measurements as well as the observed quenching of the 10 nm membranes in the PL intensity images. For the blinking curves on GNR no uniform on- or off-intensity could be identified due to changing foci and varying substrate scattering.

For any further work with this setup it is worth mentioning, that the large scattering cross section of the GNR although being responsible for the PL enhancement, complicated the interpretation of the results. Although several filters and dichroic mirrors were used, the GNR signal was not completely blocked. Moreover, the sample deposition from both sides on such a small substrate size aggravated the clear separation of semiconductor nanorods and gold nanorods.

Altogether, due to the large number of investigated samples and data points, a statistically relevant picture of the optical properties of single semiconductor nanorods in the vicinity to ordered gold nanorods could be obtained. A distance and conformation dependent fluorescence intensity enhancement of single SNR in the vicinity of aligned GNR could be detected, consistent within the different studied aspects. The strongest effect was observed for SNR at a 20 nm distance to vertically ordered GNR arrays.



## Chapter 5

# Experimental Methods

### 5.1 Chemical Methods

In this section, it is described how the different types of nanorods were synthesized and how ligand exchanges in solution were performed.

#### 5.1.1 Chemicals

In all syntheses and further measurements, only solvents with a declared purity "for analysis" was utilized. For spectroscopic preparations, solvents of spectroscopic purity were applied.

For the SNR, the following chemicals were utilized: Cadmium oxide (99.9 %, Sigma-Aldrich), Sulfur (99.8 %, Sigma-Aldrich), Selenium (99.99 %, Alfa), trioctylphosphine (90 %, Sigma-Aldrich), trioctylphosphine oxide (>98 %, Merck), hexylphosphonic acid (100 %, Alfa), octadecylphosphonic acid (100 %, Alfa).

The GNR syntheses and subsequent experiments were performed with the following chemicals: ascorbic acid (99 %, Sigma-Aldrich), dimercaptosuccinic acid (98 %, Sigma-Aldrich), cetyltrimethylammonium bromide (99 %, Sigma-Aldrich), hydrochloric acid (37 %, Merck), nitric acid (70 %, Merck), octadecanethiol (98 %, Sigma-Aldrich), potassium cyanide (96 %, Sigma-Aldrich), silver nitrate (99 %, Sigma-Aldrich), sodium boron hydride (98 %, Fluka), sodium oleate (97 %, TCI), tetrachloroauric acid trihydrate (99 %, Sigma-Aldrich).

### 5.1.2 Synthesis of Semiconductor Dot/Rods

The crystalline dot/rods were synthesized according to the method developed by Carbone et al. [15]. For the CdSe seeds the ligands, 3.0 g trioctylphosphine oxide (TOPO) and 0.28 g octadecylphosphonic acid (ODPA), were mixed in a 25 mL three-neck-flask with 0.06 g CdO and heated to 150 °C under vacuum for one hour. Afterwards, the temperature was increased to 300 °C until the CdO had dissolved and the solution became colorless. After 0.9 mL trioctylphosphine (TOP) had been added at 380 °C, 0.058 g Se in 0.430 mL TOP were quickly injected. The solution was stirred vigorously for 2.5 minutes and subsequently cooled down fast. The solution was dried under nitrogen and redispersed in 5 mL TOP stored inside the glove box until further use.

For the CdS shell, again the ligands, here 0.29 g ODPA, 0.08 g hexylphosphonic acid (HPA) and 3.0 g TOPO, were mixed with 0.086 g CdO in a three-neck-flask and dried under vacuum for one hour at 150 °C. Again, the mixture was heated (to 350 °C) until the CdO was dissolved. 0.9 mL TOP was added. Subsequently, a mixture of 0.120 g S dissolved in 1.5 mL TOP and 1 mL of a 4 nM QD solution were injected into the flask. After a reaction time of 8 min, the solution was cooled down quickly. The product was precipitated with methanol and after centrifugation redispersed in hexane.

### 5.1.3 Syntheses of Gold Nanorods

Different syntheses were performed, different parameters and advantages were studied. In all GNR syntheses ultrapure water (with a resistivity of 18.2 MΩ) was used. Tetrachloroauric acid trihydrate was used as gold precursor. It was essential for the success of the syntheses to store sodium boron hydride under nitrogen atmosphere.

#### 5.1.3.1 Synthesis of GNR stabilized with CTAB

A seeded-growth synthesis developed by El-Sayed et al. was used [94]. 5 mL of a 0.2 M CTAB solution were mixed with 5 mL 0.005 M Au<sup>3+</sup> solution. Under vigorous stirring 600 µL of an ice-cold and freshly-prepared sodium boron hydride solution were added. After 2 min of stirring the amber-colored seed solution was kept at room temperature for 2 hours.

The growth solution was prepared by mixing 5 mL 0.2 M CTAB solution with 0.001 M  $\text{Au}^{3+}$  solution and 150  $\mu\text{L}$  0.004 M  $\text{AgNO}_3$  solution. After the addition of 60  $\mu\text{L}$  of 0.1 M ascorbic acid solution the milky-yellow solution turned colorless. The growth of the GNR was started when 10  $\mu\text{L}$  of the seed solution were added. During 2 hours in a water bath with 30 °C the solution got its characteristic color. The GNR were washed and concentrated by centrifugation with 10000 rpm for 12 minutes.

#### **5.1.3.2 Synthesis of GNR using CTAB and NaOL as surfactant**

The seeded-growth method developed by the Murray group enabled the synthesis of various GNR aspect ratios [131]. In the following, one procedure is described exemplarily, while the others are listed below.

Again, the preparation was divided into a seed nucleation and a growth step. All glass devices were carefully cleaned with aqua regia and subsequently washed with ultrapure water before use. For the growth solution, 7 g CTAB and 1.234 g NaOL were dissolved in water at 50 °C. After the solution had cooled down to 30 °C, 18 mL 0.004 M  $\text{AgNO}_3$  solution were added and the solution was kept undisturbed at 30 °C for 30 min. Consequently, 250 mL 0.001 M  $\text{Au}^{3+}$  solution were added and the orange-yellow mixture was stirred until it was colorless for 90 min with 700 rpm at 30 °C.

In-between, the seed solution was prepared. 5 mL of a 0.2 M CTAB solution were mixed with 5 mL of a 0.0005 M  $\text{HAuCl}_4$  solution in a 20 mL glass vial. The yellowish solution was stirred with 1200 rpm when 600  $\mu\text{L}$  of a 0.01 M freshly prepared sodium boron hydride solution filled up with water to 1 mL was quickly injected. After 2 min of stirring the solution was aged for 30 min while it changed its color from blue-grey to amber.

To the now colorless growth solution 2.1 mL concentrated HCl was admixed while stirring with 400 rpm. The speed was increased to 1200 rpm and 1.25 mL 0.064 M ascorbic acid and after 30 s of stirring 0.8 mL seed solution were added. The solution was stirred for another 30 s. The growth solution was aged for 14 hours while it became brownish-pink. The GNR were centrifuged for 30 min at 7000 rpm.

In the following this synthesis procedure is referred to as standard synthesis. An overview of the utilized procedures is given in the table below:

Nr.	CTAB /g	NaOL /g	4 mM AgNO <sub>3</sub> /mL	HCl /mL	Seed /mL
1	7	1.234	18	2.1	0.8
2	9	1.234	36	3.0	0.2
3	9	1.234	24	2.1	0.4
4	7	1.234	12	2.1	0.2
5	7	1.234	18	1.5	0.4
6	7	1.234	24	5.6	0.8
7	7	1.234	24	4.8	0.8
8	7	1.234	12	2.1	0.8
9	9	1.234	12	2.1	0.8

**Variation of the Parameters** The standard synthesis was performed with drastic changes. The table below lists the parameter that was changed and the corresponding factor by which it was increased or reduced.

Parameter	Factor
AgNO <sub>3</sub>	1.5
AA	1.33
NaBH <sub>4</sub>	1.5
NaBH <sub>4</sub>	0.166
Stirring rate seeds	0.166
Stirring rate seeds	0
Stirring rate total	0

The rest of the synthesis was performed as described for the standard synthesis.

## 5.1.4 Ligand Exchange

### 5.1.4.1 Ligand Exchange with Octadecanethiol

A modified synthesis from Lin and coworkers was used [72]. To start the ligand exchange reaction 10 mL of a 10 mM octadecanethiol solution in ethanol was prepared and added to 3 mL of the aqueous CTAB capped GNR solution from the standard synthesis. The milky-pink solution with dark red flakes was stirred for 24 hours. After centrifugation at 3500 rpm for 20 min the supernatant was discarded and the precipitate was redispersed



in 40 mL water. After freeze drying the dark reddish solid was redispersed in 5 mL of chloroform or toluene.

#### 5.1.4.2 Ligand Exchange with PEGMUA

The experiments were performed in collaboration with Dr. Florian Schulz, who also provided the ligand,  $\alpha$ -methoxypoly-(ethylene glycol)- $\omega$ -(11-mercaptoundecanoate) (PEG-MUA). It was synthesized according to Schulz et. al [112].

**Ligand Exchange with Incubation** In this method, PEGMUA solution was added to the CTAB stabilized GNR solution and incubated for a certain amount of time. The ligand exchange was tested by oxidative etching with cyanide (5.1.5).

**Ligand Exchange with Extraction** 10  $\mu$ L GNR stock solution were diluted with ultrapure water (1:1). The excessive CTAB was removed by five times extraction with 10 mL chloroform, respectively. The remaining chloroform was eliminated from the aqueous phase in the ultrasonic bath (10 min). To one half of the extracted GNR solution 1 mL 1 mM PEGMUA solution was added. The other half was filled up with the same volume of ultrapure water, before both solution volumes were adjusted to 15 mL with ultrapure water. These solutions were further analyzed with cyanide etching experiments (5.1.5).

#### 5.1.5 Etching Experiments

All etching experiments discussed in this work were conducted with the same GNR sample. The dimensions and size distributions of this sample are given below:

Length /nm	Width /nm	Aspect ratio
85.68 $\pm$ 9.16	28.91 $\pm$ 2.42	2.83 $\pm$ 0.31

Three different stock solutions were prepared for etching with 25 mM KCN solution:

- GNR@CTAB\_2xMQ - after synthesis, 30 mL of the solution were centrifuged twice with 7000 g and the supernatant was replaced with ultrapure water (MQ), respectively.

- GNR@PEGMUA\_2xMQ - after synthesis, 35 mL of the solution were centrifuged with 6000 g and the supernatant was replaced with 35 mL of a 1 mM PEGMUA solution. The centrifugation was repeated twice, while the supernatant was replaced with the same volume of MQ water.
- GNR@3xPEGMUA - after synthesis 35 mL of the solution were centrifuged with 6000 g. The supernatant was replaced with 35 mL of a 1 mM PEGMUA solution, respectively.

**Monitoring** The two stock solutions GNR@PEGMUA\_2xMQ and GNR@3xPEGMUA were extracted with chloroform as described above, resulting in 2 different solutions for each stock solution: \_ex\_PEGMUA and \_ex\_MQ. The two solutions, to which after extraction PEGMUA has been added were purified by centrifugation. The following concentrations were determined:

Sample	Concentration /nM
GNR@PEGMUA_2xMQ_ex_PEGMUA	0.15
GNR@PEGMUA_2xMQ_ex_PEGMUA_purified	0.25
GNR@PEGMUA_2xMQ_ex_MQ	0.25
GNR@3xPEGMUA_ex_PEGMUA	0.08
GNR@3xPEGMUA_ex_PEGMUA_purified	0.11
GNR@3xPEGMUA_ex_MQ	0.10

To these 6 samples KCN solution was added so that the cyanide concentration was adjusted to 25 mM. The etching was monitored with time-resolved UV/Vis spectroscopy over 16 to 48 h, by taking one spectrum every 5 minutes.

**PEGMUA Concentration** In addition to the monitoring of the ligand exchange by extraction, the necessary concentration for a closed ligand shell was investigated. Therefore, extracted and not-extracted samples were prepared.

For the samples without extraction, a defined amount of PEGMUA solution was added to small amounts of the stock solution GNR@CTAB\_2xMQ so that the PEGMUA concentration was adjusted 10, 20, 30, 40, 50 75, 100, 150, and 300  $\mu$ M, respectively. The samples were incubated at room temperature for 16 h. Afterwards the oxidative etching

with 25 mM KCN was started and spectra were recorded to document the temporal evolution. The above described samples were prepared twice. The second sample batch was purified after incubation by centrifugation before the etching reaction was started. These two batches are in the following referred to as GNR@CTAB\_2xMQ\_raw and GNR@CTAB\_2xMQ\_purified.

For the concentration experiments with ligand exchange by extraction, PEGMUA was added before and after the extraction (PEGMUA conc. 1 and conc. 2). Consequently, there are two incubation times (t1 and t2). the second incubation time was kept constant (t2 = 1-2 hours). The different experiments are listed as tables below. The PEGMUA concentration was defined by amount that is added instead of the total concentration. The concentration refers to the final sample volume. The GNR (final) concentration was 0.35 nM.

	sample	conc. 1 / $\mu$ M	t1	conc. 2 / $\mu$ M
Series 1:	1	10	2	5
	2	10	2	10
	3	10	2	15
	4	10	2	20
	5	10	2	25
	6	10	2	30
	7	10	2	40
	8	10	2	70
	9	10	2	100
	10	10	2	140

	sample	conc. 1 / $\mu$ M	t1	conc. 2 / $\mu$ M
Series 2:	1	10	16	10
	2	10	16	15
	3	10	16	20
	4	10	16	30
	5	10	16	40
	6	10	16	80
	7	10	16	100
	8	10	16	140

Series 3:	sample	conc. 1 / $\mu$ M	t1	conc. 2 / $\mu$ M
	1	25	16	5
	2	25	16	10
	3	25	16	15
	4	25	16	20
	5	25	16	30
	6	25	16	40
	7	25	16	60
	8	25	16	80
	9	25	16	100
	10	25	16	125

After the second incubation time  $t_2$ , the etching with 25 mM KCN solution was started and spectra were taken over a period of 14 d.

**TEM monitoring** For the monitoring with electron microscopy, an etching reaction with a 50 mM KCN solution was started with extracted GNR. After 30, 50 and 70 minutes samples were taken and for which the etching reaction was stopped. Therefore, the solution was centrifuged and the supernatant was substituted with ultrapure water. TEM samples were prepared on carbon coated copper grids.

## 5.2 Sample Preparation - Physical Methods and Surface Techniques

### 5.2.1 Fabrication of GNP Films - Layer-by-Layer Spin Coating

The in the group developed technique to produce GNP membranes was used [111]. A glass slide was cleaned ultrasonically for 5 minutes in acetone. It was rinsed in ultrapure water and dried under a nitrogen stream. Afterwards, the glass slide was rotated on the spin coater plate with 3000 rpm. One layer of GNP was deposited by a subsequent deposition of 10  $\mu$ L GNP solution in toluene and two 10  $\mu$ L droplets of the thiol solution. The thiol solution was composed of 17.3 mg 1,12-dodecane thiol in 10 mL of a toluene ethanol mixture (1:19). Each layer was dried under rotation for 30 s. In

total 3 layers were deposited so that a closed film was produced. The GNP solution had a concentration of  $1.8 \times 10^{-7}$  M, determined with an empirical formula [47]. The utilized particles were  $3.7 \pm 0.6$  nm.

### 5.2.2 Fabrication of horizontally and vertically aligned GNR

For the fabrication of horizontal and vertical alignments, a matrix of different film deposition techniques, substrates and GNR solutions with different additives was tested. All samples were characterized with SEM.

#### 5.2.2.1 Substrate

A variety of different substrates and their interactions with the GNR were investigated:

- glass slides (1)
- glass slides with an amorphous carbon film (2)
- glass slides with a thin PS layer (3)
- glassy carbon disks (4)
- silicon wafers (5)
- glass slides with a PS soft lithographic pattern (6)
- glass slides with a TMOS soft lithographic pattern (7)
- SiN membranes of defined thickness (8)

#### 5.2.2.2 Film Deposition Techniques

**Spin Coating** The technique was used under different conditions.

Parameter	Variation
Solvent	Water, toluene
Substrates	1, 3, 6, 7
Speed	500, 1000, 2000, 3000 rpm

Depending on the substrate, different specially designed spin coating plates were used. The spin coating plates were cleaned ultrasonically in acetone before each use.

**Dip Coating** The substrate (3, 6, 7) was immersed in 1.2 mL of a 70 nM GNR solution. It was lifted with a speed of 5 mm/min or 2 mm/min.

**Langmuir-Blodgett** The Langmuir-Blodgett experiments were performed under the use of a Langmuir trough from KSV Nima. According to the published method by Lin et al., the GNR in chloroform stabilized with octadecanethiol were applied on the aqueous phase [72]. After the organic solvent had evaporated, the surface layer was compressed with a barrier speed of 2 cm<sup>2</sup>/s. The compressed film was transferred to a hydrophobized glass slide by vertical dipping.

**Droplet Evaporation** A defined amount of GNR solution was drop casted on the prepared substrate. The solvent was allowed to evaporate while a spherical residue emerged. The following parameters were investigated:

Parameter	Variation
Droplet volume	1, 5, 10, 15 $\mu$ L
Substrates	1, 2, 4, 5, 8
Drying speed	vacuum pump, air, closed system

### 5.2.2.3 HV Cell

An impedance cell was cleaned and two electrodes were connected to a high-voltage supply. Between the two electrodes, two clean glass slides were mounted, separated by an o-ring. 3  $\mu$ L of a 70 nM GNR solution were deposited in the center of the lower glass slide and mounted (fig. 5.1). Voltages of 1.0, 1.2 and 2.2 were applied for 7.5 hours on different samples, respectively.

### 5.2.2.4 GNR Solution

**Aqueous solvent** The concentration of the GNR was varied. For samples prepared by spin coating, the wettability of the solvent was improved with the addition of 25

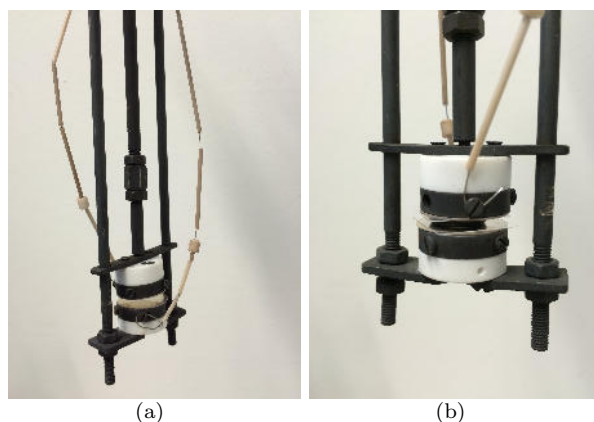


FIGURE 5.1: Pictures of the interior of the HV cell.

vol% ethanol or dioxane. In addition to this, the aqueous ligand system was used for dip coating and droplet evaporation.

**DMSA** 8 tubes containing 200  $\mu\text{L}$  GNR-DMSA mixtures were prepared. The final GNR concentration was 15 nm. The DMSA concentration was adjusted to 0.2, 0.5, 0.8, 1.0, 1.5, 2.0, 3.0, 3.5 mM, respectively. The tubes were incubated for 24 hours in a water bath of 28  $^{\circ}\text{C}$ . Afterwards 10  $\mu\text{L}$  of each solution were drop casted on a clean glass slide.

**NaCl** 0.006 g NaCl were added to 1 mL of the GNR solution, so that the final NaCl concentration was 0.1 M. The GNR solution was adjusted to 70 nM and 10  $\mu\text{L}$  of this solution was drop casted on a silicon wafer. It was dried at 20  $^{\circ}\text{C}$ .

**Organic Solvent** Samples of the octadecanethiol stabilized GNR were prepared with spin coating, Langmuir-Blodgett film deposition and drop casting.

### 5.2.3 Sample Preparation for CLSM Measurements

#### 5.2.3.1 GNP substrate

The GNP film was partly removed with a medical cotton stick that was soaked with acetone. Afterwards a poly(vinyl formal) film was deposited by spin coating of a polymer solution in chloroform with 4000 rpm. The concentration of the solution determined the

thickness of the film. It was varied from 0.015 to 0.6 wt%. After the polymer film has solidified, 30  $\mu\text{L}$  of a 1 nM SNR solution were spin coated with 3000 rpm.

### 5.2.3.2 GNR substrate

The SiN substrate was cleaned with oxygen plasma at 50 W and 27 Pa for 5 minutes. Afterwards a 1  $\mu\text{L}$  droplet of the washed, 80 nM GNR solution was deposited on the substrate. For this case, it was lying on a clean glass slide in the center of an o-ring with a diameter of 0.9 cm. The substrate was covered with another clean glass slide and the setup was covered with a heavy weight to slow down the evaporation process.

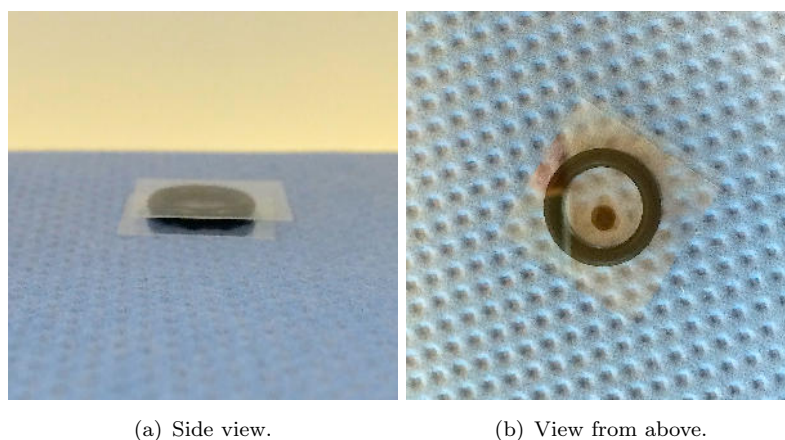


FIGURE 5.2: Pictures of droplet-drying setup.

A picture of the setup before ballasting is shown in fig. 5.2. After approximately 5 days the droplet had dried and the SNR were deposited. 25  $\mu\text{L}$  of a 1 nM SNR solution in toluene were spin coated with 4000 rpm on the other side of the SiN substrate. Here fore, a specially designed spin coating plate was used. The sample was afterwards fixed in the center of an objective slide.

## 5.3 Characterization Techniques

### 5.3.1 Absorption Spectroscopy

UV/Vis and UV/Vis-NIR spectroscopy was used to measure the absorbance of SNR and GNR, respectively. The measurements were performed with a Cary 50 or Cary 500 from



Varian. The spectral resolution of the used instruments was 1 nm. The technique and the drawn conclusions are based on the Lambert Beer law:

$$A = \varepsilon \cdot c \cdot d \quad (5.1)$$

where  $A$  is the absorbance of the sample,  $\varepsilon$  is the material specific extinction coefficient,  $c$  the concentration of the investigated substance and  $d$  the diameter of the cuvette (in this case 1 cm). All GNR concentrations were determined from their optical density at the LSPR wavelength [2, 98].

### 5.3.2 Emission Spectroscopy

The emission of the fluorescing SNR was determined from the ensemble in solution. This was done with a FluoroMax-4 from Jobin/Yvon. The spectrometer was operated with a xenon lamp. For the spectra shown in this work, the emission wavelength was set to 488 nm in order to assure the comparability with the CLSM measurements. The detector of the instrument was a photomultiplier. The grating of the monochromator was blazed.

The Quantum yield of the SNR was determined against Rhodamine 6G. For the Rhodamine in solution, few crystals of the dye were dissolved in 3 mL ethanol. It was handled with care, so that no air bubbles were inclosed and could influence the measurement.

### 5.3.3 Transmission Electron Microscopy

Transmission electron microscopy (TEM) is a main imaging technique, that uses the interaction of electrons with the investigated sample in order to gain information about the species. Under an applied acceleration voltage of 100 kV the electrons have a de Broglie wavelength of 0.0039 nm. Hence, the instrument has a resolution of 0.19 nm. This high resolution makes the transmission electron microscope an adequate tool for the characterization of nanocrystals.

For the image, the beam of highly accelerated electrons is focussed with electromagnetic lenses on the thin sample. In order to avoid unwanted scattering before the electrons interact with the specimen, the TEM has to be operated under high vacuum.

In this work, the TEM was operated in the bright field mode. In this mode, the objective lens is set in a way that only the primary electrons pass the column, which means that the vacuum appears as the brightest.

Three different types of interaction between electron beam and specimen result in different types of contrasts. Inelastic scattering with the electron beam and the atomic nuclei generate a dark/bright contrast, while the inelastic scattering with the electron shell creates a diffuse background. This most primitive of all contrasts leads for thin specimen to the mass/thickness contrast. The thin areas and the areas with the lowest mass (or atomic number) are imaged as the brightest.

Secondly, the diffraction contrast gives information about the crystallinity of the sample and can be used for a defect analysis. The electron beam is diffracted on the lattice planes of the sample. The diffraction pattern can be obtained, when the electron beam is focused on the back focal plane.

In addition to this, the phase contrast can image the lattice spacings of the crystal. Because of the diffracted and undiffracted rays a phase difference evolves which leads to an interference pattern [29]. Furthermore, x-ray fluorescence is generated (EDX). The elements of the sample can be identified by their characteristic x-ray lines. The intensity of the lines depends on the ratio of the elements, respectively. If instead of the imaging mode, the sample is scanned, the correlation of EDX and Z contrast enables atomic resolution in the STEM (Scanning Transmission Electron Microscopy) mode.

For this work, the TEM characterization was done with a Jeol JEM-1011 ( $V=100$  kV) and a Jeol-JEM 2200 FS (UHR) operated with an acceleration voltage of 200 kV. As substrates, copper grids covered with a carbon film were used. The diluted SNR sampled were deposited and the excess solvent was removed. For GNR sample preparation, the GNR were stabilized with PEGMUA and the aqueous solution dried at room temperature.

### 5.3.4 Atomic Force Microscopy

The thickness of the polymer layer and thus the distance between GNP film and SNR was determined with atomic force microscopy (AFM). The measurements were performed with a multimode AFM from Veeco Instruments under the use of the NanoScope-IV-controller. A silicon tip from Bruker was mounted.

The technique atomic force microscopy is a sensitive method to image the sample surface. A small tip (mostly Si or SiN) that is glued to a several hundred nm cantilever is brought to a distinct distance (constant height mode) to the surface and scans the surface line by line. The cantilever is bended according to the surface-tip interaction that can be distance dependently either attractive or repulsive. It follows the Lennard-Jones potential. A laser is focused on the cantilever and its deflection according to the cantilever bending is detected by a four times segmented photodiode. In the dynamic mode, the cantilever oscillates constantly and its frequency changes at another distance. In the constant height mode this means there is a change in sample height [64, 86].

### 5.3.5 Scanning Electron Microscopy

#### 5.3.5.1 Setup and Working Principle

In a scanning electron microscope (SEM), an electron beam is produced, guided and focused through a condenser, an objective and an aperture on the conductive sample. Between objective and aperture, a scan generator with scanning coils enables the scan of the sample point by point.

The scanning electron microscope detects the signal, in contrast to the before described TEM, above the sample. The electron beam hits the sample and penetrates into it. Inside the sample, the electrons of the beam are inelastically and elastically scattered by the nuclei and electrons of the sample material. The electrons that leave the sample are detected. The interaction volume of electron beam and sample is proportional to the acceleration voltage and reversely proportional to the atomic number of the sample. Two kind of particles are detected; electrons (Auger electrons, secondary electrons and back scattered electrons) and x-ray (Bremsstrahlung from decelerating electrons, x-rays

due to the filling of holes in inner shells created by electron collision and XRF due to excitations by fluorescent x-rays).

According to their energies, the in different processes produced electrons come from different depths of the sample, respectively. Auger electrons and secondary electrons (SE) can only escape from regions close to the surface, while backscattered electrons represent deeper layers of the sample. For the detection, an Everhart-Thornly detector was used. With an applied voltage of 300 V, it can resolve the SE image.

In this work, a Quanta 3D from FEI with a Schottky emitter and an acceleration voltage between 20 and 30 kV was used. The more detailed images were recorded with a 1550 Gemini from Zeiss including a field emitter with acceleration voltages between 2 and 30 kV.

### **5.3.5.2 Measurement Procedure**

SEM was used for the correlation of the fluorescence and transmission data with electron microscopy. In a way, this correlation bridges the resolution gap due to the numerical aperture in light microscopy.

The SiN membranes purchased from Plano GmbH were composed of 8 plus 1 windows. This one rectangular window allowed to keep the same orientation for electron and light microscopy. On the basis of the transmission images from the SiN windows and the characteristic GNR islands, the same region investigated with the CLSM could be imaged with SEM (fig. 5.3).

### **5.3.6 CLSM and TCSPC**

#### **5.3.6.1 Setup and Working Principle**

The optical measurements of single SNR on ordered GNR were performed with a confocal laser scanning microscope (CLSM) and a coupled time correlated single photon counting unit (TCSPC). The inverted confocal laser scanning microscope FV 1000 from Olympus had four integrated continuous wave (cw) lasers whose signal were fed into the microscope setup via an acousto-optical modulator. The light was focussed on the sample with an

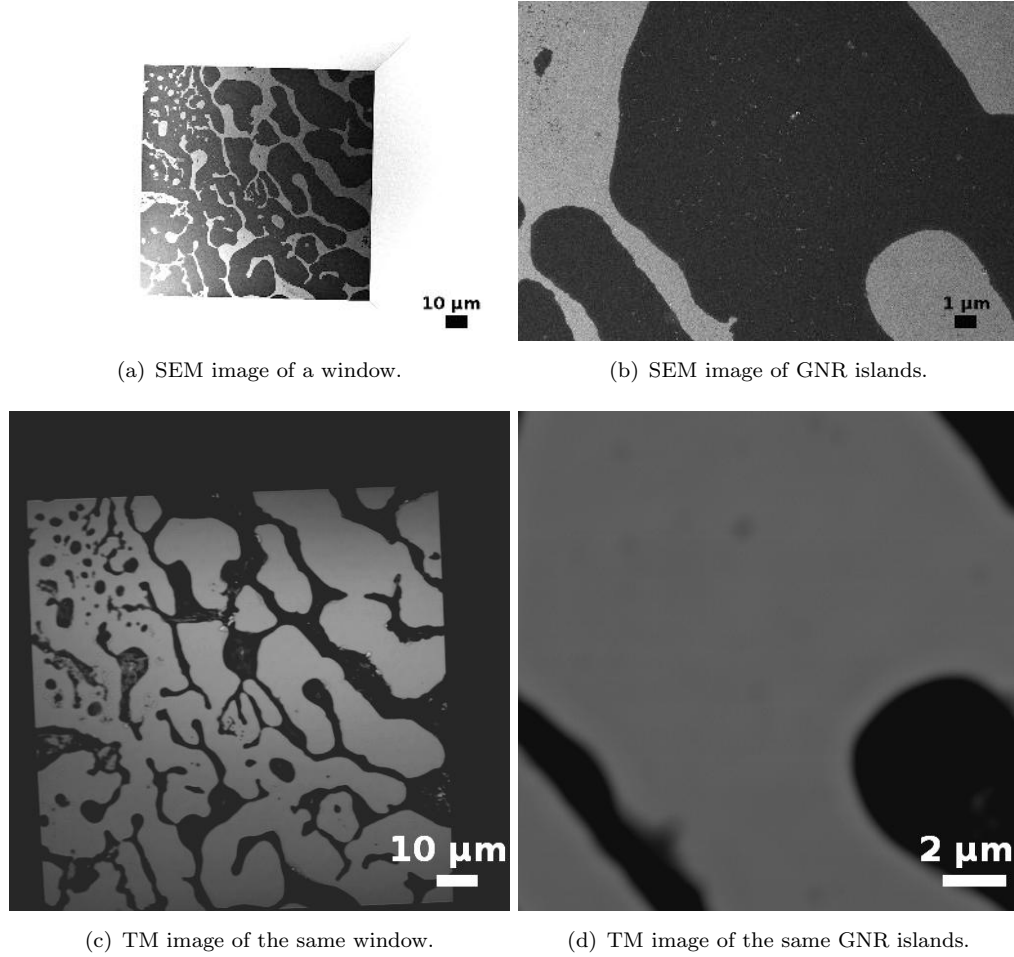


FIGURE 5.3: Corresponding SEM and TM images from the window and the scanned frame, respectively.

objective. In this work, a MPlanFLN air objective with a numerical aperture of 0.9 and a 60 x magnification was used. The emission from the sample was guided through a galvanometric mirror, and passed after filtering out the laser frequency by an dichroic mirror the confocal pinhole. The microscope setup is schematically shown in figure 5.4. For the current measurements, the pinhole aperture was set to 280 μm.

After passing the pinhole, the signal could be detected by three different microscope-internal photomultipliers and a detector for the transmission image. Alternatively, it could also be guided to a spectrometer. This possibility was used for the GNP samples, where the FWHM of the recorded emission spectra proved that a single SNR was analyzed. The spectral resolution for the Triax spectrometer from Horiba was 2.4 nm.

For the case of single SNR, the detectors of the microscope were not sensitive enough, which is why all images were taken with the TCSPC setup. Thus, instead of using the

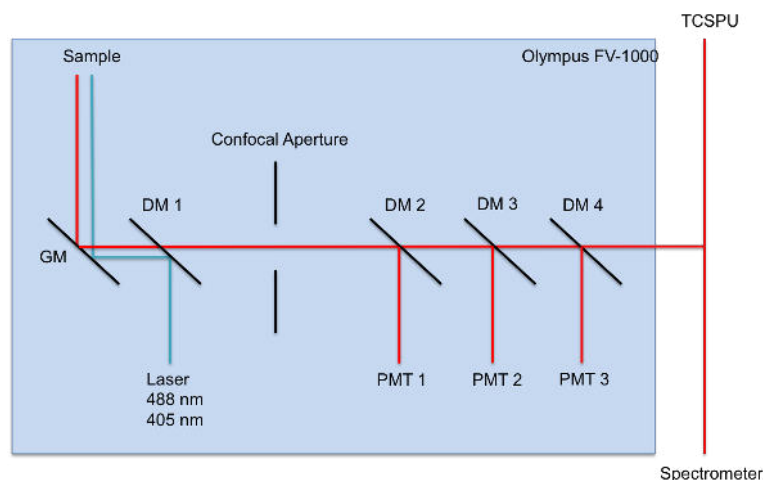


FIGURE 5.4: A sketch of the FV 1000 setup.

photomultipliers, the signal was filtered by three more dichroic mirrors and fed into an avalanche photodiode (APD) from Perkin Elmer (SPCM-AQR) via a fiber optic cable. The power for the APD came from the DSN module. The signal was converted into an electrical TTL (transistor-transistor logic) signal and guided into the router PHR 800, which made the direct correlation of the single photons possible. The Pico Harp 300 was responsible for the delivery of the lifetime histograms to the computer. The setup is illustrated in Figure 5.5.

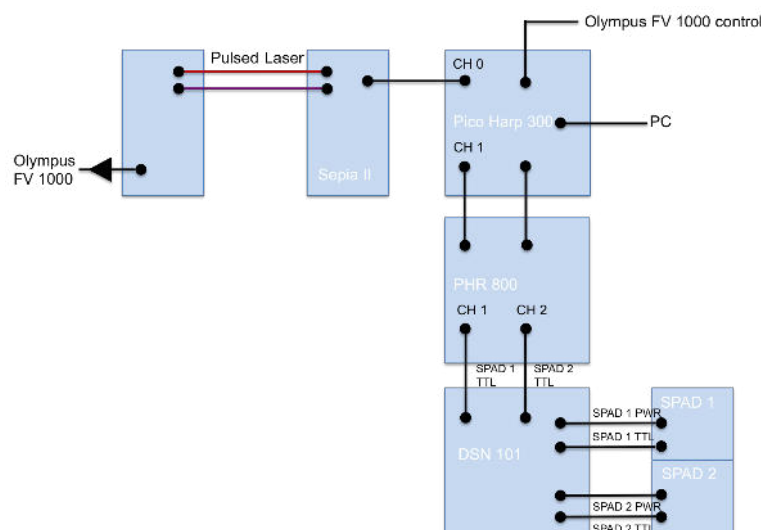


FIGURE 5.5: Schematic representation of the TCSPC connections.

The PicoQuant system enabled the extraction of lifetime information from the fluorescing sample. For this, the pulsed laser diodes at 405 nm from Picoquant was fed into the confocal setup. Repetition rates of 5 MHz, 10 MHz, 20 MHz, 40 MHz, and 80 MHz could be chosen.

To be more precise, the TCSPC method is based on subtraction of laser pulse time marker (the sync signal) and the photon detection time marker. Both times are exactly determined by a constant fraction discriminator (CFD). The signals from the CFD are converted by a TDC (time to digital converter) and add up to the lifetime histogram. The histogram of the different time bins evolves over many laser pulse cycles. The uninterrupted data flow is called time-tagged time-resolved (TTTR) mode. Additionally, the PicoQuant system was operated in the reverse start stop mode, in order to minimize the instrument response function (IRF) [124].

### 5.3.6.2 Measurement

**IRF** The instrument response function is the minimum lifetime that can be resolved. It is determined, by setup's response times. It was measured and used for the reconvolution fitting of the obtained lifetime data. On that account, a micro molar concentrated fluorescein solution was quenched with a saturated KI solution. Point measurements in the T3 mode were taken from this solution with different repetition rates. Since the lifetime of the quenched dye is shorter than the shortest resolvable lifetime, this measurement gave the IRF. The IRF was determined to be 450 ps.

**Measurement Procedure** The prepared SiN membranes were centered on an objective slide and fixed on the microscope stage, whereas the SNR side was facing the objective. Transmission images were taken from the SiN windows for the later correlation with SEM. The fluorescence image of the same section was scanned with the 488 nm laser. At the fluorescence points, point measurements with the excitation wavelengths 488 nm and 405 nm were recorded for 60 s and a repetition rate of 10 and 20 MHz. In addition to this, Fluorescence Lifetime Imaging Microscopy (FLIM) with the pulsed 405 nm laser diode were recorded to collect lifetime-resolved images from the exact same sample excerpt. The scanning speed was 2000  $\mu\text{s}/\text{px}$  for all PL images. The scattered laser light was blocked by a 500 nm longpass filter.

**Data Processing** For the fluorescence intensity data evaluation Igor Pro 6.0 was used. The fluorescence lifetime decays were fitted with FluoFit from PicoQuant. By

courtesy of Dr. Sandra Flessau, the time traces could be interpreted with a mathematica script delivering on- and off-times as well as the universal power law fit [30].

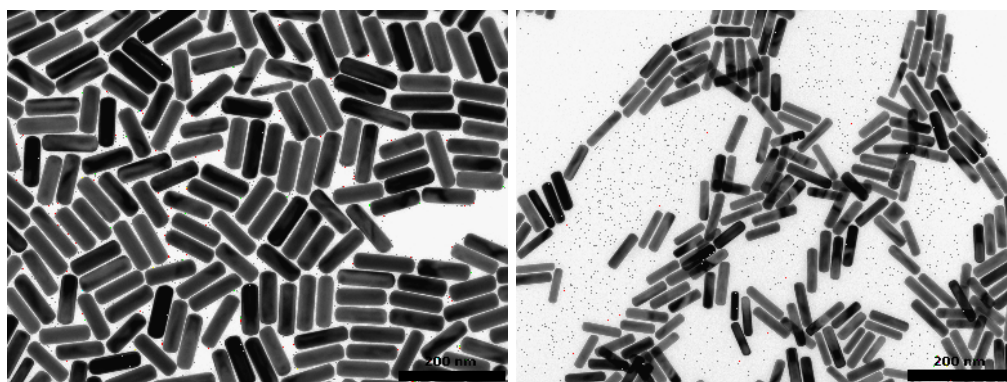


# Appendix A

## Additional Data

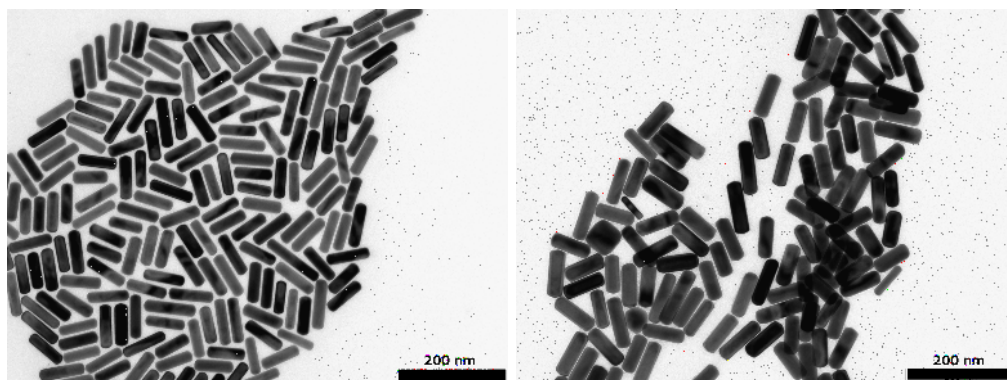
### A.1 Parameter Variation in the GNR Synthesis

TEM images:



(a) 1.5 x silver nitrate.

(b) 1.33 x AA.



(c) 1.5 x  $\text{NaBH}_4$ .

(d) Without stirring.

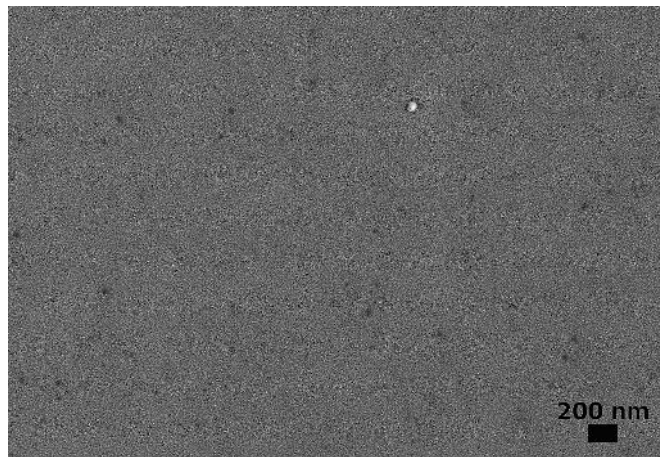
FIGURE A.1: TEM images of GNR synthesized with varied parameters.

Size distribution:

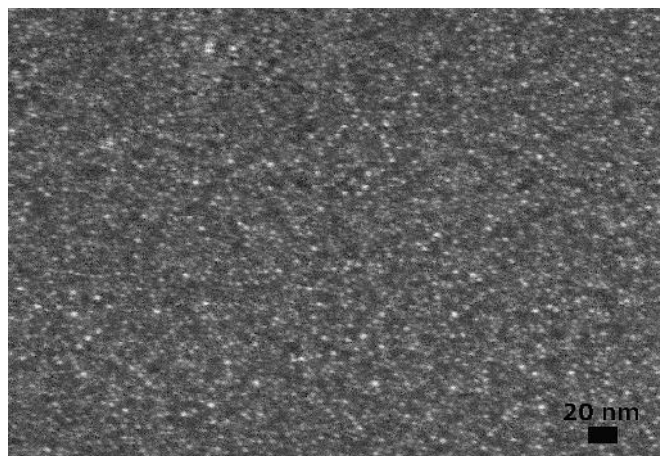
Varied Parameter	Length /nm	Width /nm	Aspect ratio
AgNO <sub>3</sub>	100.82±7.24	30.63±1.40	3.28±0.29
AA	77.32±7.22	19.31±1.47	4.00±0.39
NaBH <sub>4</sub>	75.41±7.38	21.35±1.64	3.57±0.52
Stirring	77.50±6.07	19.18±1.35	3.87±0.43

## A.2 GNP Film

SEM image of the 3 layer GNP film on glass slides:



(a) Overview.



(b) Inset.

FIGURE A.2: SEM images of a GNP film on a glass slide.

## Appendix B

# Chemicals

### B.1 All H, EUH and P Statements

TABLE B.1: All H, EUH, and P Statements.

Identifier	Statement
H200	Unstable explosives.
H201	Explosive; mass explosion hazard.
H202	Explosive, severe projection hazard.
H203	Explosive; fire, blast or projection hazard.
H204	Fire or projection hazard.
H205	May mass explode in fire.
H220	Extremely flammable gas.
H221	Flammable gas.
H222	Extremely flammable aerosol.
H223	Flammable aerosol.
H224	Extremely flammable liquid and vapour.
H225	Highly flammable liquid and vapour.
H226	Flammable liquid and vapour.
H228	Flammable solid.

*continues on next page*

---

Identifier	Statement
H240	Heating may cause an explosion.
H241	Heating may cause a fire or explosion.
H242	Heating may cause a fire.
H250	Catches fire spontaneously if exposed to air.
H251	Self-heating: may catch fire.
H252	Self-heating in large quantities; may catch fire.
H260	In contact with water releases flammable gases which may ignite spontaneously.
H261	In contact with water releases flammable gases.
H270	May cause or intensify fire; oxidiser.
H271	May cause fire or explosion; strong oxidiser.
H272	May intensify fire; oxidiser.
H280	Contains gas under pressure; may explode if heated.
H281	Contains refrigerated gas; may cause cryogenic burns or injury.
H290	May be corrosive to metals.
H300	Fatal if swallowed.
H301	Toxic if swallowed.
H302	Harmful if swallowed.
H304	May be fatal if swallowed and enters airways.
H310	Fatal in contact with skin.
H311	Toxic in contact with skin.
H312	Harmful in contact with skin.
H314	Causes severe skin burns and eye damage.
H315	Causes skin irritation.
H317	May cause an allergic skin reaction.
H318	Causes serious eye damage.

---

*continues on next page*

Identifier	Statement
H319	Causes serious eye irritation.
H330	Fatal if inhaled.
H331	Toxic if inhaled.
H332	Harmful if inhaled.
H334	May cause allergy or asthma symptoms or breathing difficulties if inhaled.
H335	May cause respiratory irritation.
H336	May cause drowsiness or dizziness.
H340	May cause genetic defects. <i>&lt;state route of exposure if it is conclusively proven that no other routes of exposure cause the hazard&gt;</i>
H341	Suspected of causing genetic defects. <i>&lt;state route of exposure if it is conclusively proven that no other routes of exposure cause the hazard&gt;</i>
H350	May cause cancer. <i>&lt;state route of exposure if it is conclusively proven that no other routes of exposure cause the hazard&gt;</i>
H351	Suspected of causing cancer. <i>&lt;state route of exposure if it is conclusively proven that no other routes of exposure cause the hazard&gt;</i>
H360	May damage fertility or the unborn child. <i>&lt;state specific effect if known&gt; &lt;state route of exposure if it is conclusively proven that no other routes of exposure cause the hazard&gt;</i>
H361	Suspected of damaging fertility or the unborn child. <i>&lt;state specific effect if known&gt; &lt;state route of exposure if it is conclusively proven that no other routes of exposure cause the hazard&gt;</i>
H362	May cause harm to breast-fed children.

*continues on next page*

Identifier	Statement
H370	Causes damage to organs <i>&lt;or state all organs affected, if known&gt;</i> . <i>&lt;state route of exposure if it is conclusively proven that no other routes of exposure cause the hazard&gt;</i>
H371	May cause damage to organs <i>&lt;or state all organs affected, if known&gt;</i> . <i>&lt;state route of exposure if it is conclusively proven that no other routes of exposure cause the hazard&gt;</i>
H372	Causes damage to organs <i>&lt;or state all organs affected, if known&gt;</i> through prolonged or repeated exposure. <i>&lt;state route of exposure if it is conclusively proven that no other routes of exposure cause the hazard&gt;</i>
H373	May cause damage to organs <i>&lt;or state all organs affected, if known&gt;</i> through prolonged or repeated exposure. <i>&lt;state route of exposure if it is conclusively proven that no other routes of exposure cause the hazard&gt;</i>
H400	Very toxic to aquatic life.
H410	Very toxic to aquatic life with long lasting effects.
H411	Toxic to aquatic life with long lasting effects.
H412	Harmful to aquatic life with long lasting effects.
H413	May cause long lasting harmful effects to aquatic life.
H350i	May cause cancer by inhalation.
H360F	May damage fertility.
H360D	May damage the unborn child.
H361f	Suspected of damaging fertility.
H361d	Suspected of damaging the unborn child.
H360FD	May damage fertility. May damage the unborn child.

*continues on next page*

Identifier	Statement
H361fd	Suspected of damaging fertility. Suspected of damaging the unborn child.
H360Fd	May damage fertility. Suspected of damaging the unborn child.
H360Df	May damage the unborn child. Suspected of damaging fertility.
EUH001	Explosive when dry.
EUH006	Explosive with or without contact with air.
EUH014	Reacts violently with water.
EUH018	In use may form flammable/explosive vapour-air mixture.
EUH019	May form explosive peroxides.
EUH044	Risk of explosion if heated under confinement.
EUH029	Contact with water liberates toxic gas.
EUH031	Contact with acids liberates toxic gas.
EUH032	Contact with acids liberates very toxic gas.
EUH066	Repeated exposure may cause skin dryness or cracking.
EUH070	Toxic by eye contact.
EUH071	Corrosive to the respiratory tract.
EUH059	Hazardous to the ozone layer.
EUH201	Contains lead. Should not be used on surfaces liable to be chewed or sucked by children.
EUH201A	Warning! contains lead.
EUH202	Cyanoacrylate. Danger. Bonds skin and eyes in seconds. Keep out of the reach of children.
EUH203	Contains chromium(VI). May produce an allergic reaction.

*continues on next page*

---

Identifier	Statement
EUH204	Contains isocyanates. May produce an allergic reaction.
EUH205	Contains epoxy constituents. May produce an allergic reaction.
EUH206	Warning! Do not use together with other products. May release dangerous gases (chlorine).
EUH207	Warning! Contains cadmium. Dangerous fumes are formed during use. See information supplied by the manufacturer. Comply with the safety instructions.
EUH208	Contains <name of sensitising substance>. May produce an allergic reaction.
EUH209	Can become highly flammable in use.
EUH209A	Can become flammable in use.
EUH210	Safety data sheet available on request.
EUH401	To avoid risks to human health and the environment, comply with the instructions for use.
P101	If medical advice is needed, have product container or label at hand.
P102	Keep out of reach of children.
P103	Read label before use.
P201	Obtain special instructions before use.
P202	Do not handle until all safety precautions have been read and understood.
P210	Keep away from heat/sparks/open flames/hot surfaces. — No smoking.
P211	Do not spray on an open flame or other ignition source.

---

*continues on next page*



Identifier	Statement
P220	Keep/Store away from clothing/.../combustible materials.
P221	Take any precaution to avoid mixing with combustibles ...
P222	Do not allow contact with air.
P223	Keep away from any possible contact with water, because of violent reaction and possible flash fire.
P230	Keep wetted with ...
P231	Handle under inert gas.
P232	Protect from moisture.
P233	Keep container tightly closed.
P234	Keep only in original container.
P235	Keep cool.
P240	Ground/bond container and receiving equipment.
P241	Use explosion-proof electrical/ventilating/lighting/... equipment.
P242	Use only non-sparking tools.
P243	Take precautionary measures against static discharge.
P244	Keep reduction valves free from grease and oil.
P250	Do not subject to grinding/shock/.../friction.
P251	Pressurized container: Do not pierce or burn, even after use.
P260	Do not breathe dust/fume/gas/mist/vapours/spray.
P261	Avoid breathing dust/fume/gas/mist/vapours/spray.
P262	Do not get in eyes, on skin, or on clothing.
P263	Avoid contact during pregnancy/while nursing.
P264	Wash ... thoroughly after handling.

*continues on next page*

Identifier	Statement
P270	Do not eat, drink or smoke when using this product.
P271	Use only outdoors or in a well-ventilated area.
P272	Contaminated work clothing should not be allowed out of the workplace.
P273	Avoid release to the environment.
P280	Wear protective gloves/protective clothing/eye protection/face protection.
P281	Use personal protective equipment as required.
P282	Wear cold insulating gloves/face shield/eye protection.
P283	Wear fire/flame resistant/retardant clothing.
P284	Wear respiratory protection.
P285	In case of inadequate ventilation wear respiratory protection.
P231 + P232	Handle under inert gas. Protect from moisture.
P235 + P410	Keep cool. Protect from sunlight.
P301	IF SWALLOWED:
P302	IF ON SKIN:
P303	IF ON SKIN (or hair):
P304	IF INHALED:
P305	IF IN EYES:
P306	IF ON CLOTHING:
P307	IF exposed:
P308	IF exposed or concerned:
P309	IF exposed or if you feel unwell:
P310	Immediately call a POISON CENTER or doctor/physician.

*continues on next page*

---

Identifier	Statement
P311	Call a POISON CENTER or doctor/physician.
P312	Call a POISON CENTER or doctor/physician if you feel unwell.
P313	Get medical advice/attention.
P314	Get medical advice/attention if you feel unwell.
P315	Get immediate medical advice/attention.
P320	Specific treatment is urgent (see ... on this label).
P321	Specific treatment (see ... on this label).
P322	Specific measures (see ... on this label).
P330	Rinse mouth.
P331	Do NOT induce vomiting.
P332	If skin irritation occurs:
P333	If skin irritation or rash occurs:
P334	Immerse in cool water/wrap in wet bandages.
P335	Brush off loose particles from skin.
P336	Thaw frosted parts with lukewarm water. Do not rub affected area.
P337	If eye irritation persists:
P338	Remove contact lenses, if present and easy to do. Continue rinsing.
P340	Remove victim to fresh air and keep at rest in a position comfortable for breathing.
P341	If breathing is difficult, remove victim to fresh air and keep at rest in a position comfortable for breathing.
P342	If experiencing respiratory symptoms:
P350	Gently wash with plenty of soap and water.
P351	Rinse cautiously with water for several minutes.

---

*continues on next page*

Identifier	Statement
P352	Wash with plenty of soap and water.
P353	Rinse skin with water/shower.
P360	Rinse immediately contaminated clothing and skin with plenty of water before removing clothes.
P361	Remove/Take off immediately all contaminated clothing.
P362	Take off contaminated clothing and wash before reuse.
P363	Wash contaminated clothing before reuse.
P370	In case of fire:
P371	In case of major fire and large quantities:
P372	Explosion risk in case of fire.
P373	DO NOT fight fire when fire reaches explosives.
P374	Fight fire with normal precautions from a reasonable distance.
P375	Fight fire remotely due to the risk of explosion.
P376	Stop leak if safe to do so.
P377	Leaking gas fire: Do not extinguish, unless leak can be stopped safely.
P378	Use ... for extinction.
P380	Evacuate area.
P381	Eliminate all ignition sources if safe to do so.
P390	Absorb spillage to prevent material damage.
P391	Collect spillage.
P301 + P310	IF SWALLOWED: Immediately call a POISON CENTER or doctor/physician.
P301 + P312	IF SWALLOWED: Call a POISON CENTER or doctor/physician if you feel unwell.

*continues on next page*

---

Identifier	Statement
P301 + P330 + P331	IF SWALLOWED: rinse mouth. Do NOT induce vomiting.
P302 + P334	IF ON SKIN: Immerse in cool water/wrap in wet bandages.
P302 + P350	IF ON SKIN: Gently wash with plenty of soap and water.
P302 + P352	IF ON SKIN: Wash with plenty of soap and water.
P303 + P361 + P353	IF ON SKIN (or hair): Remove/Take off immediately all contaminated clothing. Rinse skin with water/shower.
P304 + P340	IF INHALED: Remove victim to fresh air and keep at rest in a position comfortable for breathing.
P304 + P341	IF INHALED: If breathing is difficult, remove victim to fresh air and keep at rest in a position comfortable for breathing.
P305 + P351 + P338	IF IN EYES: Rinse cautiously with water for several minutes. Remove contact lenses, if present and easy to do. Continue rinsing.
P306 + P360	IF ON CLOTHING: Rinse immediately contaminated clothing and skin with plenty of water before removing clothes.
P307 + P311	IF exposed: Call a POISON CENTER or doctor/physician.
P308 + P313	IF exposed or concerned: Get medical advice/attention.
P309 + P311	IF exposed or if you feel unwell: Call a POISON CENTER or doctor/physician.
P332 + P313	If skin irritation occurs: Get medical advice/attention.

---

*continues on next page*

Identifier	Statement
P333 + P313	If skin irritation or rash occurs: Get medical advice/attention.
P335 + P334	Brush off loose particles from skin. Immerse in cool water/wrap in wet bandages.
P337 + P313	If eye irritation persists: Get medical advice/attention.
P342 + P311	If experiencing respiratory symptoms: Call a POISON CENTER or doctor/physician.
P370 + P376	In case of fire: Stop leak if safe to do so.
P370 + P378	In case of fire: Use ... for extinction.
P370 + P380	In case of fire: Evacuate area.
P370 + P380 + P375	In case of fire: Evacuate area. Fight fire remotely due to the risk of explosion.
P371 + P380 + P375	In case of major fire and large quantities: Evacuate area. Fight fire remotely due to the risk of explosion.
P401	Store ...
P402	Store in a dry place.
P403	Store in a well-ventilated place.
P404	Store in a closed container.
P405	Store locked up.
P406	Store in corrosive resistant/... container with a resistant inner liner.
P407	Maintain air gap between stacks/pallets.
P410	Protect from sunlight.
P411	Store at temperatures not exceeding °C/°F.
P412	Store at temperatures not exceeding 50°C/122°F.
P413	Store bulk masses greater than kg/lbs at temperatures not exceeding °C/°F.




















*continues on next page*

---






















Identifier	Statement
P420	Store away from other materials.
P422	Store contents under ...
P402 + P404	Store in a dry place. Store in a closed container.
P403 + P233	Store in a well-ventilated place. Keep container tightly closed.
P403 + P235	Store in a well-ventilated place. Keep cool.
P410 + P403	Protect from sunlight. Store in a well-ventilated place.
P410 + P412	Protect from sunlight. Do not expose to temperatures exceeding 50°C/122°F.
P411 + P235	Store at temperatures not exceeding °C/°F. Keep cool.
P501	Dispose of contents/container to ...








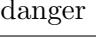


---

## B.2 Chemicals and Statements

Substance	Symbol	H	P	EUH
Acetone	  danger	225-319-336	210-261-305+351 +338	066
AA				
Cadmium oxide	   danger	301-330-341-350 -361fd-372-410	201-260-273-281 -284-301+310	
Chloric acid	  danger	271-314	220-280-305 +351-338-310	
Chloroform	  danger	351-361d-331 -302-372-319-315	261-281-305 +351+338-311	
CTAB	   danger	302-315-318 -335-410	261-273-280-305 +351+338-501	
Dioxane	   danger	225-319-335-351	210-261-281-305 +351+338	
DMSA				
Ethanol	 danger	225	210	
HPA				
Methanol	   danger	225-301-311-331 -370	210-260-280 -301+310-311	



Nitric acid	 	272-311+331	220-261-280-305	
	 danger	-314	+351+338-310	
Octadecanethiol	 warning	315-319-335	261-305+351+338	
ODPA				
Polystyrene				
Poly(vinyl formal)				
Potassium cyanide	 	290-300+310+330	260-264-273-280	
	  danger	-370-372-410	284-301+310	
Selenium	  danger	301+331 -373-413	261-301+310 -311	
Silver nitrate	    danger	272-302-314-410	220-273-280-305 +351+338-310-501	
Sodium	 	260-301+311-314	223-231+232-280-301	
Boron hydride	 danger		+310-370+378-422	
Sodium hydroxide	 danger	290-314	280-305+351+338 -310	
Sodium oleate				
Sulfur	 warning		315	
Tetrachloro- auric acid	  danger	314-317	280-305+351 +338-310	

TMOS	   	226-315-318-330-335	260-280-284-305  +351+338-310	
Toluene	  	225-361d-304-373  -315-336	210-261-281-301  +310-331	
TOP	 	314	280-305+351+338-310	
TOPO	 	315-318	280-305+351+338	

### B.3 CMR

Only chemicals with at least category 1B are listed here.

Chemical	Carcinogenic Category	Mutagenic Category	Toxic to reproduction Category
Cadmium oxide	1B	2	2
Chloroform	1B	2	2

# Bibliography

- [1] I. Ahmad, H. J. W. Zandvliet, and E. S. Kooij. Shape-induced separation of nanospheres and aligned nanorods. *Langmuir*, 30:7953–7961, 2014.
- [2] M. R. K. Ali, B. Snyder, and M. A. El-Sayed. Synthesis and optical properties of small au nanorods using a seedless growth technique. *Langmuir*, 28:9807–9815, 2012.
- [3] A. M. Alkilany, P. K. Nagaria, C. R. Hexel, T. J. Shaw, C. J. Murphy, and M. D. Wyatt. Cellular uptake and cytotoxicity of gold nanorods: molecular origin of cytotoxicity and surface effects. *Small*, 5(6):701–8, 2009.
- [4] L. Amirav and A. P. Alivisatos. Photocatalytic hydrogen production with tunable nanorod heterostructures. *J. Phys. Chem. Lett.*, 1:1051–1054, 2010.
- [5] N. W. Ashcroft and N. D. Mermin. *Solid State Physics*. Cengage Learning Emea, 1976.
- [6] K. Aslan, S. N. Malyn, and C. D. Geddes. Metal-enhanced fluorescence from gold surfaces: Angular dependent emission. *J. Fluoresc.*, 17:7–13, 2007.
- [7] G. A. Beane, K. Boldt, N. Kirkwood, and P. Mulvaney. Energy transfer between quantum dots and conjugated dyes. *J. Phy. Chem. C*, 118(31):18079–18086, 2014.
- [8] P. Bharadwaj and L. Novotny. Robustness of quantum dot power-law blinking. *Nano Lett.*, 11:2137–2141, 2011.
- [9] L. Biadala, B. Siebers, R. Gomes, Z. Hens, and D. R. Yakovlev. Tuning energy splitting and recombination dynamics of dark and bright excitons in cdse/cds dot-in-rod colloidal nanostructures. *J. Phy. Chem. C*, 118:22309–22316, 2014.

- 
- [10] C. F. Bohren and D. R. Huffman. *Absorption and Scattering of Light by Small Particles*. Wiley-VCH, 1998.
- [11] K. Boldt, S. Jander, K. Hoppe, and H. Weller. Characterization of the organic ligand shell of semiconductor quantum dots by fluorescence quenching experiments. *ACS Nano*, 5(10):8115–23, 2011.
- [12] A. Brioude, X. C. Jiang, and M. P. Pileni. Optical properties of gold nanorods: Dda simulations supported by experiments. *J. Phys Chem. B*, 109:13138–13142, 2005.
- [13] L. E. Brus. Electron-electron and electron-hole interaction in small semiconductor crystallites: The size dependence of the lowest excited electronic state. *J. Chem. Phys.*, 80:4403, 1984.
- [14] E. Carbó-Argibay, B. Rodríguez-Gonzalez, S. Gómez-Grana, A. Guerrero-Martínez, I. Pastoriza-Santos, J. Pérez-Juste, and L. M. Liz-Marzán. The crystalline structure of gold nanorods revisited: Evidence for higher-index lateral facets. *Angew. Chem. Int. Ed.*, 49:9397–9400, 2010.
- [15] L. Carbone, C. Nobile, M. De Giorgi, F. Della Sala, G. Morello, P. Pompa, M. Hytch, E. Snoeck, A. Fiore, I. R. Franchini, M. Nadasan, A. F. Silvestre, L. Chiodo, S. Kudera, R. Cingolani, and L. Manna. Synthesis and micrometer-scale assembly of colloidal cdse/cds nanorods prepared by a seesaw growth approach. *Nano Letters*, 7(10):2942–2950, 2007.
- [16] S. Chakraborty, G. Xing, Y. Xu, S. W. Ngiam, N. Mishra, T. C. Sum, and Y. Chan. Engineering fluorescence in au-tipped, cdse-seeded cds nanoheterostructures. *Small*, 1:1–6, 2011.
- [17] R. R. Chance, A. Prock, and R. Silbey. Comments on the classical theory of energy transfer. ii. extension to higher multipoles and anisotropic media. *J. Chem. Phys.*, 65(1):2527–2531, 1976.
- [18] F. Cichos, C. v. Borcyskowski, and M. Orrit. Power-law intermittency of single emitters. *Curr. Opin. Colloid Interface Sci.*, 12:272–284, 2007.

- [19] C. H. Crouch, O. Sauter, X. Wu, R. Purcell, C. Querner, M. Drndic, and M. Pelton. Facts and artifacts in the blinking statistics of semiconductor nanocrystals. *Nano Lett.*, 10:1692–1698, 2010.
- [20] R. D. Deegan, O. Bakajin, T. F. Dupont, G. Huber, S. R. Nagel, and T. A. Witten. Capillary flow as the cause of ring stains from dried liquid drops. *Nature*, 389:827–829, 1997.
- [21] J. Dimitrijevic, L. Krapf, C. Wolter, C. Schmittke, J.-P. Merkl, T. Jochum, A. Kornowski, A. Schüth, A. Gebert, G. Hüttmann, T. Vossmeier, and H. Weller. CdSe/cds-quantum rods: fluorescent probes for in vivo two-photon laser scanning microscopy. *Nanoscale*, 6:10413, 2014.
- [22] A. S. Dimitrov and K. Nagayama. Continuous convective assembling of fine particles into two-dimensional arrays on solid surfaces. *Langmuir*, 12:1303–1311, 1996.
- [23] K. H. Drexhage. Influence of a dielectric interface on fluorescence decay time. *J. Luminesc.*, 1-2:693, 1970.
- [24] J. Duan, D. N. Nepal, K. Park, J. E. Haley, J. H. Vella, A. M. Urbas, R. A. Vaia, and R. Pachter. Computational prediction of molecular photoresponse upon proximity to gold nanorods. *J. Phy. Chem. C*, 115:13691–13967, 2011.
- [25] A. L. Efros and A. L. Efros. Interband absorption of light in a semiconductor sphere. *Sov. Phys. Semicond.*, 7(16):772–775, 1982.
- [26] A. L. Efros and M. Rosen. Random telegraph signal in the photoluminescence intensity of a single quantum dot. *Phys. Rev. Lett.*, 78(6):1110–1113, 1997.
- [27] M. A. El-Sayed. Small is different: Shape-, size-, and composition-dependent properties of some colloidal semiconductor nanocrystals. *Acc. Chem. Res.*, 37:326–333, 2004.
- [28] S. Eustis and M. A. El-Sayed. Why gold nanoparticles are more precious than pretty gold: Noble metal surface plasmon resonance and its enhancement of the radiative and nonradiative properties of nanocrystals of different shapes. *Chem. Soc. Rev.*, 35:209–217, 2006.
- [29] S. L. Flegler, J. W. Heckman, and K. L. Klomparens. *Elektronenmikroskopie*. Spektrum Akademischer Verlag, 1995.

- [30] S. Flessau. *Fluorescence Spectroscopy of Individual Semiconductor Nanoparticles in Solution*. PhD thesis, University of Hamburg, 2014.
- [31] T. Förster. Transfer mechanisms of electronic excitation. *Discuss. Faraday Soc.*, 27:7–17, 1959.
- [32] P. Frantsuzov, M. Kuno, B. Jankó, and R. A. Marcus. Universal emission intermittency in quantum dots, nanorods and nanowires. *Nature Physics*, 4:519–522, 2008.
- [33] P. A. Frantsuzov and R. A. Marcus. Explanation of quantum dot blinking without the long-lived trap hypothesis. *Phys. Rev. B*, 72:155321, 2005.
- [34] Y. Fu and J. R. Lakowicz. Modification of single molecule fluorescence near metallic nanostructures. *Laser and Photon. Rev.*, 3(1-2):221–233, 2009.
- [35] Y. Fu, J. Zhang, and J. R. Lakowicz. Plasmon-enhanced fluorescence from single fluorescence end-linked to gold nanorods. *J. Am. Chem. Soc.*, 132:5540–5541, 2010.
- [36] R. Gans. Über die form ultramikroskopischer goldteilchen. *An. Phys.*, 37:881, 1912.
- [37] L. Genzel, T. P. Martin, and U. Kreibig. Dielectric function and plasma resonances of small metal particles. *Z. Phys. B*, 21(4):339–346, 1975.
- [38] J. J. Giner-Casares and L. M. Liz-Marzán. Plasmonic nanoparticles in 2d for biological applications: Toward active multipurpose platforms. *Nanotechnology*, 9(3):365–377, 2014.
- [39] A. Gole and C. J. Murphy. Seed-mediated synthesis of gold nanorods: Role of the size and nature of the seed. *Chem. Mater.*, 16(19):3633–3640, 2004.
- [40] D. E. Gómez, M. Califano, and P. Mulvaney. Optical properties of semiconductor nanocrystals. *Phys. Chem. Chem. Phys.*, 8:4989–5011, 2006.
- [41] S. Gómez-Grana, F. Hubert, F. Testard, A. Guerrero-Martínez, I. Grillo, L. M. Liz-Marzán, and O. Spalla. Surfactant (bi)layers on gold nanorods. *Langmuir*, 28:1453–1459, 2012.

- [42] A. O. Govorov, G. W. Bryant, W. Zhang, T. Skeini, J. Lee, N. A. Kotov, J. M. Slocik, and R. R. Naik. Exciton-plasmon interaction and hybrid exciton in semiconductor metal nanoparticle assemblies. *Nano Letters*, 6(5):984–994, 2006.
- [43] M. Grzelczak, J. Pérez-Juste, P. Mulvaney, and L. M. Liz-Marzán. Shape control in gold nanoparticle synthesis. *Chem. Soc. Rev.*, 37:1783–1791, 2008.
- [44] A. Guerrero-Martínez, J. Pérez-Juste, E. Carbó-Argibay, G. Tardajos, and L. M. Liz-Marzán. Gemini-surfactant-directed self-assembly of monodisperse gold nanorods into standing superlattices. *Angew. Chem. Int. Ed.*, 48:9484–9488, 2009.
- [45] A. Guerrero-Martínez, M. Grzelczak, and L. M. Liz-Marzán. Molecular thinking for nanoplasmonic design. *ACS Nano*, 6(5):3655–3662, 2012.
- [46] X. Guo, Q. Zhang, Y. Sun, Q. Zhao, and J. Yang. Lateral etching of core-shell au@metal nanorods to metal-tipped au nanorods with improved catalytic activity. *ACS Nano*, 6, 2012.
- [47] W. Haiss, N. T. K. Thanh, J. Aveyard, and D. G. Fernig. Determination of size and concentration of gold nanoparticles from uv-vis spectra. *Analytical Chemistry*, 79(11):4215–4221, 2007.
- [48] G. M. Hale and M. R. Querry. Optical constants of water in the 200 nm to 200  $\mu$ m wavelength region. *Appl. Optics*, 12:557–562, 1973.
- [49] M. A. Hampton, T. A. H. Nguyen, A. V. Nguyen, Z. P. Xu, and L. Huang. Influence of surface orientation on the organization of nanoparticles in drying nanofluid droplets. *Journal of Colloid and Interface Science*, 377:456–462, 2012.
- [50] K. Hosoki, T. Tayagaki, S. Yamamoto, K. Matsuda, and Y. Kanemitsu. Direct and stepwise energy transfer from excitons to plasmons in close-packed metal and semiconductor nanoparticle monolayer films. *Phys. Rev. Lett.*, 100:207404, 2008.
- [51] H. Hu and R. G. Larson. Marangoni effect reverses coffee-ring depositions. *J. Phys Chem. B*, 110:7090–7094, 2006.
- [52] N. Gomez i Bastus. *Gold Nanoparticles for Biomedical Applications: Synthesis, Conjugation and in vitro Experiments*. PhD thesis, Universitat de Barcelona, 2008.

- [53] Y. Ito, K. Matsuda, and Y. Kanemitsu. Mechanism of photoluminescence enhancement in single semiconductor nanocrystals on metal surfaces. *Physical Review B*, 75:03309, 2007.
- [54] P. K. Jain, K. S. Lee, I. H. El-Sayed, and M. A. El-Sayed. Calculated absorption and scattering properties of gold nanoparticles of different size, shape, and composition: Applications in biological imaging and biomedicine. *J. Phys. Chem. B*, 110:7238–7248, 2006.
- [55] N. R. Jana. Gram-scale synthesis of soluble, near-monodisperse gold nanorods and other anisotropic nanoparticles. *Small*, 1(8-9):875–882, 2005.
- [56] N. R. Jana, L. Gearheart, S. O. Obare, and C. J. Murphy. Anisotropic chemical reactivity of gold spheroids and nanorods. *Langmuir*, 18(3):922–927, 2002.
- [57] S. Jander. *Synthese und optische Untersuchungen von einzelnen Halbleiternanokristallen*. PhD thesis, Universität Hamburg, 2011.
- [58] S. Jander, A. Kornowski, and H. Weller. Energy transfer from cdse/cds nanorods to amorphous carbon. *Nano Lett.*, 11(12):5179–83, 2011.
- [59] C. Javeaux, B. Mahler, B. Dubertret, A. Shabaev, A. V. Rodina, Al. L. Efros, D. R. Yakovlev, F. Lui, M. Bayer, G. Camps, L. Biadala, S. Buil, X. Quelin, and J.-P. Hermier. Thermal activation of non-radiative auger recombination in charged colloidal nanocrystals. *Nature Nanotechnology*, 8:206–212, 2013.
- [60] S. Jin, E. DeMarco, M. J. Pellin, O. K. Farha, and G. P. Wiederrecht. Distance-engineered plasmon-enhanced light harvesting in cdse quantum dots. *J. Phys. Chem. Lett.*, 4:3527–3533, 2013.
- [61] M. Kawai, A. Yamamoto, N. Matsuura, and Y. Kanemitsu. Energy transfer in mixed cdse and au nanoparticle monolayers studied by simultaneous photoluminescence and raman spectral measurements. *Physical Review B*, 78:153308, 2008.
- [62] M. Kawai, A. Yamamoto, and H. Yanagi. Electromagnetic-field enhancement and energy transfer effects on photoluminescence in au/poly(methyl methacrylate)/cdse-nanoparticle multilayers. *J. Phys. Soc. Jpn.*, 80:014704, 2011.



- [63] S. Kedenburg, M. Vieweg, T. Gissibl, and H. Giessen. Linear refractive index and absorption measurements of nonlinear optical liquids in the visible and near-infrared spectral region. *Optical Materials Express*, 2(11):1588–1611, 2012.
- [64] C. Kittel. *Introduction to Solid State Physics*. Wiley-VCH, 8th edition, 2004.
- [65] C. Kuemin, L. Nowack, L. Bozano, N. D. Spencer, and H. Wolf. Oriented assembly of gold nanorods on the single-particle level. *Adv. Funct. Mater.*, 22:702–708, 2012.
- [66] O. Kulakovich, N. Strekal, A. Yaroshevich, S. Maskevich, S. Gaponenko and Nabiev, U. Woggon, and M. Artemyev. Enhanced luminescence of cdse quantum dots on gold colloids. *Nano Letters*, 2(12):1449–1452, 2002.
- [67] M. Kuno, D. P. Fromm, H. F. Hamann, A. Gallagher, and D. J. Nesbitt. Nonexponential "blinking" kinetics of single cdse quantum dots: A universal power law behavior. *J. Chem. Phys.*, 112(7):3117–3120, 2000.
- [68] J. R. Lakowicz. Radiative decay engineering 5: metal-enhanced fluorescence and plasmon emission. *Anal Biochem.*, 337(2):171–194, 2005.
- [69] J. R. Lakowicz and C. D. Geddes. *Topics in Fluorescence Spectroscopy*, volume 8. Springer, 2004.
- [70] V. K. LaMer and R. H. Dinegar. Theory, production and mechanism of formation of monodispersed hydrosols. *J. Am. Chem. Soc.*, 72(11):4847–4854, 1950.
- [71] P. R. Lang. Depletion interaction mediated by polydisperse rods. *J. Chem. Phys.*, 127:124906, 2007.
- [72] C.-C. Lin, L.-K. Chau, S.-S. Chang, and C. R. C. Wang. Langmuir-blodgett films of alkanethiolate gold nanorods. *J. Chin. Chem. Soc.*, 50:1015–1021, 2003.
- [73] S. Link, M. B. Mohamed, and M. A. El-Sayed. Simulation of the optical absorption spectra of gold nanorods as a function of their aspect ratio and the effect of the medium dielectric constant. *J. Phys Chem. B*, 103:3073–3077, 1999.
- [74] S. E. Lohse and C. Murphy. The quest of shape control: A history of gold nanorod synthesis. *Chem. Mater.*, 25:1250.1261, 2013.
- [75] S. E. Lohse, N. S. Burrows, L. Scarabelli, and L. M. Liz-Marzán. Anisotropic noble metal nanocrystal growth: The role of halides. *Chem. Mater.*, 26:34–43, 2014.

- [76] X. Ma. *Manipulation of Photoluminescence from Semiconductor Nanocrystals by Bandgap Engineering and Surface Plasmons*. PhD thesis, University of Hamburg, 2011.
- [77] X. Ma, H. Tan, T. Kipp, and A. Mews. Fluorescent enhancement, blinking suppression, and gray states of individual semiconductor nanocrystals close to gold nanoparticles. *Nano Letters*, 10:4166–4174, 2010.
- [78] B. Mahler, P. Spinicelli, S. Buil, X. Quelin, J.-P. Hermier, and B. Dubertret. Towards non-blinking colloidal quantum dots. *Nature Materials*, 7:659–664, 2008.
- [79] O. M. Marago, P. H. Jones, P. G. Gucciardi, G. Volpe, and A. C. Ferrari. Optical trapping and manipulation of nanostructures. *Nature Nanotechnology*, 8(11):807–819, 2013.
- [80] G. Margolin, V. Protasenko, M. Kuno, and E. Barkai. Power law blinking quantum dots: Stochastic and physical models. *Adv. Chem. Phys.*, 133:327–356, 2006.
- [81] A. Martin, C. Schopf, A. Pescaglini, A. O’Riordan, and D. Iacopino. Synthesis, optical properties and self-assembly of gold nanorods. *Journal of Experimental Nanoscience*, 7(6):688–702, 2012.
- [82] A. Martín, C. Schopf, A. Pescaglini, J. J. Wang, and D. Iacopino. Facile formation of ordered vertical arrays by droplet evaporation of au nanorod organic solutions. *Langmuir*, 2014.
- [83] K. Matsuda, Y. Ito, and Y. Kanemitsu. Photoluminescence enhancement and quenching of single cdse/zns nanocrystals on metal surfaces dominated by plasmon resonant energy transfer. *Appl. Phys. Lett.*, 92:211911, 2008.
- [84] Marie-Isabel Mattern. *Herstellung von linear strukturierten, nanoskalierten Substraten mittels Soft-Lithographie und Einlagerung von Nanokomposit-Materialien in die erzeugten Vorstrukturen*. PhD thesis, University of Hamburg, 2013.
- [85] B. C. Mei, E. Oh, K. Susumu, D. Farrell, T. J. Mountziaris, and H. Mattoussi. Effects of ligand coordination number and surface curvature on the stability of gold nanoparticles in aqueous solutions. *Langmuir*, 25:10604–10611, 2009.
- [86] E. Meyer. Atomic force microscopy. *Progress in Surface Science*, 41:3–49, 1992.

- [87] T. Ming, X. Kou, H. Chen, T. Wang, H.-L. Tam and K.-W. Cheah, J.-Y. Chen, and J. Wang. Ordered gold nanostructure assemblies formed by droplet evaporation. *Angew. Chem. Int. Ed.*, 47:9685–9690, 2008.
- [88] T. Ming, L. Zhao, Z. Yang, H. Chen, L. Sun, J. Wang, and C. Yan. Strong polarization dependence of plasmon-enhanced fluorescence on single gold nanorods. *Nano Letters*, 9(11):3896–3903, 2009.
- [89] K. Mitamura, T. Imae, N. Saito, and O. Takai. Fabrication and self-assembly of hydrophobic gold nanorods. *J. Phys. Chem. B*, 111:8891–8898, 2007.
- [90] C. B. Murray, D. J. Norris, and M. G. Bawendi. Synthesis and characterization of nearly monodisperse cde (e =s, se, te). *J. Am. Chem. Soc.*, 115(19):8706–8715, 1993.
- [91] D. Nepal, L. F. Drummy, S. Biswas, K. Park, and R. A. Vaia. Large scale solution assembly of quantum dot-gold nanorod architectures with plasmon enhanced fluorescence. *ACS Nano*, 7(10):9064–9074, 2013.
- [92] R. G. Neuhauser, K. T. Shimizu, W. K. Woo, S. A. Empedocles, and M. G. Bawendi. Correlation between fluorescence intermittency and spectral diffusion in single semiconductor quantum dots. *Phys. Rev. Lett.*, 85(15):3301–3304, 2000.
- [93] Y. Niidome, Y. Nakamura, K. Honda, Y. Akiyama, K. Nishioka, H. Kawasaki, and N. Nakashima. Characterization of silver ions adsorbed on gold nanorods: surface analysis by using surface-assisted laser desorption/ionization time-of-flight mass spectrometry. *Chem. Commun.*, 13:1754–1756, 2009.
- [94] B. Nikoobakht and M. A. El-Sayed. Preparation and growth mechanism of gold nanorods (nrs) using seed-mediated growth method. *Chem. Mater.*, 15(10):1957–1962, 2003.
- [95] M. Nirmal, B. O. Dabbousi, M. G. Bawendi, J. J. Mackling, J. K. Trautman, T. D. Harris, and L. E. Brus. Fluorescence intermittency in single cadmium selenide nanocrystals. *Nature*, 383:802–804, 1996.
- [96] K. S. Novoselov, A. K. Geim, S. V. Morozov, D. Jiang, Y. Zhang, S. V. Dubonos, and A. A. Firsov. Electric field effect in atomically thin carbon films. *Science*, 306(5696):666–9, 2004.

- [97] K. Okamoto, S. Vyawahare, and A. Scherer. Surface-plasmon enhanced bright emission from cdse quantum dot nanocrystals. *J. Opt. Soc. Am. B*, 8:1674–1678, 2006.
- [98] C. J. Orendorff and C. J. Murphy. Quantitation of metal content in the silver-assisted growth of gold nanorods. *J. Phys Chem. B*, 110:3990–3994, 2006.
- [99] B. Peng, Q. Zhang, X. Liu, Y. Ji, H. V. Demir, C. H. A. Huan, T. C. Sum, and Q. Xiong. Fluorophore-doped core-multishell spherical plasmonic nanocavities: Resonant energy transfer toward a loss compensation. *ACS Nano*, 7(6):6250–6259, 2012.
- [100] B. Peng, G. Li, D. Li, S. Dodson, Q. Zhang, J. Zhang, Y. Lee, H. V. Demir, X. Y. Ling, and Q. Xiong. Vertically aligned gold nanorod monolayer on arbitrary substrates: Self-assembly and femtomolar detection of food contaminants. *ACS Nano*, 7(7):5993–6000, 2013.
- [101] B. Peng, Z. Li, E. Mutlugun, P. L. Hernández Matinez, D. Li and Q. Zhang, Y. Gao, H. V. Demir, and Q. Xiong. Quantum dots on vertically aligned gold nanorod monolayer: plasmon enhanced fluorescence. *Nanoscale*, 6:5592–5598, 2014.
- [102] J. Pérez-Juste, L. M. Liz-Marzán, S. Carnie, D. Y. C. Chan, and P. Mulvaney. Electric-field-directed growth of gold nanorods in aqueous surfactant solutions. *Adv. Funct. Mater.*, 14:571–579, 2004.
- [103] J. Pérez-Juste, I. Pastoriza-Santos, L. M. Liz-Marzán, and P. Mulvaney. Gold nanorods: Synthesis, characterization and applications. *Coordination Chemistry Reviews*, 249(17-18):1870–1901, 2005.
- [104] A. Petukhova, J. Greener, K. Liu, D. Nykypanchuk, R. Nicolay, K. Matyjaszewski, and E. Kumacheva. Standing arrays of gold nanorods end-tethered with polymer ligands. *Small*, 8, 2012.
- [105] Michael Quinten. *Optical Properties of Nanoparticle Systems*. Wiley-VCH, 1st edition, 2011.
- [106] F. T. Rabouw, P. Lunnemann, R. J. A. van Dijk-Moes, M. Frimmer, F. Pietra, A. F. Koenderink, and D. Vanmaekelbergh. Reduced auger recombination in single

- cdse/cds nanorods by one-dimensional electron delocalization. *Nano Lett.*, 13:4884–4892, 2013.
- [107] J. Rodríguez-Fernández, J. Pérez-Juste, P. Mulvaney, and L. M. Liz-Marzán. Spatially-directed oxidation of gold nanoparticles by au(iii)-ctab complexes. *J. Phys Chem. B*, 109:14257–14261, 2005.
- [108] R. Ruppin. Surface modes of two spheres. *Phys. Rev. B*, 26:3440, 1982.
- [109] R. Ruppin. Decay of an excited molecule near a small metal sphere. *J. Chem. Phys.*, 76:1681–1684, 1982.
- [110] G. Schlegel, J. Bohnenberger, I. Potapova, and A. Mews. Fluorescence decay time of single semiconductor nanocrystals. *Phys. Rev. Lett.*, 88(13):137401, 2002.
- [111] H. Schlicke, J. H. Schröder, M. Trebbin, A. Petrov, M. Ijeh, H. Weller, and T. Vossmeier. Freestanding films of crosslinked gold nanoparticles prepared via layer-by-layer spin-coating. *Nanotechnology*, 22:1–9, 2011.
- [112] F. Schulz, T. Vossmeier, N. G. Bastus, and H. Weller. Effect of the spacer structure on the stability of gold nanoparticles functionalized with monodentate thiolated poly(ethylene glycol) ligands. *Langmuir*, 29(31):9797–9908, 2013.
- [113] K. T. Shimizu, R. G. Neuhauser, C. A. Leatherdale, S. A. Empedocles, W. K. Woo, and M. G. Bawendi. Blinking statistics in single semiconductor nanocrystal quantum dots. *Physical Review B*, 63:205316, 2001.
- [114] K. T. Shimizu, W. K. Woo, B. R. Fisher, H. J. Eisler, and M. G. Bawendi. Surface-enhanced emission from single semiconductor nanocrystals. *Phys. Rev. Lett.*, 89(11):117401, 2002.
- [115] S. Si, C. Leduc, M.-H. Delville, and B. Lounis. Short gold nanorod growth revisited: The critical role of the bromide counterion. *Chem. Phys. Chem.*, 13:193–202, 2012.
- [116] D. Smith, N. R. Miller, and B. A. Korgel. Iodide in ctab prevents gold nanorod formation. *Langmuir*, 25(16):9518–9524, 2009.
- [117] D. K. Smith and B. A. Korgel. The importance of the ctab surfactant on the colloidal seed-mediated synthesis of gold nanorods. *Langmuir*, 24:644–649, 2008.

- [118] T. S. Sreeprasad, A. K. Samal, and T. Pradeep. One-, two-, and three-dimensional superstructures of gold nanorods induced by dimercaptosuccinic acid. *Langmuir*, 24:4589–4599, 2008.
- [119] D. Steiner, D. Dorfs, U. Banin, F. Della Sala, L. Manna, and O. Millo. Determination of band offsets in heterostructured colloidal nanorods using scanning tunneling spectroscopy. *Nano Lett.*, 8(9):2954–2958, 2008.
- [120] D. V. Talapin, R. Koeppe, S. Götzinger, A. Kornowski, J. M. Lupton, A. L. Rogach, O. Benson, J. Feldmann, and H. Weller. Highly emissive colloidal cdse/cds heterostructures of mixed dimensionality. *Nano Letters*, 3(12):1677–1681, 2003.
- [121] A. Ueda, T. Tayagaki, and Y. Kanemitsu. Energy transfer from semiconductor nanocrystal monolayers to metal surfaces revealed by time-resolved photoluminescence spectroscopy. *Appl. Phys. Lett.*, 92:133118, 2008.
- [122] R. Verberk, A. M. van Oijen, and M. Orrit. Simple model for the power-law blinking of single semiconductor nanocrystals. *Phys. Rev. B*, 66:233202, 2002.
- [123] L. Vigdeman, B. P. Khanal, and E. R. Zubarev. Functional gold nanorods: Synthesis, self-assembly, and sensing applications. *Adv. Mater.*, 24, 2012.
- [124] M. Wahl. Time-correlated single photon counting. PicoQuant GmbH Technical Notes, 2014.
- [125] Z. L. Wang, M. B. Mohamed, S. Link, and M. A. El-Sayed. Crystallographic facets and shapes of gold nanorods of different aspect ratios. *Surface Science*, 440: 809–814, 1999.
- [126] R. G. West and S. M. Sadeghi. Enhancement of energy transfer between quantum dots: The impact of metallic nanoparticle sizes. *J. Phys. Chem. C*, 116:20496–20503, 2012.
- [127] Y. Xie, S. Guo, Y. Ji, C. Guo, X. Liu, Z. Chen, X. Wu, and Q. Liu. Self-assembly of gold nanorods into symmetric superlattices directed by oh-terminated hexa(ethylene glycol) alkanethiol. *Langmuir*, 27:11394–11400, 2011.
- [128] Y. Xie, S. Guo, C. Guo, M. He, D. Chen, Y. Ji, Z. Chen, X. Wu, Q. Liu, and S. Xie. Controllable two-stage droplet evaporation method and its nanoparticle self-assembly mechanism. *Langmuir*, 29:6232–6241, 2013.

- 
- [129] X. Ye, L. Jin, H. Caglayan, J. Chen, G. Xing, C. Zing, V. Doan-Nguyen, Y. Kang, N. Engheta, C. R. Kagan, and C. B. Murray. Improved size-tunable synthesis of monodisperse gold nanorods through the use of aromatic additives. *ACS Nano*, 6(3):2804–2817, 2012.
- [130] X. Ye, Y. Gao, J. Chen, D. C. Reifsnyder, C. Zheng, and C. B. Murray. Seeded growth of monodisperse gold nanorods using bromide-free surfactant mixtures. *Nano Lett.*, 13(5):2163–2171, 2013.
- [131] X. Ye, C. Zheng, J. Chen, Y. Gao, and C. B. Murray. Using binary surfactant mixtures to simultaneously improve the dimensional tunability and monodispersity in the seeded growth of gold nanorods. *Nano Lett.*, 13:765–771, 2013.
- [132] E. Yuskovitz, I. Hadar, A. Sitt, I. Lieberman, and U. Banin. Interplay of quenching and enhancement effects in apertureless near-field fluorescence imaging of single nanoparticles. *J. Phy. Chem. C*, 115:15834–15844, 2011.
- [133] H. Yuan, K. P. F. Janssen, T. Franklin, G. Lu, L. Su, X. Gu, H. Uji-i, M. B. J. Roelfaers, and J. Hofkens. Reshaping anisotropic gold nanoparticles through oxidative etching: the role of the surfactant and nanoparticle surface curvature. *RCS Adv.*, 5:6829–6833, 2015.

## Declaration of Authorship

Ich, Wiebke FRIEDRICH, erkläre hiermit an Eides statt, dass ich die vorliegende Arbeit mit dem Titel 'Semiconductor Nanorods in the Vicinity of Ordered Gold Nanorods' selbst verfasst und keine anderen als die angegebenen Hilfsmittel benutzt habe. Ich versichere, dass diese Dissertation nicht in einem früheren Promotionsverfahren eingereicht wurde.

Signed:

---

Date:

---



# *Acknowledgements*

Im Nachfolgenden möchte ich den Personen danken, die mich in den letzten Jahren während der Erstellung meiner Dissertation begleitet haben. Menschen, die mich fachlich unterstützten, mir Hilfestellungen gaben, mir stets mit Rat und Tat zur Seite standen, mich aufbauten wenn die Motivation einmal nachließ und die mir stets Kraft gaben, an meinem Ziel festzuhalten.

Mein besonderer Dank gilt vorab Herrn Prof. Dr. Horst Weller, der mir ermöglicht hat, meine Dissertation in seinem Arbeitskreis anzufertigen. Darüber hinaus gilt mein Dank Herrn Prof. Dr. Alf Mews für die Übernahme des Zweitgutachtens. Hervorhebend danken möchte ich im Weiteren meiner Betreuerin Kathrin Hoppe, die mir stets mit fachlichen Ratschlägen zur Seite stand und mir mit ihren persönlichen Erfahrungsberichten sehr geholfen hat.

Ich bedanke mich sehr bei meinen Bachelor-Studenten Cornelius Fendler, Denislav Hristov, Maximilian Schwartz und Heiko von der Heide für ihre Mitarbeit im Labor.

Ich danke Andreas Kornowski für Ratschläge bezüglich der Elektronenmikroskopie und Robert Schön für seine Geduld beim Anfertigen der unzähligen SEM-Bilder. Mein Dank gilt dem gesamten AK Weller für hilfreiche Diskussionen und eine angenehme Arbeitsatmosphäre; speziell Florian Schulz für die Zusammenarbeit und Kollegialität, Klaus Boldt für anfängliche Erklärungen und Hilfe. Jannika Lauth und Robert Seher möchte ich für eine schöne Zeit danken. Mein besonderer Dank gilt Lena Wittern für die Gespräche, Unterstützung und ihr Verständnis.

Ich danke meinen Freunden und meinem Freund Markus Dertnig für seine Geduld, sein Einfühlungsvermögen und dass er für mich da war.

Abschließend gilt der größte Dank meinen Eltern, die mich nicht nur während meiner Dissertation großzügig und liebevoll unterstützt haben sondern auch in allen anderen Lebenslagen stets für mich da waren.